1-1-2015

Identification of Geostationary Satellites Using Polarization Data from Unresolved Images

Andy Speicher
University of Denver

IDENTIFICATION OF GEOSTATIONARY SATELLITES USING POLARIZATION DATA FROM UNRESOLVED IMAGES

_____

A Dissertation

Presented to

the Faculty of the Daniel Felix Ritchie School of Engineering and Computer Science

University of Denver

_____

In Partial Fulfillment

of the Requirements for the Degree

Doctor of Philosophy

_____

by

Andy Speicher

August 2015

Advisor: Mohammad Matin

Author: Andy Speicher
Title: IDENTIFICATION OF GEOSTATIONARY SATELLITES USING POLARIZATION DATA FROM UNRESOLVED IMAGES
Advisor: Mohammad Matin
Degree Date: August 2015

Abstract

In order to protect critical military and commercial space assets, the United States Space Surveillance Network must have the ability to positively identify and characterize all space objects. Unfortunately, positive identification and characterization of space objects is a manual and labor intensive process today since even large telescopes cannot provide resolved images of most space objects. Since resolved images of geosynchronous satellites are not technically feasible with current technology, another method of distinguishing space objects was explored that exploits the polarization signature from unresolved images.

The objective of this study was to collect and analyze visible-spectrum polarization data from unresolved images of geosynchronous satellites taken over various solar phase angles. Different collection geometries were used to evaluate the polarization contribution of solar arrays, thermal control materials, antennas, and the satellite bus as the solar phase angle changed. Since materials on space objects age due to the space environment, it was postulated that their polarization signature may change enough to allow discrimination of identical satellites launched at different times.

The instrumentation used in this experiment was a United States Air Force Academy (USAFA) Department of Physics system that consists of a 20-inch Ritchey-Chrétien telescope and a dual focal plane optical train fed with a polarizing beam splitter.

A rigorous calibration of the system was performed that included corrections for pixel bias, dark current, and response. Additionally, the two channel polarimeter was calibrated by experimentally determining the Mueller matrix for the system and relating image intensity at the two cameras to Stokes parameters S_0 and S_1.

After the system calibration, polarization data was collected during three nights on eight geosynchronous satellites built by various manufacturers and launched several years apart. Three pairs of the eight satellites were identical buses to determine if identical buses could be correctly differentiated. When Stokes parameters were plotted against time and solar phase angle, the data indicates that there were distinguishing features in S_0 (total intensity) and S_1 (linear polarization) that may lead to positive identification or classification of each satellite.

Acknowledgements

I would like to thank Dr. Mohammad Matin of the University of Denver School of Engineering and Computer Science for his technical guidance and leadership in this project. His sound advice was critical in establishing a plan for the execution of this research.

I would like to thank Dr. Francis Chun and Dr. Roger Tippets of the United States Air Force Academy Department of Physics for their vision of establishing capable research assets so that students could conduct meaningful research in the field of Space Situational Awareness (SSA). Without the USAFA telescope, this project would not have been possible since regular access to high caliber research instruments is extremely difficult. Thanks also to Dr. Chun and Dr. Tippets for their insight and technical experience that was generously offered in support of this project.

I would also like to thank Dr. David Strong of the USAFA for his help in assembling, calibrating and operating the research instruments. His expertise, guidance, and efforts were a key to collecting quality measurements for this study.

Table of Contents

List of Figures

List of Tables

CHAPTER ONE: INTRODUCTION

Motivation

The world relies on orbiting satellites for communications involving military services, banking transactions, paging, emergency beacon location, maritime messages, medical data transfers, GPS navigation signals, entertainment broadcasts, and natural disaster messages just to name a few. Satellites can also provide scientific data related to climate monitoring, mineral discovery, hydrology, agriculture, pollution monitoring, and astronomical research among other things. Keeping track of the thousands of operational satellites and orbital debris is critical to ensuring a continuation of the services we rely on every day. Notifying a satellite operator that a collision with space debris is imminent can only happen if the operational satellite has been positively identified by the Space Surveillance Network. Since satellites change orbits from time to time based on new launches or new operational plans, there has to be a way to positively identify satellites.

In 2006, Space Situation Awareness (SSA) was deemed by General Chilton (Commander of Air Force Space Command) and General Shelton (commander of JF-CC Space) as the number one priority to ensure our ability to protect our operations in space (Teehan 2007). A dependence on space assets requires SSA capabilities that include

detecting, identifying, and characterizing all operational satellites at the very least. Unfortunately, positive identification of space objects is a manual and labor intensive process today. Equally concerning is the fact that identifying an object that has maneuvered can take 7 to 30 days (Blake 2011).

Developing data discriminators for a system to identify specific satellites by their optical signature would add significant capabilities to the Space Surveillance Network. Optical signature parameters of unresolved satellite images that may be exploited include intensity, spectra, and polarization. While intensity and spectral content have been the topic of several satellite studies, there has been less of a focus on polarization. The objective of this investigation is to collect polarization data from unresolved images of passively-lit geosynchronous satellites to aid in the development of discriminators that can be used to identify individual satellites.

Since the amount of light that is polarized in a reflected visible-spectrum signature depends on the surface properties of the material it interacts with, polarization data along with the light reflection angles can give us insight into an optical signature of a particular spacecraft that is being observed. As the materials on a spacecraft age due to the space environment, this reflected signature may change due to surface property differences. Characterizing polarized light reflected off a spacecraft at various geometries may lead to understanding the signature caused by the solar arrays, body, or antennas for future use as a satellite identification discriminator.

Current Resolved Image Capabilities

One way to potentially identify a satellite uses resolved images collected by ground telescope assets. Unfortunately today's technology does not allow direct identification of a Geosynchronous Earth Orbit (GEO) satellite using detailed (resolved) imaging due to poor resolution. Calculating the diffraction limited resolution of a ground-based telescope can be accomplished using the following equation:

$$R = (1.22\ h\ \lambda) / D \quad (1)$$

where R is the resolution, h is the satellite altitude, λ is the wavelength of interest, and D is the diameter of the telescope aperture (Wertz 2010). A one-meter diameter telescope similar to the Space Surveillance Network (SSN) assets has a diffraction limited resolution of 0.6 meters at 1000 km and 22.0 meters at 36,000 km in the visible spectrum. Even increasing the telescope diameter to 4.0 meters will only provide 5.5 meter resolution at the geostationary altitude of approximately 36,000 km. Neither of these cases will enable discrimination of one satellite from another. Even the 10 meter Keck II telescope at the 14,000 foot summit of Mauna Kea Hawaii provides unrecognizable "resolved" images that only show the general shape of a satellite (Drummond 2010). These pixelated images do not provide enough information to identify a satellite. See Table 1 below for an analysis of the diffraction limited resolution of various diameter telescopes when viewing geosynchronous satellites. The range is optimistic in that it assumes the telescope is directly below the satellite of interest.

Telescope aperture diameter (m)	Range (km)	Wavelength (um)	Diffraction Limited Resolution (m)
0.5	36000	0.5	43.9
1.0	36000	0.5	22.0
2.0	36000	0.5	11.0
3.0	36000	0.5	7.3
4.0	36000	0.5	5.5
5.0	36000	0.5	4.4
10.0	36000	0.5	2.2

Table 1. Diffraction limited resolution for various diameter telescopes

Since satellites are being developed that are smaller than ever, there is little hope right now that direct identification via high resolution imaging from the ground is feasible. There are a number of spacecraft that may be detected by ground-based optical systems but remain unidentified due to a recent maneuver.

Optical Signature Parameters

The three parameters of an optical signature that may be used to identify or classify a particular spacecraft are intensity, spectrum, and polarization. All three optical signature components vary based on the fact that differences in a reflected signal from a passively lit spacecraft can stem from distinctive materials, degradation of surfaces due to the space environment, and sun angles.

The intensity of a satellite's reflected solar spectrum can be measured using a telescope and focal plane array to capture unresolved images at various sun angles and collection geometries. As satellite observation geometries such as solar array or body angles change, the intensity can be cataloged over time to establish a particular intensity

signature of a satellite. A recent study by Bruski, Harms, Jones, Thomas, and Dahlke showed that it may be possible to discern the basic size, shape, and orientation of a Low Earth Orbiting (LEO) satellite by analyzing the intensity collected from unresolved images (Bruski 2012). Identification of the satellites was not addressed by this particular study as it was assumed that the identity was known.

Another technique that has been investigated is to classify satellites by the spectral content reflected to an Earth observer. One study by Cauquy, Roggemann, and Schulz looked at visual and near IR data collected from numerous field observations to evaluate two pattern recognition methods: neural nets and nearest neighbor (Cauquy 2006). Various features of the data were used to discriminate between the different observed spectra which led to varying levels of success for the classification methods. Proper choice of features can greatly reduce the data processing required to reach a classification answer.

Polarization of a satellite's optical signature from an unresolved image may potentially be used to uniquely identify a satellite and is the focus of this dissertation.

Satellite Polarimetry Literature Search

A thorough review was conducted of the available SPIE, IEEE, and AMOS literature to understand previous satellite polarization studies. Colleagues in the field of Space Situational Awareness were also canvased to bring out any other sources of literature such as PhD dissertations that may be helpful. What follows is a summary of those studies as well as some discussion of how a particular study may be relevant to the work proposed in this paper.

Characterizing BRDF of Spacecraft Materials

Studies of optical scatter physics have shown that spacecraft materials can interact with the solar illumination to produce a polarized component that can be measured. Laboratory measurements by Bowers and Wellems of the Bidirectional Reflectance Distribution Function (BRDF) for typical spacecraft materials such as solar cells, Kapton, and aluminum have been conducted that characterize the interactions with electromagnetic radiation (Bowers 2011). These interactions are a function of material micro and macro properties. Reflections can also vary as they occur at a primary surface (ie: external component of paint), a volumetric material (ie: paint binder), or a secondary surface (paint pigment molecules). These complex interactions can lead to various polarity signatures. This data simply validates the idea of this research that spacecraft materials can have polarization components in their optical signature.

Simulations of Polarization Signatures for Active and Passive Illumination

One particular investigation attempted to see if satellites may potentially be classified based on the measured polarization from a satellite illuminated with passive (solar spectrum) and with an active (laser) energy source. This study by Bush, Crockett and Barnard used a reflectance model called Time-domain Analysis Simulation for Active Tracking or TASAT (Bush 2002). This tool uses the laboratory-measured reflectance characteristics of satellite materials assembled into a 3-D spacecraft shape to perform ray tracing. TASAT was used for this investigation to simulate the polarization expected from passive and active illumination. Since polarization depends heavily on the surface property of materials and illumination geometries relative to the observer, precise

answers can be difficult to obtain. It was determined that the use of polarization was promising in classifying satellites in the modeled environment.

Developing an Instrument to Measure All Four Stokes Parameters on the Battlefield

A study by Pesses and Ryan presented the analysis of a new method for measuring all four Stokes parameters using a single detector, spinning quarter-wave plate, and a stationary linear polarizer (Pesses 2007). One motivation for this study was to enable ground based assets to characterize surface properties of asteroids and comets. The proposed full Stokes parameter instrument is interesting and could add more valuable data to a satellite classifier but is fairly complex and will be much harder to calibrate than the system in place for this proposed study. Since a valuable portion of a spacecraft's reflected optical signature can be found in Stokes parameters S_0 and S_1, a two channel polarimeter will be used for the research in this dissertation.

Developing an Instrument to Measure Satellite Polarimetry

Another study by Tippets designed, built, and tested a four-channel polarimeter to be used with a telescope for determining polarization of resolved satellite images (Tippets 2005). Following a detailed calibration of the instrument, he collected polarization data from resolved images of the International Space Station (ISS). Stokes parameters for S_0, S_1, and S_2 were calculated from the data. He found that the Degree of Linear Polarization for the ISS was on the order of 20-35%. Several pieces of the Tippets detailed calibration procedure will be used in this proposed study.

Polarization Light Curves for Space Debris and Satellites

A study by Stryjewski, Hand, Tyler, Murali, Roggemann, and Peterson proposed a model to determine satellite material, orientation, and shape using a micro facet scattering model for Low Earth Orbit (LEO) satellites and debris (Stryjewski 2010). Although the study only analyzed two objects with different shapes, the Hubble Space Telescope and an Athena rocket body, it was concluded that polarization does provide a potential discriminator for spacecraft identification. The model also showed that polarization yields more data than a single intensity value because the two parameters are assumed to be uncorrelated. Since the Stryjewski study did not collect actual data to validate the concept of using polarimetric data to identify satellites, it is an important intermediate step but stops short of the goals accomplished in this dissertation.

Polarization

Electromagnetic radiation can be viewed as a wave made up of electric fields and magnetic fields with vectors at right angles to each other. The plane of these vectors is perpendicular to the direction of travel. The polarization type is defined as the direction (shape) traced out by the electric field vector temporally. Polarimetry is the study of electromagnetic wave front changes through interactions with the environment. See Figure 1 below for a look at the electric and magnetic field vectors. Unpolarized light can become polarized by reflection, refraction, and scattering (Hudson 1982).

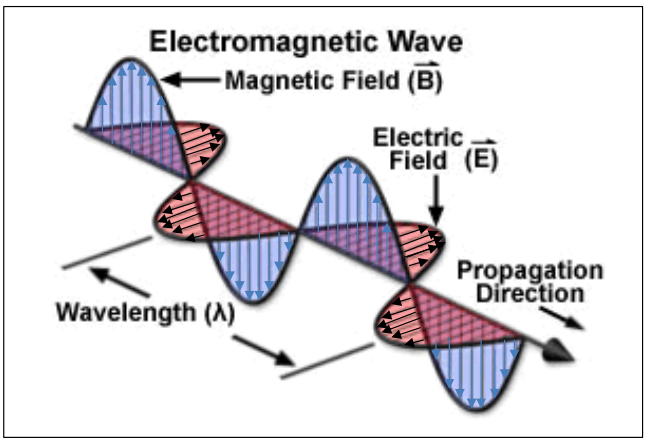

Figure 1. Electric and magnetic field vectors in electromagnetic radiation (micro.magnet.fsu.edu 2015)

Since the amount of light that is polarized in a signal depends on the surface properties (i.e., roughness, index of refraction) of the material it interacts with, this polarization data along with the incoming light and reflection angles may give us insight into an optical signature of a particular spacecraft that is being observed. As the materials on a spacecraft age, this signature may change due to surface property changes. Characterizing polarized light reflected off a spacecraft at various geometries can lead to understanding the signature caused by the solar arrays, body, or antennas for future use as a satellite identification discriminator. The Stokes vector described below allows us to decompose a light signal into four distinct characterization types that each can be used separately for study. This study will use two of those four parameters.

Unpolarized visible light can become polarized by three distinctly different interactions with the environment: reflection, refraction, and scattering. While the following sections will describe these interactions in detail, the polarization method exploited in this research is due to reflections of unpolarized light off of spacecraft materials.

Polarization Due to Reflections

As light interacts with a non-metallic or dielectric material it can be fully or partially polarized depending on surface properties of the material. Unpolarized light will be 100% polarized if reflected off a dielectric material at Brewster's Angle given by:

$$\tan \theta_i = n_2 / n_1 \quad (2)$$

where n_2 is the index of refraction of the dielectric material, n_1 is the index of refraction of the surrounding medium, and theta (θ_i) is the angle between the surface normal and incoming light (Hudson 1982). Unpolarized light that does not reflect at Brewster's Angle may be partially polarized. See Figure 2 for a diagram of the reflection geometry. Note in Figure 2 that P-polarization is in plane with the incident unpolarized light and reflected polarized light vectors. The S-polarization is perpendicular to the plane formed by the incident unpolarized light and reflected polarized light vectors. From this definition of polarization it can be shown that S-polarization will be what is seen by a ground observer when collecting a polarized reflected signal from a satellite. Based on the geometry of the sun, satellite and observer it is expected that a majority of the polarized signal will be vertically polarized as referenced to the telescope and observer.

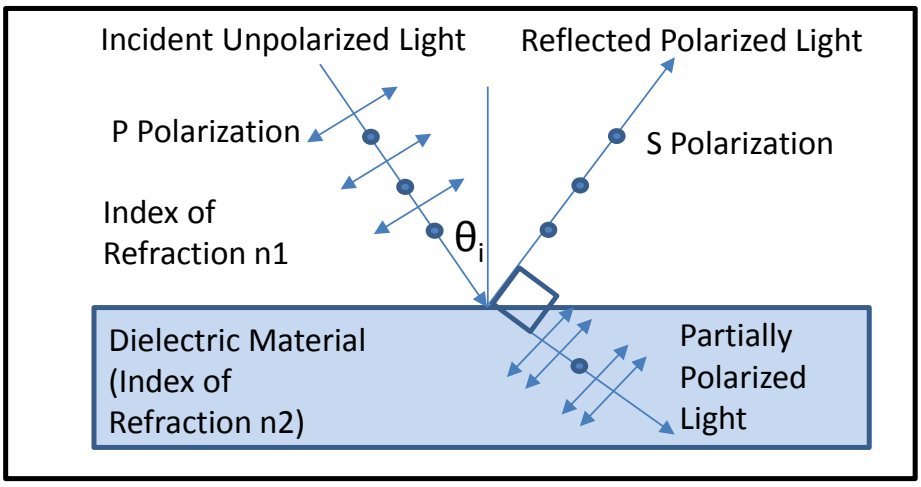

Figure 2. Polarization of light due to reflection (Hudson 1982)

After interacting with the exposed materials on a satellite, electromagnetic energy may become polarized in much the same way solar energy is polarized when it interacts with highway pavement or other dielectric materials. Light that reflects off of a concrete road is S-polarized or horizontally polarized as viewed from a driver in a car. Thus, polarized sunglasses have vertically polarized lenses so they block the incoming horizontal S-polarized light. In Figure 3 below the converse can be shown that if the slats or polarizering material in a polarimeter are oriented vertically as in the top part of Figure 3, then vertically polarized light is transmitted through. If the polarizer material is oriented horizontally, then the vertically polarized light is absorbed by the polarizing material and is not transmitted through (Physicsclassroom.com 2015). The research in this dissertation used a polarizing beamsplitter that can separate polarized light preferentially into P-polarization and S-polarization.

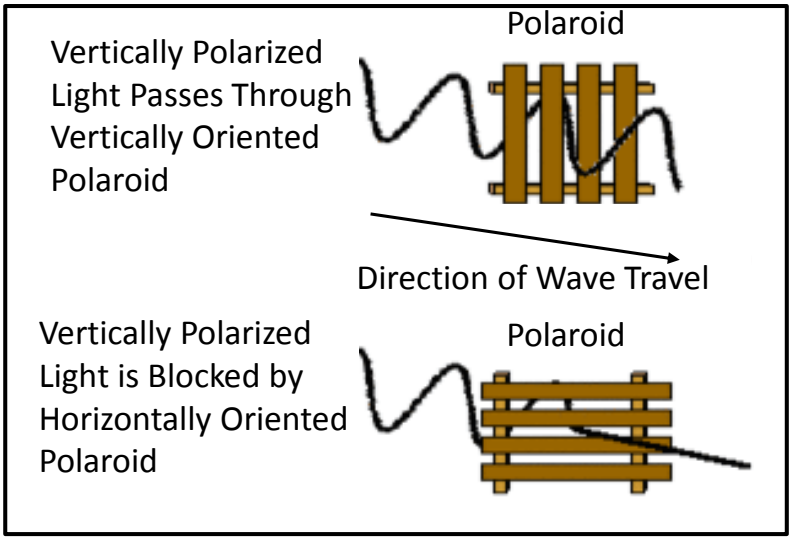

Figure 3. Polarized light interactions with a polaroid (Physicsclassroom.com 2015)

Polarization Due to Refraction

Unpolarized light can also be polarized by refraction when light passes from one material into another. An example of this is when light enters a calcite crystal and is divided into two orthogonal polarized beams: one that is horizontal and one that is vertically polarized as referenced from the crystal light entry surface (Hudson 1982). This occurs when an object is optically anisotropic or birefringent in that it has two different indices of refraction depending on the direction. Birefringence is caused by a non-symmetrical atomic lattice in the material which results in the binding force of the electrons being different depending on the polarization of incoming light. This causes the electrons to vibrate differently in different directions and thus the electromagnetic radiation propagates at different speeds through the material.

Polarization Due to Scattering

Light can also be polarized by scattering when it travels through a medium (Tinbergen 1996). As an example, sunlight scattered by the atmosphere can be linearly polarized such that the maximum polarization occurs at 90 degrees from the sun. This phenomenon occurs as light passes through our atmosphere often producing a glare in the sky. Proper use of a polarizing filter in photography can reduce this polarized, scattered light such that the photograph has a higher contrast (Schott 2009). Since the scattering involved with the relatively small amount of light reflected off of a satellite is forward scattered through the atmosphere, the original polarization is retained and will not affect the measurements used in this experiment.

Types of Polarized Light

Light can take on four different polarization states: unpolarized, linear polarization, circular polarization, or elliptical polarization. It should be noted that most of the time only a small portion of the light emanating from an object is polarized so the overall signal is said to be partially polarized. Since light can be described as wave-like in nature when discussing polarization, electric field behavior describes the polarization of an electromagnetic wave. When the electric field vector is random in phase and amplitude, the light can be defined as unpolarized (Tinbergen 1996, Schott 2009, Klinger 1990, Hudson 1982).

Linearly Polarized Light

An electric field vector that oscillates in a single direction is said to be linearly polarized (Tinbergen 1996). If the orientation of the vector varies slowly, it may still be

considered linearly polarized but its polarization angle is said to be changing. Thus the tip of the electric field vector traces out a line over time. See Figure 1 for a look at how the energy at any one point varies as a sinusoidal function.

Circularly Polarized Light

Since the electric field is a vector quantity, it is possible to add the vectors together to form a resultant vector. If two linearly polarized vectors of the same frequency and amplitude with vibration vectors at right angles but 90 degrees out of phase are added together, the polarization of the resultant vector is circular (Tinbergen 1996). When the resultant vector is viewed along its direct of motion, the tip traces out a circle. See Figure 6 for a look at the resultant vector. Notice that the magnitude does not vary and that the vector tip makes one rotation as the wave cycles through a period. Since the two linearly polarized vectors that were summed together can have slow changes in their polarization angle and magnitudes, the circle traced out by their resultant vector can also show changes in amplitude and phase. Depending on whether the two summed linearly polarized vectors are +/- 90 out of phase, the circle can be drawn out by the resultant vector tip rotating clockwise using the right hand rule with your thumb pointing along the propagation vector or counter-clockwise. Clockwise is called Right-Hand Circular Polarization (RHCP) as in Figure 6 below. A counter-clockwise trace is called Left Hand Circular polarization (LHCP).

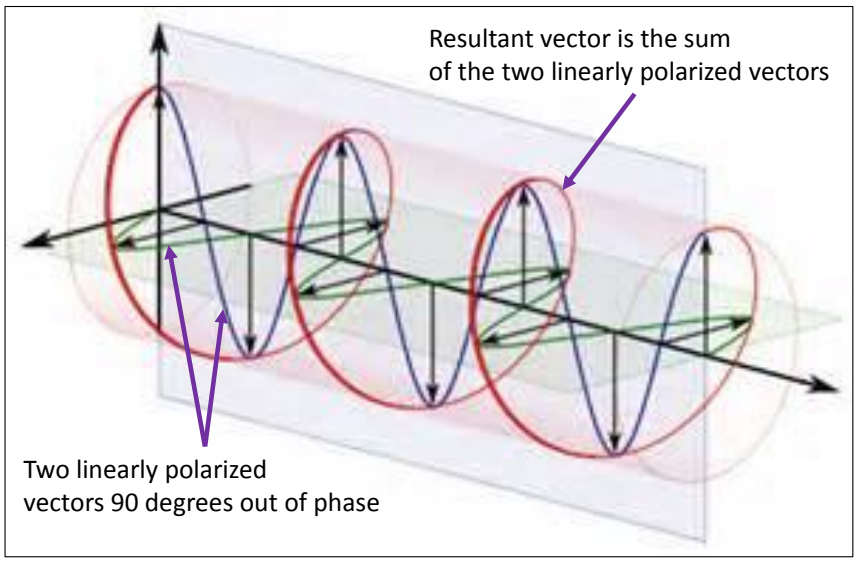

Figure 4. Two linearly polarized vectors summed to the circular resultant vector (wikimedia.org 2015)

Elliptically Polarized Light

The most common form of polarization is elliptical where the resultant vector temporally traces out an ellipse when viewed along the propagation path. See Figure 5 for an elliptically polarized resultant vector from the sum of two linearly polarized vectors. Elliptical polarization can be the resultant vector when any of the following are vector summed (Tinbergen 1996):

1. Two linearly polarized vectors with different amplitudes that are +/-90 degrees out of phase
2. Two linearly polarized vectors with the same amplitude that are something other than 0 or +/-90 degrees out of phase
3. Two linearly polarized vectors with different amplitudes that are also something other than 0 or +/-90 degrees out of phase

4. Two circularly polarized vectors of different handedness (RHCP, LHCP) and different amplitudes
5. A linearly polarized vector and a circularly polarized vector

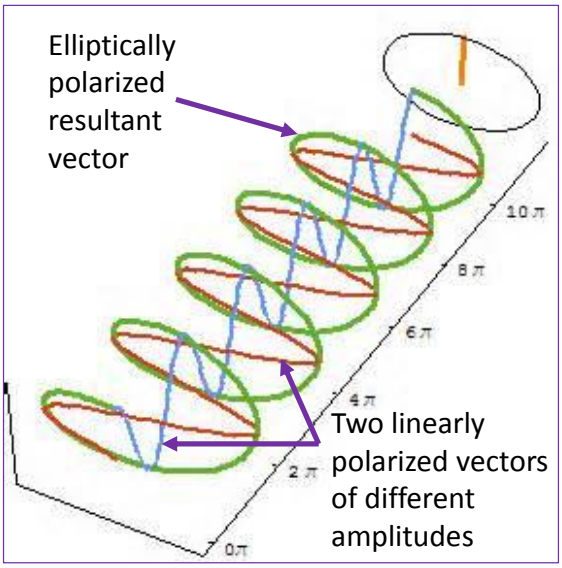

Figure 5. Elliptical polarization (sp.yimg.com 2015)

Measuring Polarization

Since the light signal reflected from an object may be made up of partially polarized light, measurement of the overall polarization properties may be useful. The amount of polarization measured may be compared to the total signal in a ratio to determine the "degree of polarization" (DOP) expressed as a percentage (Tinbergen 1996). The Degree of Linear Polarization (DOLP) expresses how much of the signal is linearly polarized and is dependent on Stokes S_1 and S_2. Since it is expected that S_1 will contain a majority of the polarization signals, it should be indicative of the linear polarization. It should be noted that the polarimeter cameras used in this study are oriented orthogonal to the right ascension plane. Since geostationary satellites don't

really move far from the celestial equator the coordinate system is nearly constant allowing measurements at different times to be compared. Characterizing the polarization of light reflected off a satellite usually involves separating the different polarization signals collected by the instrumentation. This can be accomplished in a variety of ways using crystals, prisms, etc. Some polarizer types include Glan, Glan Thompson, Foster, Wollaston, Rochon, Brewster prisms, and Calcite rods (Tinbergen 1996).

The polarizer instrumentation system used in this study is shown in Figure 6 where two prisms have been cemented together with a dielectric optical cement to form a polarizing beam splitter. The incident beam enters the cube and either reflects off the beam splitter coating at 90 degrees if it is horizontally polarized (S ray) or passes straight through if the light is vertically polarized (P ray). Two different cameras are used to capture the linearly polarized light that has been separated by polarization.

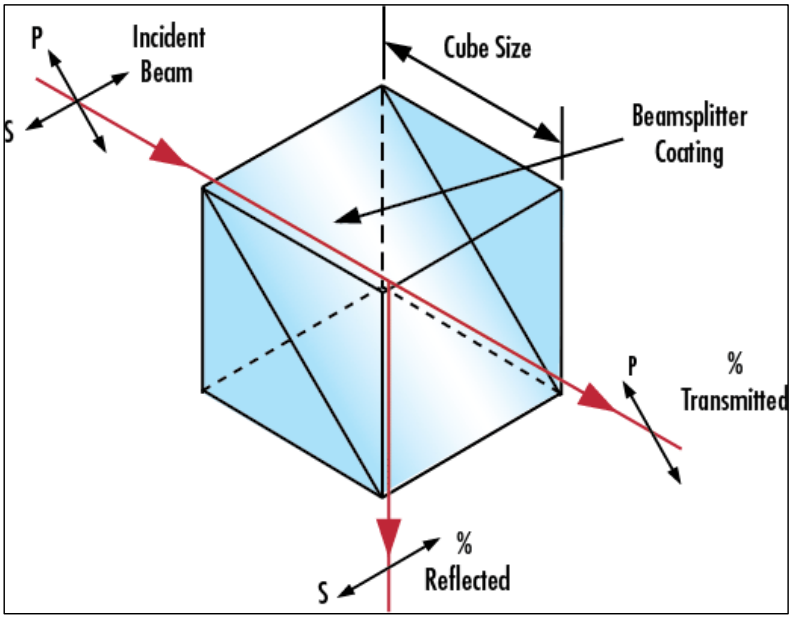

Figure 6. Polarizing beamsplitter (edmundoptics.com 2015)

Stokes Parameters

In 1852 Sir George Gabriel Stokes described the polarization of light using four parameters now called the Stokes parameters or when taken together called the Stokes vector (Tinbergen 1996). Each of the Stokes parameters (S_0, S_1, S_2, and S_3) represents a measurement of radiant energy as it pertains to describing the overall intensity and polarization of a particular signal. To uniquely characterize light using Stokes parameters, a set of six measurements must be taken using either filters or a rotating waveplate system. Kliger, Lewis, and Randall define the Stokes parameters as intensity measurements taken using filters with linear polarizations angles of 0, 45, 90, and -45 degrees along with a RHCP and LHCP filter (Klinger 1990). Once the measurements have been taken, the Stokes parameters are calculated as follows and normalized to the total intensity given by S_0 from the equation below:

$$S_0 = I_0 + I_{90} \tag{3}$$

$$S_1 = I_0 - I_{90} \tag{4}$$

$$S_2 = I_{45} - I_{-45} \tag{5}$$

$$S_3 = I_{RHCP} - I_{LHCP} \tag{6}$$

Stokes parameter S_0 describes the total intensity of a light beam and is the sum of the signal collected at 0 degrees and 90 degrees. Stokes parameter S_1 describes the preference for linear polarization over a range of 0 to 90 degrees and has a value normalized to S_0 of between -1.0 (vertical or P-polarization) and 1.0 (horizontal or S-polarization). Stokes parameter S_2 describes the preference for linear polarization over a range of -45 to +45 degrees and varies between -1.0 and 1.0 respectively when

normalized to S_0. Stokes parameter S_3 describes the preference for circular polarization over a range of LHCP to RHCP varies between -1.0 and 1.0 respectively when normalized to S_0. The Stokes vector allows a light signal to be decomposed into its constituent linear and circular components for in-depth study and characterization of a partially polarized signal.

Since the instrumentation setup for this experiment only includes a two-channel polarimeter, measurements will be taken for linear polarization at 0 and 90 degrees. Any component of the satellite optical signal that is circularly polarized will not be differentiated from the linear polarization signals. From equations (3) and (4) above it can be seen that the setup will produce Stokes parameters S_0 and S_1 for this study, thus linear polarization at +/-45 degrees and circular polarization cannot be addressed in this experiment. The two channels alone should be a good indicator of the presence of linear polarization which is more likely than circular polarization in a signal reflected from a satellite based on how circular polarization is generated. Since it takes two linearly polarized signals of approximately equal amplitude and rotated +/- 90 degrees out of phase to produce circular polarization, it is unlikely because this requires two reflections off of a satellite. The first reflection polarizes the light which is reflected off another surface and combined with the original polarized signal to form circular polarization. Since S_1 should account for a majority of the signal reflected from a satellite, the experiment will indicate the likelihood of using linear polarization to uniquely identify satellites.

Spacecraft Materials

Thermal Components

Satellite designers can use any combination of the thermal devices to achieve a spacecraft that keeps its components within their operations temperatures. A satellite can be designed so that it is "cold biased" in that the component temperatures tend to decrease over time if left alone. Heaters are then cycled on as necessary to keep components from getting too cold. Cold biasing is done because it is very easy to add heat to a component using thermostatically or computer controlled heater circuits. Conversely, it is much more complicated to actively cool a component.

Thermal components are used to control the flow of heat by either promoting or inhibiting the flow of heat. Optical Surface Reflectors, paints, kapton, and metals all generally promote the flow of heat from the satellite to the local environment. These components are usually flat, bright surfaces that reflect sunlight in a specular manner and also allow heat to exit the spacecraft. Paints, however, typically reflect light in a more diffuse manner. Insulating blankets on the other hand are used to keep components warm by restricting the flow of heat out of the spacecraft. A bright exterior surface of the blanket also reflects sunlight so the component does not get too hot if it exposed directly to the sun for long periods of time. Louvers are a special case since they are small, actively controlled, "Venetian blind" devices that open to allow heat to escape and close to keep heat inside the satellite as desired to keep components at the correct operating temperatures. A summarized list of typical external thermal components along with their respective Beginning of Life (BOL) absorptivity and emissivity is shown below in Table

2 (Wertz 2010). These surfaces can all reflect light and produce varying degrees of polarization that will be measured in this study at the aggregate level.

Surface Finish	Absorptivity (Beginning of Life)	IR Emissivity (Beginning of Life)
Optical Solar Reflector	0.05 to 0.16	0.66 to 0.80
White Paints	0.17 to 0.28	0.85 to 0.92
Black Paints	0.92 to 0.98	0.84 to 0.89
Aluminized Kapton	0.34 to 0.46	0.55 to 0.86
Metals	0.08 to 0.86	0.03 to 0.88
Thermal Blankets	0.22 to 0.90	0.34 to 0.86

Table 2. A list of typical external thermal surfaces along with their absorptivity and IR emissivity

Solar Cells

Solar cells are thin wafers of semiconductor materials used to collect solar power which is used to power the spacecraft electrical components. Solar cells are grouped together in parallel and series in order to provide the proper voltage and current as required by the satellite to conduct its mission. These cells are typically bonded onto an electrically insulated kapton face sheet with some form of epoxy. The face sheet is usually attached to an aluminum honeycomb substrate which provides structural rigidity. The epoxy used to bond the cells to the face sheet is visible between the cells and can provide a unique polarization signature that may be used for satellite identification. The silicon (Si) or Gallium Arsenide (GaAs) electrically active component of the solar cells is covered with a glass cover slide for protection and isolation. An anti-reflective coating on the outer surface of the cover slide helps to reduce power losses due to reflection off the

glass. The polarization properties of the cover slides along with their degraded properties over time can potentially be used to help identify a particular satellite. Light rays reflect off a solar array panel in both a specular and diffuse manner depending on the condition and composition of the external surfaces. Polarization of the specular reflections may yield discriminating data to help identify a particular spacecraft.

Antennas

Spacecraft antennas are used for either payload functions or as a command and telemetry link with the ground station. Payloads can be in the form of a two-way communications link like a high bandwidth data transponder or a radar for Earth monitoring. These mission activities require antennas that are a meter to several meters in diameter. Due to their size they provide a significant optical signature to a ground observer. Command and telemetry antennas on a spacecraft provide the ability to receive uplink commands or transmit state of health data to the ground. These antennas are usually centimeters to a meter in diameter and may be harder to use for satellite identification. Antennas can take many different shapes although parabolic dishes, helixes, and horns are popular due to their inherent gain characteristics and simple design. Phased array antennas are also used although to a lesser degree based on their high cost. Helix antennas are formed with spirals of wire that are supported by an internal electrically insulated material. On larger helixes the wires and structure may be visible and can provide a moderate spectral signature. Smaller helixes are usually encased in a light-weight dielectric foam material for protection and thermal control. This foam may have a specific optical signature although their small sizes may make their use more

difficult for spacecraft identification. Horn antennas are usually made of various light-weight metals that most likely will not polarize light that is reflected unless the metal is coated with a thermal or treated surface. Parabolic dishes can be large or small and are constructed of metals and composites with various surface electrical and thermal coatings. Large antennas may provide a significant optical signature for spacecraft identification.

Optical Signature Change Due to the Space Environment

It is well known that materials degrade significantly when exposed to the space environment. This environment consists of vacuum, neutral species, plasma, radiation, and micrometeorites (Tribble 1995). Each of these factors can affect the optical signature of materials due to the degradation or changing of material properties over increased exposure time. The largest contributors to optical changes due to material degradation are vacuum, Ultraviolet (UV) radiation, and neutral species. Although designers attempt to use materials that can still perform their functions in space, their interaction with the solar spectrum can dramatically change polarization as their exposure time to the space environment increases. This fact can be used as a discriminator when attempting to identify particular satellites in orbit by their polarization signature.

While the atmospheric pressure at sea level is approximately 1,000,000 Pascals, at an altitude of 100 km it drops to roughly 1 Pascal. The vacuum of space leads to two different material interactions that can cause changes in optical properties. The first interaction is due to the lack of pressure which allows materials to outgas contaminants that can migrate to sensitive surfaces and bind to the new surface. A new surface coating

means the polarization signature will most likely change. The second interaction relies on the fact that materials in space are exposed to the full brunt of the sun's ultraviolet (UV) radiation since there is no atmosphere to block the UV rays. Earth's ozone layer blocks most of the UV radiation from reaching the ground. UV photons have enough energy to break chemical bonds which leads to physical degradation of a material's surface. An experiment flown on NASA's Optical Properties Monitor (OPM) aboard the Russian MIR space station has confirmed that UV can cause discoloration of multilayer insulation blankets (Wilkes 2001). After a little more than eight months of exposure the solar absorptivity of the material had nearly doubled from 0.25 to 0.49. This can change a materials black body radiation temperature and optical signature.

The neutral environment pertains to the many molecular species that can affect satellite materials. Energetic collisions of particles against materials can lead to physical sputtering on the exterior surfaces. Sputtering breaks the bonds of exposed molecules and over time alters the physical properties of coatings and materials. Chemical reactions of spacecraft materials with neutral species occur at Low Earth Orbits (LEO) and can alter the optical signature of these materials. At altitudes as high as 650 km, the primary atmospheric constituent, atomic oxygen, can corrode or etch surfaces (Wilkes 2001). Experiments flown for over five years in LEO on the Long Duration Exposure Facility (LDEF) indicate that atomic oxygen actually enabled contamination from outgassing sources to deposit on materials (Rantanen 1998). Surfaces that had no exposure to atomic oxygen did not have any measurable contamination deposited on surfaces. The result of this particular contamination that was enabled by the atomic oxygen was a significant

discoloration and optical reflection change of the surface. Experiments flown aboard the MIR Space Station also indicated that atomic oxygen in concert with ultraviolet radiation enabled outgassed materials to deposit in thin films on spacecraft surfaces (Pippin 2002). The effect of the thin films was a significant change in the optical properties of the mirrored surfaces and even bare aluminum samples. Most of the studies cited above are concerned with the bulk property changes and emissivity/absorptivity changes of the materials as they are subjected to the space environment. The effect on the index of refraction or polarization signature of the materials was not addressed but is assumed given the significant surface changes referenced.

Data Collection Geometry

Since a spacecraft can have many different external surface materials that contribute to the optical signature, it is important to understand which materials may be discriminators. Figure 7 below describes the potential geometries associated with observing satellites. Since it is only possible to collect visual data on satellites when the ground observatory is in the dark, spacecraft positions P1, P2, and P8 are not candidate view positions. What this means is that it is unlikely a ground observatory will ever see the back side of a solar array unless there is reflection of the flux from the Earth. Since solar arrays usually have high emissivity white paints or other coatings on the back to radiate heat out of the solar panel, viewing large solar panel surfaces of white thermal paint are not likely but can occur.

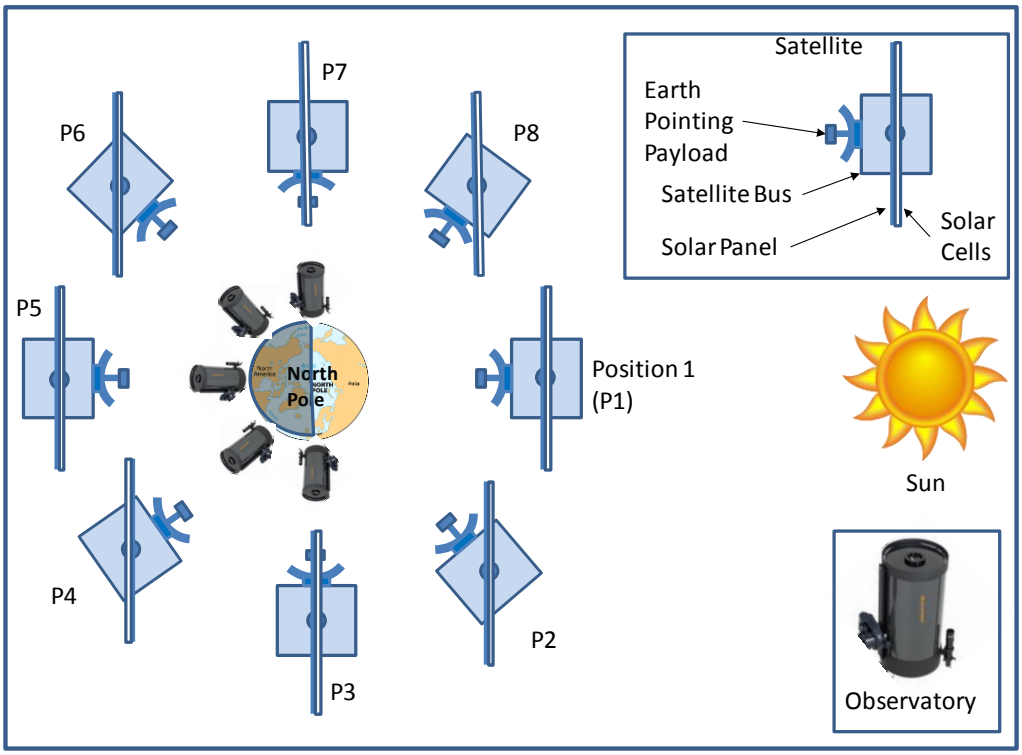

Figure 7. Earth observer sun angle and spacecraft geometry

Conversely, spacecraft positions P3, P4, P5, P6, and P7 will provide the ground observer with views of the solar cells, metallic interconnects, and bonding epoxy used on the solar arrays at many different sun angles. From positions P3 to P4 to P5 it may also be seen that the Earth observer gets a small edge-on view and then progressively better views of the entire array. This leads to a larger optical signature at position P5. As the satellite moves from positions P5 to P6 to P7 it may be seen that the observer gets a progressively more edge-on view of the solar array. The drawback to using solar cells as a polarization discriminator is that the cells and metallic interconnects usually reflect in a highly specular manner which means the ground observer will rarely get a strong signature. There are some rays that reflect in a more diffuse manner due to imperfect edges on solar cell cover glasses.

Typically the north and south faces of a spacecraft (in and out of the page) are usually covered with Optical Surface Reflectors (OSRs), aluminized kapton, or some other highly reflective (low absorptivity) and high emissivity material to reject heat to space. These surfaces do not get any significant exposure to the sun through the entire orbit and are ideal for radiator surfaces. Unfortunately these surfaces are rarely visible to Earth observers and will not figure prominently as polarization discriminators.

Another feature from Figure 7 is that an Earth observer usually sees the payload and antennas all the time since most payloads and communication antennas are pointed to the Nadir position at Earth. Typically the Nadir and adjoining sides of a spacecraft are covered with either thermal blankets or active surfaces like louvers to avoid overheating due to the sun and under-temping due to a temporary view of deep space at certain times in the orbit. Fortunately antennas and thermal blankets can have fairly large optical signatures due to their surface materials. Thermal blankets usually have highly reflective and irregularly shaped outer materials which leads to diffuse spreading of the reflected light rays. The irregular shapes of antennas also promote a wide dispersion of reflected light rays. Thermal components such as Optical Surface Reflectors, white paints, aluminized kapton, metals, and multilayer insulation blankets can all be found on surfaces that may be viewed by an Earth observer.

The discussion above leads to the conclusion that the satellite's optical signature to an Earth observer is driven by a combination of solar cells, cell bonding epoxy, solar cell interconnects, antennas, and thermal components. While it is not possible to separate the polarization signatures of these individual components, it is possible to determine

when a solar array is edge-on to an observer and thus the collected signature must be from other bus or payload components.

CHAPTER TWO: EXPERIMENTAL SETUP

In order to facilitate the training of students and faculty in Space Situational Awareness (SSA) research, the United States Air Force Academy (USAFA) Physics Department has assembled significant telescope assets (Dearborn 2011). The research-grade instruments and facilities are described below and offer significant capabilities for advances in the SSA body of knowledge.

Telescope

The size of the collection optics for this study is driven by the visual magnitude of the objects to be tracked. Satellites located in the geostationary belt can have visual magnitudes on the order of 10 to 15. In order to provide an adequate signal to noise ratio using a reasonable integration time, a 20-in diameter, f/8.1 Ritchey-Chrétien telescope from RC Optical Systems has been used for this study. One item that has been integrated into the system optics is a polarimeter designed by the U.S. Air Force Academy to allow simultaneous collection of two-channel polarimetry data. Figure 8 below shows the configuration for collecting polarimetry data and also a photograph of the collection system.

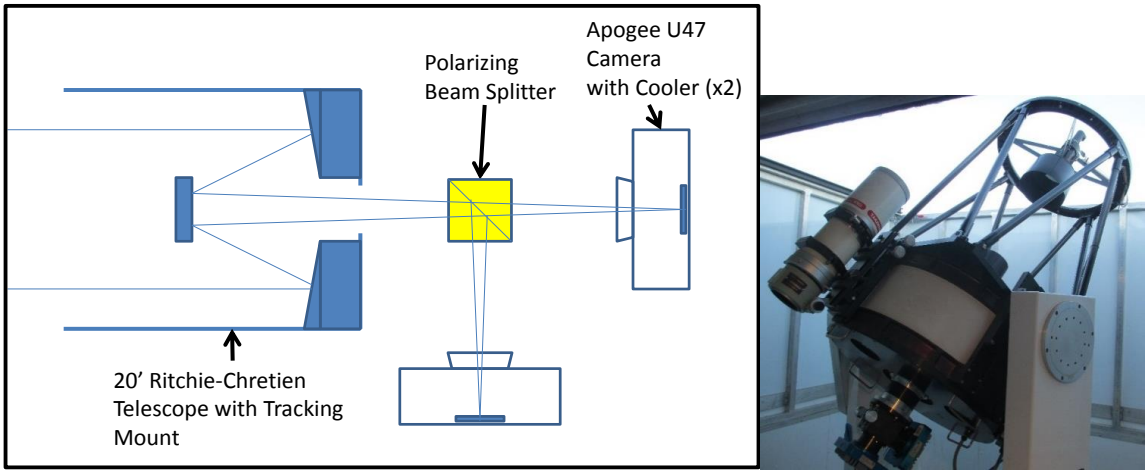

Figure 8. Polarimetry data collection configuration

Cameras

The cameras used for the data collection are Apogee F47 back-illuminated CCD's with a maximum quantum efficiency of 96%. These cooled CCD's have a 1024 X 1024 array of 13 X 13 micron size pixels all packaged in a 13.3 X 13.3 mm imaging area. The plate scale of the focal plane is 0.65 arc sec per pixel yielding an 11 X 11 arc minute field of view. Dark current for the pixels is typically 0.2 e/pixel/sec at -20 C and the system noise is typically 15 e RMS at 1 MHz. The focal plane array full well is 100k electrons, digital resolution is 16 bits, and the dynamic range is 83 dB (ccd.com, 2015). See Figure 9 for the camera quantum efficiency of the U47-MB (Mid-band) CCD.

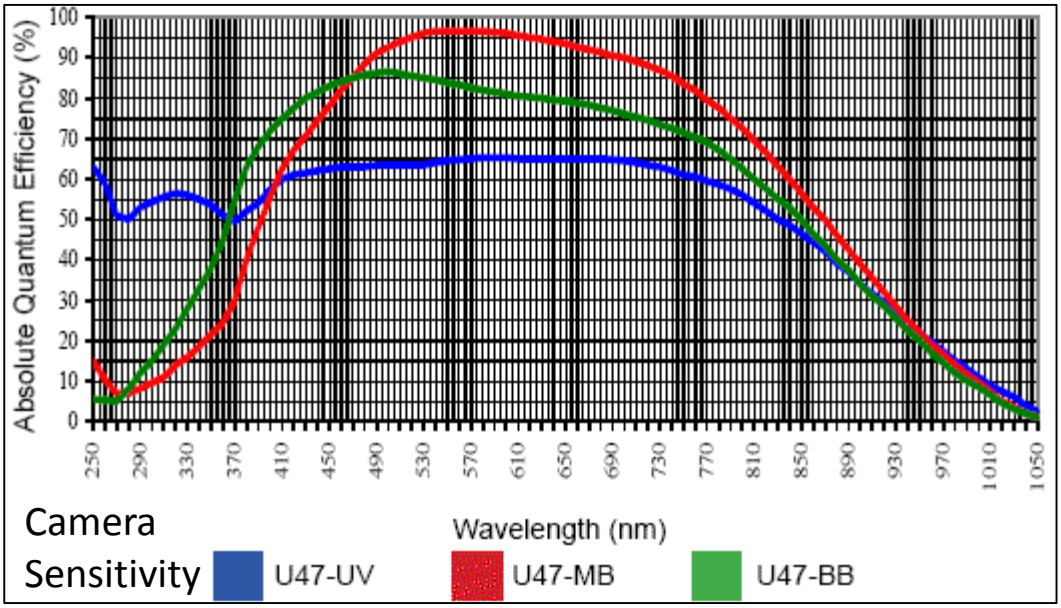

Figure 9. Apogee F47 (U47-MB) quantum efficiency vs wavelength (ccd.com, 2015)

Polarimeter

The polarizer instrumentation system used in this study is a polarizing beamsplitter where two prisms have been cemented together with a dielectric optical cement to form a polarizing beam splitter. The incident beam enters the cube and either reflects off the beamsplitter coating at 90 degrees if it is horizontally polarized (S ray) or passes straight through if the light is vertically polarized (P ray). Two different cameras are used to capture the linearly polarized light that has been separated by the polarizing beamsplitter. The broadband polarizing beamsplitter is an Edmund Optics, 50 mm cube with an antireflective coating designed for the visible spectrum. The cube passes greater than 90% of the vertically polarized light (P-pol) and reflects greater than 99% of the horizontally polarized light (S-pol). See Figure 10 and Table 3 for the beam splitter

transmission performance. See Figure 6 for the coordinate system used in Figure 10 below.

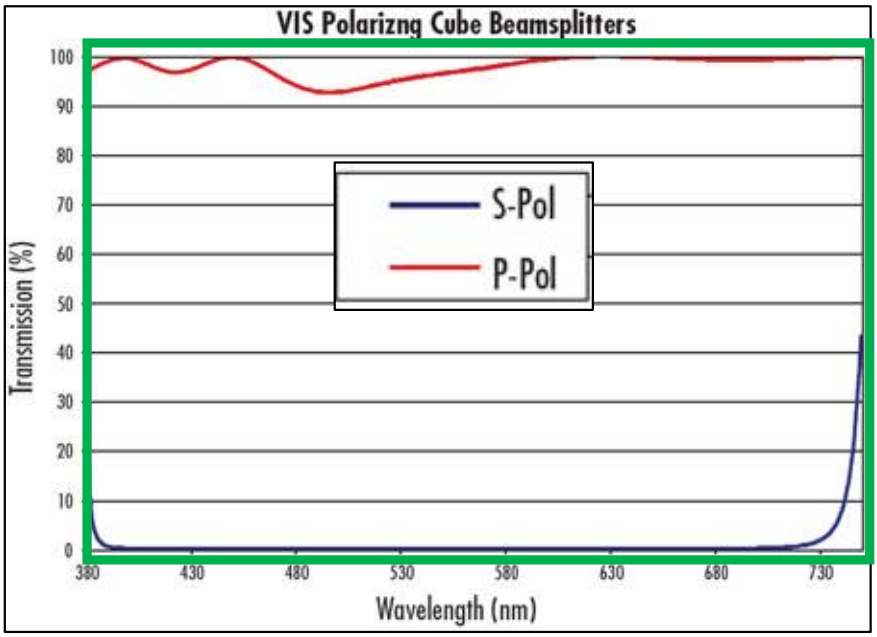

Figure 10. Polarizing beam splitter performance vs wavelength (edmundoptics.com 2015)

Clear Aperture (%)	90
Beam Deviation (arcminutes)	±3
Wavelength Range (nm)	420 - 680
P-Polarization Transmission (%)	>90
S-Polarization Reflection (%)	>99
Coating Specification	R_{avg} <0.5% @ 420 - 680 nm
Type	Linear Polarizer

Table 3. Polarizing beamsplitter specifications (edmundoptics.com 2015)

Instrumentation Signal to Noise Ratio

A model of the system was built in MathCad to determine performance and assist in data collection planning. The first assumption was that the geostationary satellite has an observed visual magnitude of 12. From this it was calculated that the number of

photons entering the 0.171 square meter effective aperture is 149,000 per second. From actual data it was seen that the satellite image is spread across approximately 210 total pixels. Each pixel receives 213 photons per second or 2,130 over a ten second integration time. Once the Quantum Efficiency (QE) is taken into account, 1,600 electrons are generated per pixel during the collect. Actual data for this same satellite showed 1,535 counts per pixel during the 10 second integration period for a difference of 4%. Since the CCD used for this study has very low noise characteristics, it was calculated that the Signal to Noise ratio was 109 when a 20% polarization case was taken into account. This is adequate for the study and will be increased even further by changing the integration time to 20 seconds to have approximately a one third to one half full electron well so the FPA is being operated in its linear range. See Table 4 for a summary of the modeled system parameters. See Appendix A for the algorithms in the MathCad worksheet.

Parameter	Value	Units
Assumed Satellite Visual Magnitude	12.0	N/A
Signal at telescope entrance	4.32E-13	W/m^2
Assumed wavelength	4.00E-07	m
Energy of a photon at given wavelength	4.97E-19	W/sec
Effective telescope aperture	0.171	m^2
Number of photons entering telescope	1.49E+05	photons/sec
Number of photons striking the FPA	4.47E+04	photons/sec
Number of pixels for satellite signal	210	pixels
Number of photons per pixel per second	213	photons/sec
FPA Quantum Efficiency	0.75	N/A
Number of electrons per pixel per second	160	electrons/pixel/sec
Integration period	10	sec
Electrons per pixel (model)	1600	electrons/pixel
Electrons per pixel (actual)	1535	electrons/pixel
Difference between model and actual	4	percent
Percentage of Full Well	1.6	percent
Detector readout noise	2	e- rms
Detector system noise	15	e- rms
Dark current	0.2	e- rms pixel/sec
Sky background noise estimate	20	e- per pixel/sec
Total Signal per 200 pixels	335,200	e-
Total Noise per 200 pixel	615	e- rms/pixel
Signal to Noise ratio per channel	545	N/A
Polarized Signal to Noise ratio per channel	109	N/A

Table 4. Summary of the modeled system parameters

CHAPTER THREE: INSTRUMENT CALIBRATION

Error sources

Polarization data collection systematic errors can come from polarization resident in the instrumentation setup such as those induced by the telescope optics, polarimeter, or cameras. These errors can be calibrated out. Since the Stokes vector of a light source could be modified as it interacts with the components of the data collection system, there is a method for calibrating the raw collected data so that it represents the true polarization state of the light reflected from a source. Mueller calculus uses a Mueller matrix to capture all the polarimetric terms in a system and calibrate them out so the final polarization data is meaningful (Tinbergen 1996).

It should be noted that errors due the atmosphere are small since turbulence affects all polarizations equally. Polarization errors due to the atmosphere are also small since Mie scattering in this geometry is forward scattering and the incident polarization signal is retained (Schott 2009). Rayleigh scattering is also minimal in forward scattering but increases as the scattering angle increases. Since the scattering angle will be nearly

zero for the geometry used in this experiment, polarization due to Rayleigh scattering will be extremely small.

In order to minimize the polarization induced in the telescope optical train, Ritchey-Chrétien optics will be used since they have only two mirrored surfaces and no glass refractive components. Glass optics disperse light and reduce the signal seen at the final focal plane array. Since the two mirrored surfaces in Ritchey-Chrétien optics are hyperbolic shapes, the secondary mirror has a smaller magnification factor which leads to a flatter field for better results at the focal plane array. According to Tinbergen, when the optics in the collection system are symmetrical, the effects on the polarization signature are small since the polarization action of the mirrors are radially oriented and average out at the focal plane (Tinbergen 1996). The symmetric mirror has polarization that is zero at the center and increases towards the edge. Fortunately, opposite sides of the mirror have the same polarization but with opposite signs so they cancel out when combined at the focal plane. There still can be significant polarization in the optical train, polarizer, and cameras that need to be calibrated. While the cameras used in this setup are not sensitive to polarization, there are errors in a focal plane such as bias, thermal noise, and sensitivity.

System calibration

There are three types of images that will be collected to calibrate the collection system: bias frames, dark frames, and flat frames. By collecting these three types of images on each of the two cameras it is possible to calibrate for the optical train errors in

the collection system to account for Focal Plane Array (FPA) zero bias, FPA dark current, and FPA pixel sensitivity.

Focal plane array zero bias

Focal Plane Array pixels each have a different zero point or bias that is characterized by taking a number of "bias" images with zero second exposures (or close to zero) while the shutter is closed. Whatever reading a pixel has is assumed to be due to this "zero level bias" since there is no light hitting the pixel and there is no time for thermal noise to accumulate. By subtracting the bias frames from the raw data this zero bias will be calibrated out of the raw data. For example, if a pixel read +5 Analog-to-Digital counts in a bias frame collection then it is assumed that the pixel reads more counts than it should when real data is collected since there is a starting pedestal at a non-zero number. For the zero bias calibration of this system, a total of 10 bias frames of zero integration time were taken with the shutter closed. All 10 of these frames were averaged together on a per-pixel basis so that the contribution by each pixel could be calibrated out of the observation data.

Focal plane array dark current

Each Charge Coupled Device (CCD) pixel also generates dark current or thermal noise at different rates. By taking a number of "dark" images with long exposures while the shutter is closed, the rate of dark current generation can be characterized. Any signal or "dark current" that is collected was generated by the FPA pixel circuitry and is a function of the CCD temperature. Cooling the FPA reduces the amount of thermal noise that is generated by a pixel. In this particular experiment the CCD is cooled to -20 °C. It

is important to collect the dark current images at the same CCD temperature that is planned for the observation data collection since dark current is a function of the CCD temperature. Another key for calibrating out the thermal noise is to collect the dark frames for the same integration time as the observation data since this will yield the most accurate knowledge of individual pixel dark current generation. Once these dark current frames are subtracted from the raw image data, the images have been calibrated with regard to dark current effects of the CCD. For the dark current (thermal noise) calibration of this system, a total of 10 dark frames of 20 second integration time were taken with the shutter closed. All 10 of these frames were averaged together on a per-pixel basis so that the contribution by each pixel could be calibrated out of the observation data.

Pixel sensitivity and optical train abnormalities

Each pixel also has a different sensitivity to light which is a function of the physical CCD pixel performance and the path taken by light through the optical train. Characterizing these effects can be accomplished by taking numerous “flat field” images at the desired exposure time using a flat, uniform light source. The source of flat, uniform light across the optical aperture can be the twilight sky or a special flat panel specifically designed for this purpose. Flat frames were collected in order to account for the effects of pixel sensitivity and optical train abnormalities.

A variation of the flat field images was used in this experiment to characterize and calibrate the polarizer system by inserting a polaroid between the flat panel and the telescope optical train entrance. By rotating the polaroid and collecting flat frame images at every 10 degrees of polaroid rotation, the performance of the setup can be

characterized. When the polaroid is configured to let only vertically polarized light through to the telescope optical train, the polarizing beam splitter should reflect very little light to the horizontal polarization camera. In this case most of the light is transmitted through the polarizing beam splitter to the vertical polarization camera. Conversely, when the polaroid is configured to let only horizontally polarized light into the telescope optical train, most of the light should be reflected to the horizontal polarization camera. See Figure 11 for the polarimeter characterization setup. The intensity of light reflected or transmitted to a camera varies with the square of the cosine function for the rotation angle. As the polaroid is rotated away from the camera's ideal position, the amount of light received at the camera drops to 50% at 45 degrees and then to nearly zero at 90 degrees away from the ideal position. These intensity differences are predicted by the Law of Malus (Hudson 1982):

$$I = I_o \cos^2\theta \tag{7}$$

where I is the resultant intensity after exiting the system, I_o is the initial intensity of the light entering the system, and theta (θ) is the angle between the incoming light polarization and the polaroid.

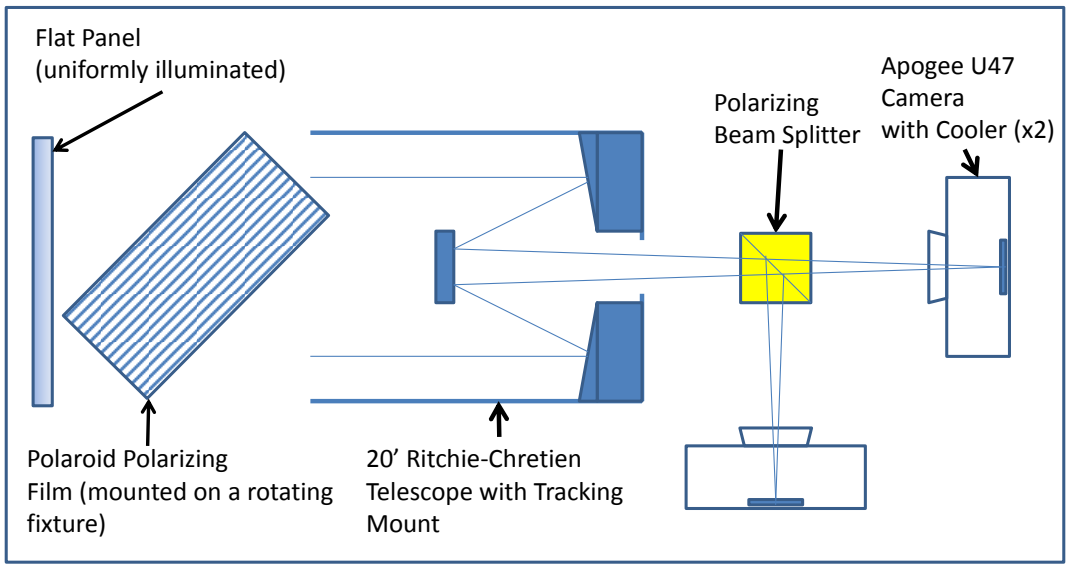

Figure 11. Polarizer characterization setup

Flatman Characterization: Flatness, Polarization, and Stability

In this experiment, a Flat-Man XL panel from AlnitaK Astrosystems was used which features an electroluminescent panel with a screen that evenly distributes the light so it is uniform, unpolarized, and stable at the telescope optical train entrance. It features an XL24 Plexiglass 2447 diffuser that has a spectral response as shown in Figure 12 below. The illumination power can be controlled to produce the desired level of illumination to properly fill the pixel wells for the flat frames. The flat field images then are used to calibrate the raw image data for optical train and CCD pixel sensitivity.

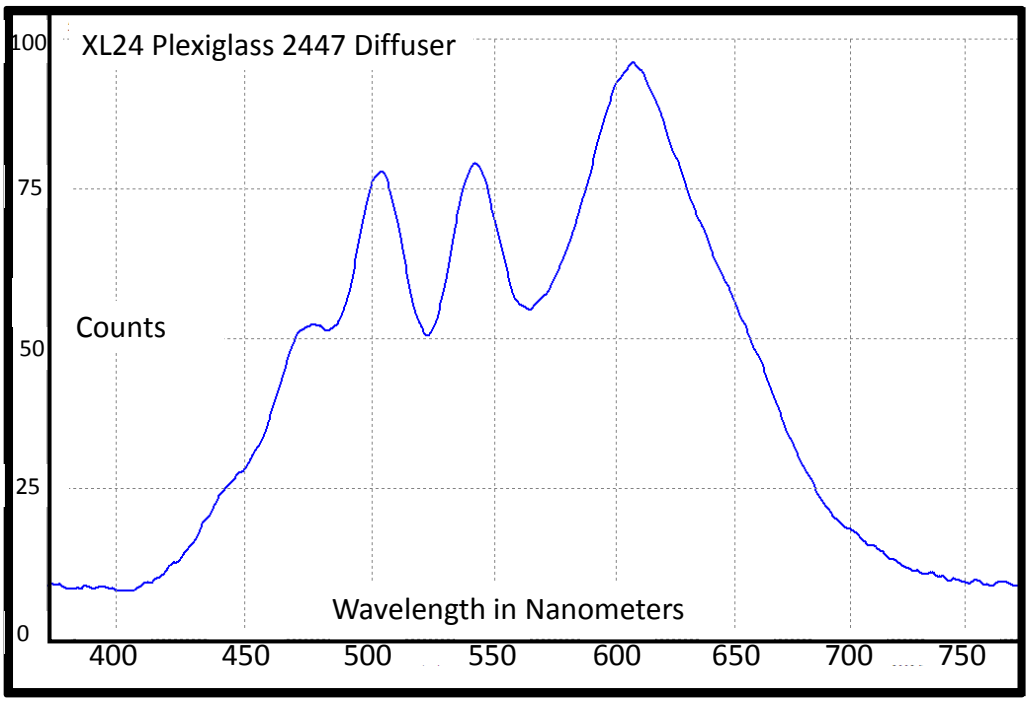

Figure 12. Spectral response of the Alnitak Astrosystems Flat-Man XL panel (optecinc.com 2015)

Three tests were conducted to determine the flatness, polarization, and stability of the illumination from the flat panel. The desire for an accurate polarimeter calibration was for the Flat-Man to be flat, unpolarized, and stable over time to within a few percent. While any errors with the flatness will eventually be removed using the calibration flat frames, this experiment was conducted to validate that the illumination from the flat panel was reasonably flat prior to flat frame calibration. Any polarization of the flat panel illumination will be a small error in the ultimate calibration of the polarimeter so there is a strong desire to validate that the flat panel has a small contribution to the polarization signature. It should be noted however, that the polaroid should be able to reduce any polarization from the flat panel since the polaroid will effectively block most of the polarized light that is not oriented with the polaroid transmission plane. Stability of the

flat panel illumination over time should not contribute significant errors since both cameras will receive illumination that is the correct ratio of the total signal due to the transmission properties of the polaroid.

Flatman Illumination Flatness Test

The flat panel illumination flatness test used the same configuration shown in Figure 11 above which featured the flat panel, polaroid, telescope, beamsplitter, and two cameras. Images were taken with 2 second integration times simultaneously by both cameras. The PFA-NA polaroid was positioned at the zero degree step, the camera coolers were set to -20 C, and the Flat-Man XL panel illumination level was set to 144 on the controller. After calibrating the images with bias and dark frames, an analysis was completed to determine how flat the images were vertically and horizontally in the central $1/9^{th}$ of the frames. Since the telescope tracking controller kept satellite images in the central $1/9^{th}$ of the frames, flatness was measured in this region of the frames. Figure 13 below shows the Camera0 flat frame plot horizontally across the frame. This correlates to a flatness of 3.2%. Figure 14 below shows the Camera0 flat frame plot vertically across the frames. This corresponds to a flatness of 3.3%. Figure 15 below shows the Camera90 flat frame plot horizontally across the frame. This correlates to a flatness of 3.0%. Figure 16 below shows the Camera90 flat frame plot vertically across the frame. This correlates to a flatness of 2.4%. Reviews of the frame diagonals showed similar flatness across the central $1/9^{th}$ of the flat frames. This amount of flatness error can easily be calibrated out using the flat frames.

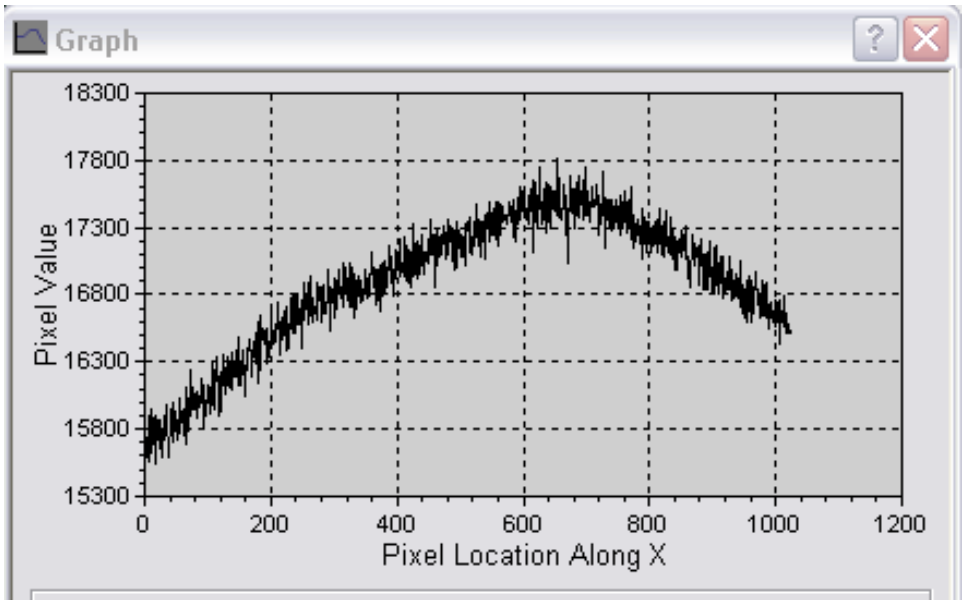

Figure 13. Camera0 flatness across center of the flat frames

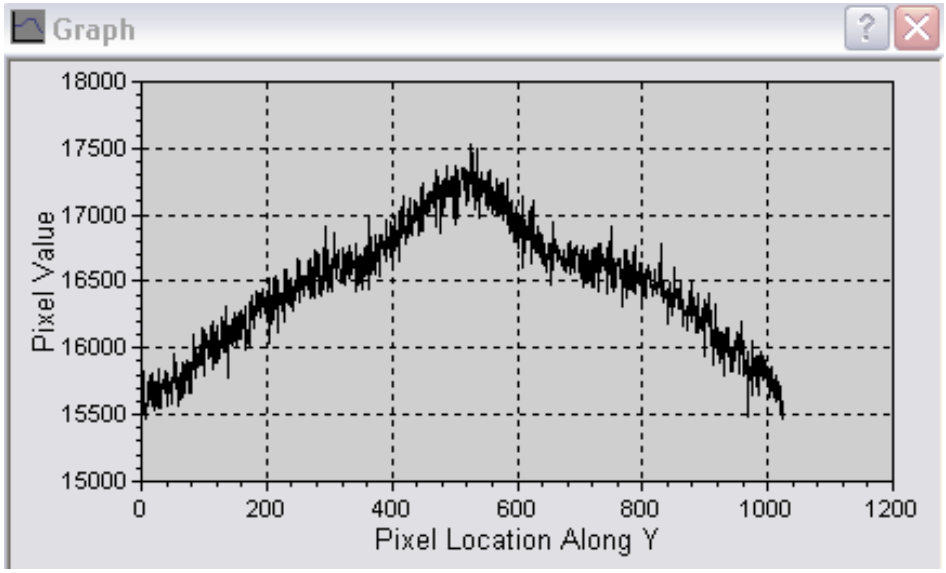

Figure 14. Camera0 flatness down center of the flat frames

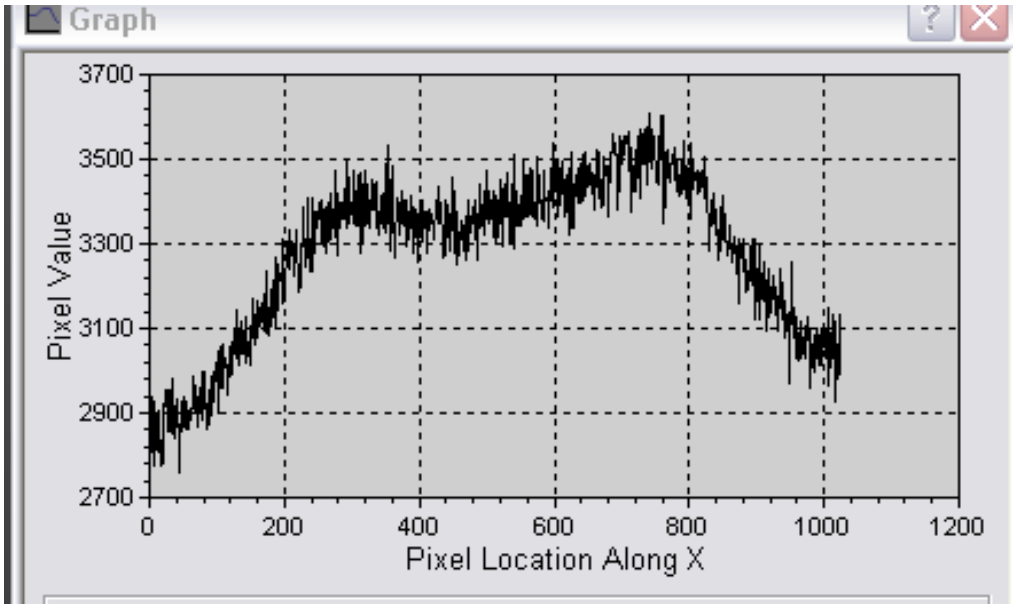

Figure 15. Camera90 flatness across center of the flat frames

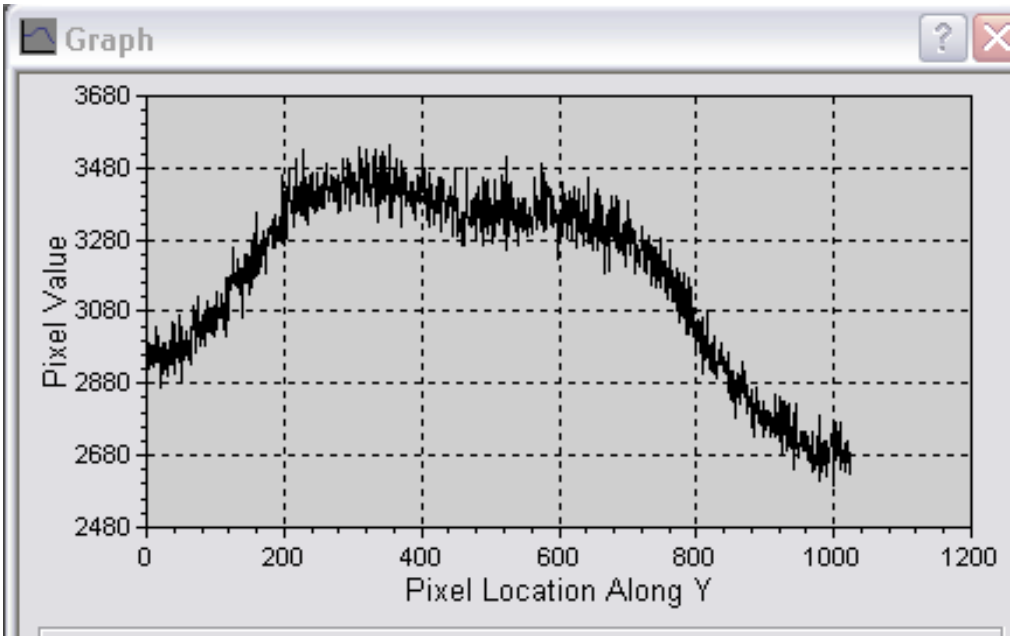

Figure 16. Camera90 flatness down center of the flat frames

Flatman Illumination Polarization Test

The flat panel polarization test used the configuration shown in Figure 17 below which featured the flat panel, polaroid, telescope, filter wheel set to “visible” and only one camera. Notice that the polarizing beamsplitter was removed for this experiment so there was no errors due to the beamsplitter response. Images were taken with a 2 second integration time from the camera at each 10 degree step of the polaroid from 0 degrees to 180 degrees. The camera cooler was set to -20° C and the Flat-Man XL panel illumination level was set to 144 on the controller. After calibrating the images with bias and dark frames, an analysis was completed to determine how much polarization there was in the central $1/9^{th}$ of the frames. Figure 18 below shows how the single camera response varied over the polaroid steps. If there was no polarization, the values should be identical for all polaroid steps. The response below indicates there is either a 3.4% variation in the polarization or there is a combination of illumination polarization and stability errors adding to 3.4%. Since the stability test described below recorded a 1.6% variation in illumination stability, the total polarization error induced by the Flatman was estimated to be 1.8%.

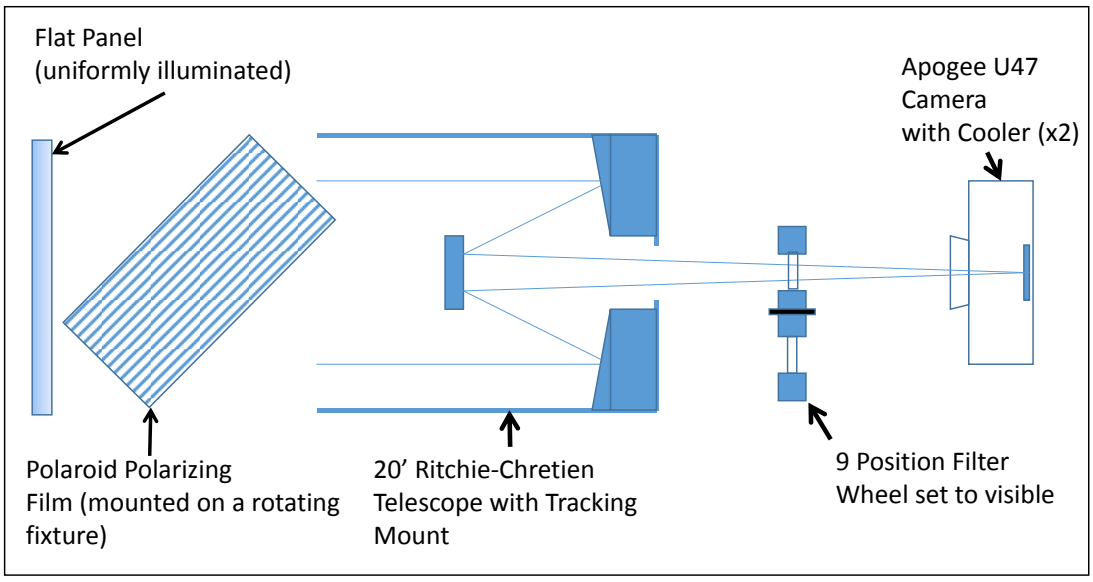

Figure 17. Experimental setup for determining the flat panel polarization and stability

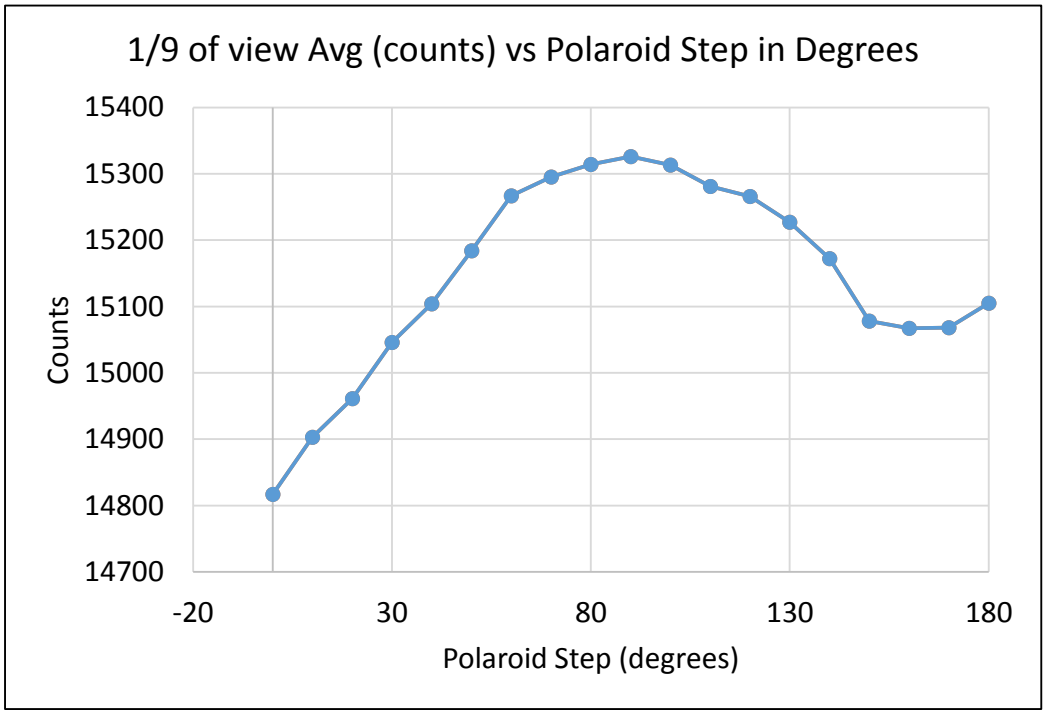

Figure 18. Flat panel polarization test results

Flatman Illumination Stability Test

The flat panel stability test used the configuration shown in Figure 17 above and was performed to determine if the Flat Man XL illumination was stable over time.

Typically the flat frame calibration process of collecting images from both cameras over the polaroid steps takes about 30 minutes so this time was used to characterize the illumination stability. Images were taken once per minute with a 2 second integration time from the camera with the polaroid set to 0 degrees. The camera coolers were set to -20° C and the Flat-Man XL panel illumination level was set to 144 on the controller. After calibrating the images with bias and dark frames, an analysis was completed to determine illumination stability in the central 1/9th of the frames. Figure 19 below shows how the single camera response varied over the 30 minutes. If there was no drift in the illumination output from the flat panel, the values should be identical over the 30 minutes. The response below indicates there was a 1.6% variation in the illumination stability over 30 minutes.

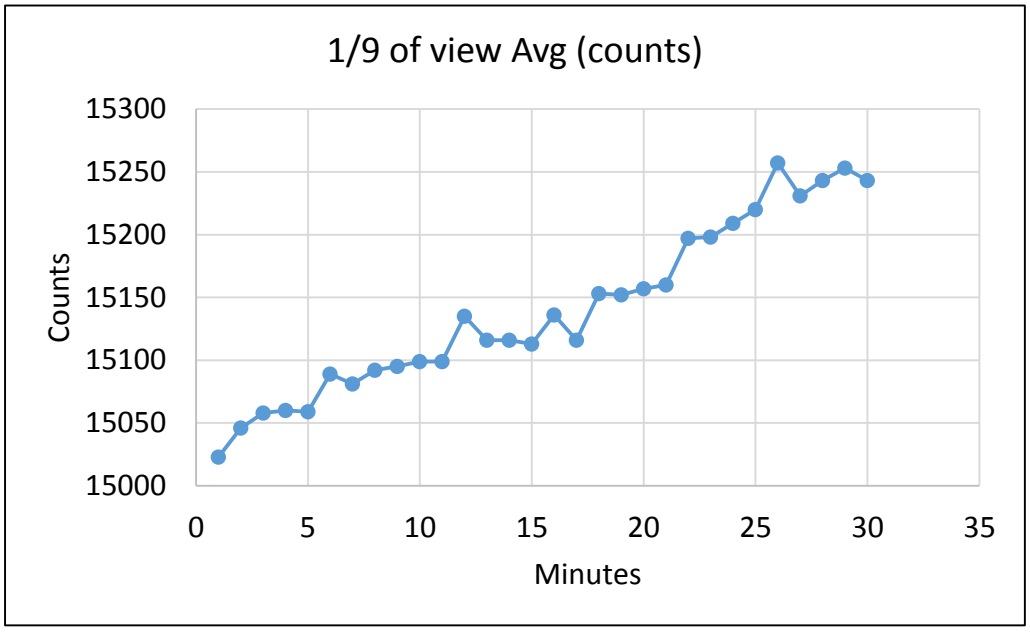

Figure 19. Flat panel illumination stability over time test results

Mueller matrix determination

Tinbergen states that the 4-element Stokes vector describes the flow of electromagnetic energy in terms of its vibration components radiating from a source (Tinbergen 1996). The polarization components of this energy may be altered from their original state when they encounter a medium such as the atmosphere or an object such as the components of an optical train. In order to compare polarization data from one observation session or one instrumentation system to another, the collection system systematic errors must be removed to reveal the actual polarization components incident on the collection system aperture.

In 1943 Hans Mueller introduced the Mueller matrix which may be used to quantify the errors induced by a medium or component even when the signal is only partially polarized. Equation (8) shows that when observing satellite polarization the Stokes vector incident on the instrumentation system, S_{in}, is multiplied by the Mueller matrix, *M*, to give the Stokes vector measured by the detector, S_{out}. Typically each component of an optical train has a particular Mueller matrix that is multiplied together with the other component Mueller matrices in reverse order to determine the overall system Mueller matrix (Tinbergen 1996). Equation (9) from Klinger shows the general form of the Mueller matrix for any polarizer where θ is the angle of the polarizer (Klinger 1990). Equation (10) shows the Stokes vector for light incident on the telescope entrance.

$$S_{out} = M\, S_{in} \tag{8}$$

$$M = \begin{bmatrix} m_{00} & m_{01} & m_{02} & m_{03} \\ m_{10} & m_{11} & m_{12} & m_{13} \\ m_{20} & m_{21} & m_{22} & m_{23} \\ m_{30} & m_{31} & m_{32} & m_{33} \end{bmatrix} = \frac{1}{2}\begin{bmatrix} 1 & cos2\theta & sin2\theta & 0 \\ cos2\theta & cos^2 2\theta & cos2\theta sin2\theta & 0 \\ sin2\theta & cos2\theta sin2\theta & sin^2 2\theta & 0 \\ 0 & 0 & 0 & 0 \end{bmatrix} \tag{9}$$

$$S_{in} = \begin{bmatrix} S_0 \\ S_1 \\ S_2 \\ S_3 \end{bmatrix} \quad (10)$$

While the Mueller matrix estimates for various types of optical components can be found in reference material, this study will determine the entire instrumentation system Mueller matrix experimentally. The system Mueller matrix includes all elements of the optical train and will be used to determine the Stokes vector incident on the instrumentation system. The general method for determining the system Mueller matrix for a polarization state analyzer is described by Chenault (Chenault 1990). Tippets describes a procedure for determining the system Mueller matrix for a 4-channel polarimeter (Tippets 2005). It is advantageous to develop an equation relating the Stokes vector (S_0 and S_1) to the intensities recorded by the two cameras. The derivation below will closely follow Chenault and Tippets with the modifications necessary to apply the procedure to a 2-channel linear polarimeter (Speicher 2014).

Equation (9) reduces to a (2 X 2) Mueller matrix or Analyzer matrix, equation (11) for this experiment since the 2-channel polarimeter can only detect linear polarization at 0 and 90 degrees.

$$\boldsymbol{A} = \frac{1}{2}\begin{bmatrix} a_{0,0} & a_{0,1} \\ a_{1,0} & a_{1,1} \end{bmatrix} \quad (11)$$

An assumption made in this calibration is that the cameras are not sensitive or selective to polarization as indicated by the Flatman illumination testing so that no matter what polarization strikes the FPA pixels, there will be no difference in the camera

intensity or analog-to-digital counts recorded. The detector polarization sensitivity of the camera can be represented by a detection vector, D = [d0, d1], where d0 = 1 and d1 = 0.

$$D = [1 \quad 0] \tag{12}$$

An overall analyzer vector, **A** in equation (13), can be determined that will include the instrumentation polarization and the detector polarization sensitivity by the vector product of D and A. The analyzer vector will be used in equation (8) to convert camera counts from the observation data to the calibrated incident Stokes vectors.

$$\mathbf{A} = D\,A = \tfrac{1}{2}[1 \quad 0]\begin{bmatrix} a_{00} & a_{01} \\ a_{10} & a_{11} \end{bmatrix} = \tfrac{1}{2}[a_{00} \quad a_{01}] \tag{13}$$

The detectors record intensity by outputting analog-to-digital counts that are proportional to the intensity. Intensity can be calculated using the dot product of the analyzer vector, **A**, and Stokes vector of the light incident on the instrumentation, S_{in}.

$$I = \mathbf{A} \cdot S_{in} = \tfrac{1}{2}[a_{00} \quad a_{01}] \cdot \begin{bmatrix} S_0 \\ S_1 \end{bmatrix} = \tfrac{1}{2}\,(a_{00}S_0 + a_{01}S_1) \tag{14}$$

Using equation (14) the overall analyzer vector can be experimentally determined by recording the intensity or analog-to-digital counts on each camera as a function of different incident Stokes vectors. The system of equations (15) and (16) below are linear. The analyzer vectors for each channel convert the incident Stokes vector into a calibrated number of analog-to-digital counts with a correction of instrument polarization systematic errors.

$$\text{Channel 0} \quad \begin{bmatrix} I_{0,0} \\ I_{0,1} \\ \cdot \\ I_{0,18} \end{bmatrix} = \begin{bmatrix} S_{0,0} & S_{0,1} \\ S_{1,0} & S_{1,1} \\ \cdot & \cdot \\ S_{18,0} & S_{18,1} \end{bmatrix} \tfrac{1}{2}\begin{bmatrix} a_{0,0} \\ a_{0,1} \end{bmatrix} \tag{15}$$

Channel 1 $$\begin{bmatrix} I_{1,0} \\ I_{1,1} \\ \cdot \\ I_{1,18} \end{bmatrix} = \begin{bmatrix} S_{0,0} & S_{0,1} \\ S_{1,0} & S_{1,1} \\ \cdot & \cdot \\ S_{18,0} & S_{18,1} \end{bmatrix} \frac{1}{2} \begin{bmatrix} a_{1,0} \\ a_{1,1} \end{bmatrix} \quad (16)$$

Each analyzer vector for a particular channel is then used to construct a matrix called the polarization measurement matrix denoted as **U**. Since there are two channels and two values in the analyzer vectors the polarization measurement matrix will be a 2 X 2 matrix shown below. The polarization measurement matrix may be solved using a least-squares approach with as few as 4 measurements but will be over-determined with the 38 measurements taken in this experiment for each channel.

$$\boldsymbol{U} = \frac{1}{2} \begin{bmatrix} a_{0,0} & a_{0,1} \\ a_{1,0} & a_{1,1} \end{bmatrix} \quad (17)$$

Once the analyzer vectors and thus the polarization measurement matrix is known, the incident Stokes vectors may be determined by inverting the polarization measurement matrix and multiplying by the intensities measured for each of the polarimeter channels. Equation (18) combines equations (15) and (16) so that both polarimeter channels are addressed simultaneously. Equation (19) solves for the incident Stokes vector by inverting the polarization measurement matrix. Equation (20) expands equation (19) into the detailed terms for clarity where S_0 and S_1 are the calibrated incident Stokes vectors, the first row of a's are the channel 1 analyzer matrix, the second row of a's are the channel 2 analyzer matrix, I_0 is the channel 1 measured counts, and I_1 is the channel 2 measured counts. Equation (20) is used to calculate the calibrated Stokes vector taking into account the polarization errors due to the instrumentation assuming the detectors are not polarization sensitive. It should be noted that the measured intensities

(counts) have been corrected for FPA bias and FPA thermal noise as described in the previous sections prior to their use in equation (19).

$$I = \mathbf{U}\, S_{in} \tag{18}$$

$$S_{in} = \mathbf{U}^{-1}\, I \tag{19}$$

$$\begin{bmatrix} \boldsymbol{S_0} \\ \boldsymbol{S_1} \end{bmatrix} = \frac{1}{2} \begin{bmatrix} a_{0,0} & a_{0,1} \\ a_{1,0} & a_{1,1} \end{bmatrix}^{-1} \begin{bmatrix} I_0 \\ I_1 \end{bmatrix} \tag{20}$$

Solving for the polarization measurement matrix, U

According to Hornbeck, there are two general methods for solving systems of equations, the direct method and the iterative method (Hornbeck 1975). Direct methods such as Gauss-Jordan Elimination will yield answers after a predictable number of operations. Iterative methods such as Gauss-Seidel or Levenberg-Marquardt can require a large number of iterations in order to produce an accurate answer but can handle complex non-linear problems. Leveraging the work of Tippets, the Levenberg-Marquardt iterative technique was chosen and configured to solve for both polarimeter channel analyzer vectors simultaneously, yielding the Polarization Measurement matrix **U** (Tippets 2005). This is implemented in a non-linear least squares technique which requires an initial estimation of the solution. The initial guess must be somewhat close for a large set of equations which in this case is 38 total equations. An estimation model shown in equation (21) was developed from equation (9) and (14) above for a general polarizer which includes the estimated angle of the polarizer in each channel (ϕ) and the estimated angle of the polaroid (θ) used to produce the input Stokes vector at the instrumentation (telescope) aperture. The estimated angle of the polarizer (ϕ) in each channel is assumed

to be 0 or 90 degrees depending on the channel. This equation also includes the flat panel polarization term.

$$Channel\ Intensity = \frac{1}{2}[S_0 a_0 + S_0 a_0 cos(2\theta)\ cos(2\emptyset) + S_0 a_0 sin(2\theta)\ sin(2\emptyset)] \quad (21)$$

The Levenberg-Marquardt algorithm computes a figure of merit for each iteration and then compares that figure of merit to the previous and continues the iteration process until a desired solution is reached which is evident by a small difference (residual) in the two figure of merits. See Appendix B for a listing of the MathCad algorithm from Tippets used to calculate the **U** calibration matrix for this research.

Calibration Results

A preliminary and final set of calibration data was collected on December 29th, 2013 and March 5th, 2015 using the USAFA Mobile 1 telescope facility. A total of 10 bias frames were taken for each camera at zero second exposure time with the shutter closed. Each focal plane array (FPA) employs a cooler that was operating to a set point of -20 degrees C. Bias frames were used to determine the zero point of each FPA pixel.

Next, 10 dark frames were taken for each camera at 10 different exposure settings with the shutter closed to allow calibration over a wide range of exposure times in the future. The exposure times included 10 seconds for the preliminary collect and 20 seconds for the final data collection activity. Dark frames were used to account for the amount of dark current that is generated by Charge Coupled Device (CCD) even when no light impinges on the FPA.

Finally, 10 flat frame images were taken with each camera while the telescope aperture was exposed to a uniformly lit flat panel. Since the flat panel had only one brightness setting which was full power due to a software issue for the initial 2013 calibration, any exposure time over 0.1 seconds saturated the FPA. For the final calibration conducted in 2015, the Flatman software had been fixed so a lower flat panel illumination level was used to ensure a two-second integration time could be used. This longer integration time was desired so that the mechanical shutter opening time would not be a factor in the calibration procedure.

Between the flat panel and telescope input aperture was a polaroid on a turntable with degree markings to allow the entire polarimeter optical train to be calibrated for both vertical and horizontal polarization inputs. Flat panel images calibrate the entire optical train which includes any dust and also pixel sensitivity. As the polaroid was turned in 10 degree increments, response to the changing polarization input was recorded to allow calibration of future images. As expected, the response on each camera varied sinusoidally through rotation of the input polaroid. Camera0 is the FPA that collects light that is transmitted through the polarizing beam splitter. Camera90 is the FPA that collects light that is reflected at 90 degrees from the input direction. Figure 20 shows a plot of the Malus curves using normalized and calibrated flat panel data.

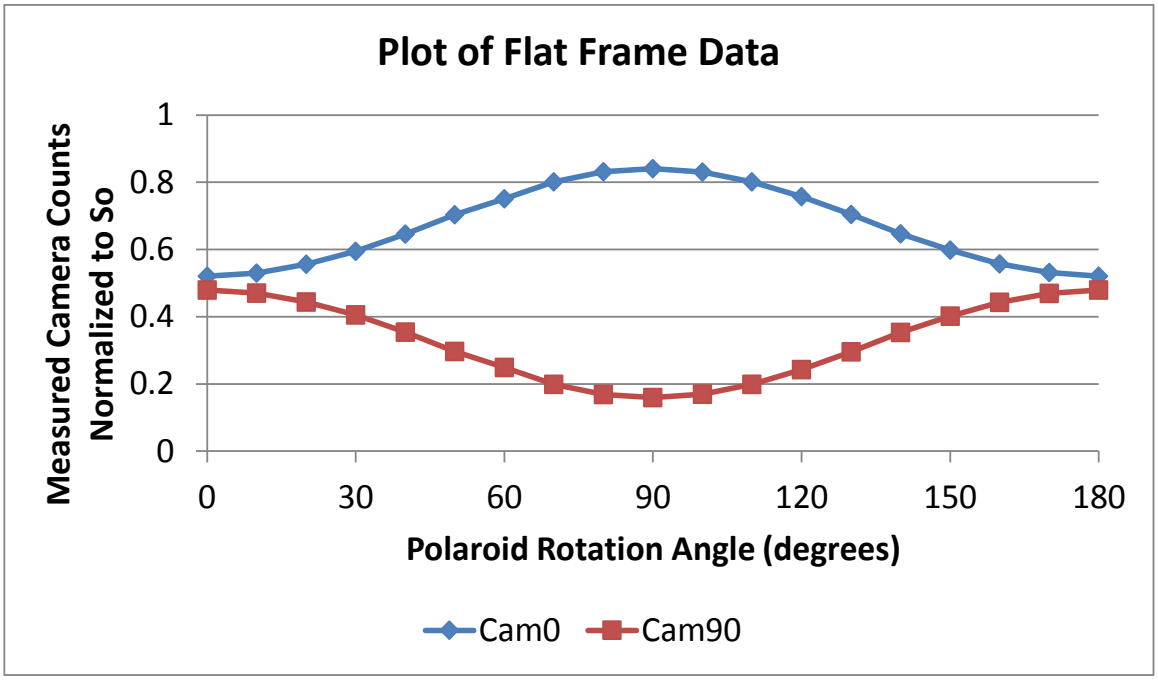

Figure 20. Malus curves using the calibrated flat panel data collected March 5, 2015

The Polarization Measurement matrix, ***U***, was determined using the Levenberg-Marquardt algorithm to solve for the A matrix in equation (15) and (16). The Stokes parameters S_0 and S_1 are shown in equation (24) below as a function of the ***U*** and I matrices.

$$\boldsymbol{U} = \begin{bmatrix} 0.329938 & 0.152459 \\ 0.704129 & -0.189426 \end{bmatrix} \tag{22}$$

$$\boldsymbol{W} = \boldsymbol{U}^{-1} = \begin{bmatrix} 1.115255 & 0.897614 \\ 4.145601 & -1.942527 \end{bmatrix} \tag{23}$$

$$\begin{bmatrix} S_0 \\ S_1 \end{bmatrix} = \begin{bmatrix} 1.115255 & 0.897614 \\ 4.145601 & -1.942527 \end{bmatrix} \begin{bmatrix} I_0 \\ I_1 \end{bmatrix} \tag{24}$$

With the relation of intensity to the Stokes parameters above in equation (24), only the Camera0 and Camera90 intensities I_0 and I_1 in camera counts need to be entered

to compute Stokes vectors S_0 (total intensity) and S_1 (linear polarization) for a set of satellite images at a particular time.

In order to validate that the equation above is a good fit, the original flat panel intensity data was entered into equation (24). This S_1 data was plotted against the polaroid angles used to take the data. In this way, it was proven that the original Camera0 and Camera90 intensity data fed into the final calibration algorithm yielded the expected normalized linear polarization S_1 values. For example, in Figure 22 below it can be seen that the camera intensity data collected while the polaroid was at the 0 degree position yielded a normalized S_1 value of approximately 1.0 as expected which correlates to S-polarization or horizontal polarization. Similarly, Camera0 and Camera90 intensity data fed into the calibration algorithm at a polaroid position of 90 degrees yielded a normalized S_1 value of approximately -1.0 as expected which correlates to P-polarization or vertical polarization. In other words, if a set of satellite intensity data from Camera0 and Camera90 were fed into the calibration algorithm, the expected results are obtained. It can also be seen in Figure 21 below that the calibrated data deviates from the "perfect" modeled Malus curve by +/- 5 percent or a value of +/- 0.05 for a normalized S_1 Stokes parameter. Thus, as long as the signal-to-noise ratio of the collected data is adequate at 100 or higher, it is believed that the errors should be no more than 5 percent.

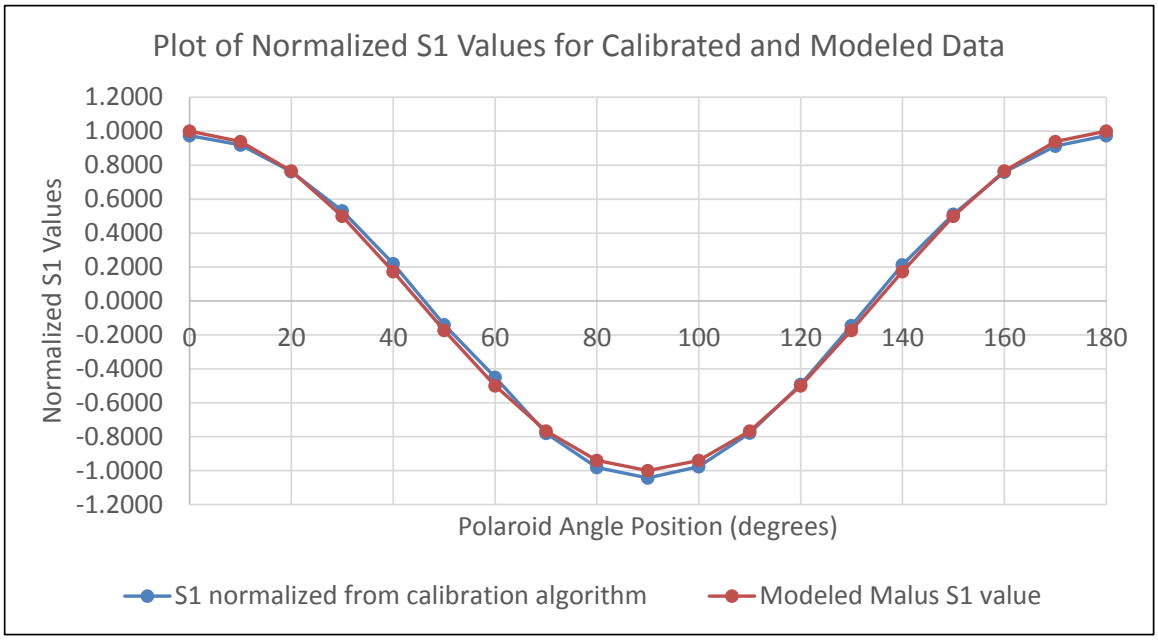

Figure 21. A comparison of calibrated S_1 data using the original flat panel camera inputs and the modeled "perfect" Malus curve

It should be noted that the calibration procedure described for pixel sensitivity and optical train abnormalities should be repeated each time the polarizer or telescope optics are changed in any way. If the polarizer and optics are unchanged, the procedure should be repeated every week or so since dust can settle on optics relatively quickly which affects the calibration. While the FPA zero bias and thermal noise error components are not expected to change appreciably over longer periods of time, it is recommended to take the data prior to each observation session since it only requires minutes to accomplish.

CHAPTER FOUR: DATA COLLECTION

There were two separate data collection campaigns executed. A preliminary set of data was collected on five target satellites using the United States Air Force Academy Mobile-1 telescope on December 30th, 2013. Each satellite was imaged five times every 15 minutes for a 10 second exposure using the dual camera polarimeter. Approximately 3 hours of data were collected until the tracking mount registered an error that could not be corrected at the time. The purpose of this initial data set was to validate collection and processing procedures. This activity also established that the Stokes S_0 and S_1 parameters were potentially unique for each satellite.

The final sets of data were collected on eight target satellites using the United States Air Force Academy Mobile-1 telescope on three separate nights. Each satellite was imaged two times every 15 minutes for a 20 second exposure using the dual camera polarimeter. Approximately 11 hours of data were collected on each night to establish repeatability of the optical signatures.

Target Selection

Initial Target Set

Since the purpose of this initial data collection was to validate the study concepts and procedures, five geostationary satellites were selected that included five different spacecraft buses to show that they all had unique optical signatures with respect to intensity and polarization. Details of those spacecraft can be seen in Table 4 below.

	S/C Vendor	S/C Bus	Launch Date
Directv-4S	Boeing	BSS-601HP	11/2001
Directv-9S	Space Sys Loral	LS-1300	10/2006
SES-1	OSC	Star-2.4	4/2010
Directv-12	Boeing	BSS-702	12/2009
AMC-18	Lockheed	A2100A	12/2006

Table 5. Initial list of geostationary satellites imaged for polarization signatures

Final Target Set

A total of eight geosynchronous satellites were selected for the final study in order to encompass many different satellite buses and to allow a comparison of several of the same buses over time. In Table 6 below it can be seen that the eight satellites include five different buses and three sets of the same bus. The experiment will be able to contrast the polarization of different buses and the same buses launched at a different time to see if the signature will enable classification of each satellite. Since the data was collected over a few months, it was possible with this experiment to determine how the polarization signature changed over time. All eight satellites selected are high in the sky relative to the United States Air Force Academy located in Colorado Springs, Colorado. Since the satellites are located within a few degrees of each other in the geostationary belt

at an elevation of approximately 44 degrees, slew time from satellite to satellite was only a few seconds.

In Figure 22 below, it can be seen that the targets selected are communications satellites which have a similar architecture with two solar arrays and a central bus that houses the payload antennas. Each of these satellites point their payload dishes towards Earth typically to a fixed point and thus are three-axis stabilized. All of these satellites have solar arrays that track the sun in order to collect power.

	Spacecraft Vendor	Spacecraft Bus	Launch Date
Directv-4S	Boeing	BSS-601HP	11/2001
AMC-15	Lockheed	LM A2100	10/2004
Directv-8	Space Sys Loral	LSS 1300	5/2005
Directv-9S	Space Sys Loral	LSS-1300	10/2006
AMC-18	Lockheed	LM A2100A	12/2006
Directv-10	Boeing	BSS-702	7/2007
Directv-12	Boeing	BSS-702	12/2009
SES-1	OSC	Star-2.4	4/2010

Table 6. Final list of geostationary satellites imaged for polarization signatures

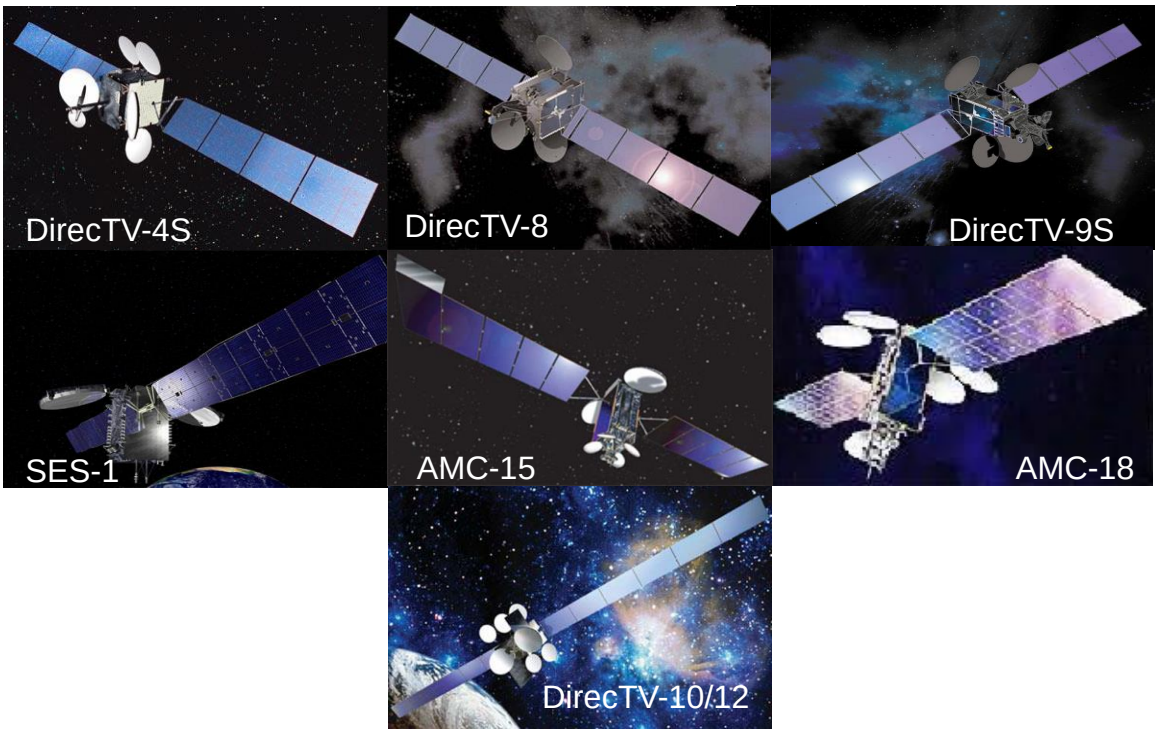

Figure 22. Artist renderings of the eight target satellites (Image of Satellite URLs, 2015)

Solar Phase Angle

Since it is expected that the polarization signature of a satellite will change as the sun illuminates different parts of the bus, the solar phase angle is a key parameter in understanding the data collected. Solar phase angle is the angle measured from the satellite being observed to the sun and to the observer; it is analogous to the moon phases. In Figure 23 below it can be seen that spacecraft positions P2, P3, and P4 will provide the ground observer with views of the front of the solar arrays at many different sun angles. From positions P1 and P5 it may also be seen that the Earth observer gets an edge-on view of the solar array. With a solar phase angle of 0 degrees, the observer typically gets the highest reflected optical signal intensity from the satellite. Observation data on February 8th, February 14th, and March 21st, 2015 validated this assumption. However,

the polarization signal should be independent of the total signal received and is more a function of the materials being illuminated.

Another feature from Figure 23 is that an Earth observer usually sees the payload and antennas since most payloads and communication antennas are pointed to the Nadir position at Earth. Figure 24 below shows the actual solar phase angle from Directv-4S to the Air Force Academy observatory and to the sun on February 8th, 2015. Due to the difficulties of collecting satellite images at dusk and dawn, the solar phase angles for this study were limited to less than 100 degrees. The solar phase angle never reaches zero degrees during these particular data collects because of seasonal variations caused by the earth's tilt with respect to the sun. Observer latitude will also affect the solar phase angle since they may not be located in the ecliptic plane as implied by the two-dimensional Figure 23 representation.

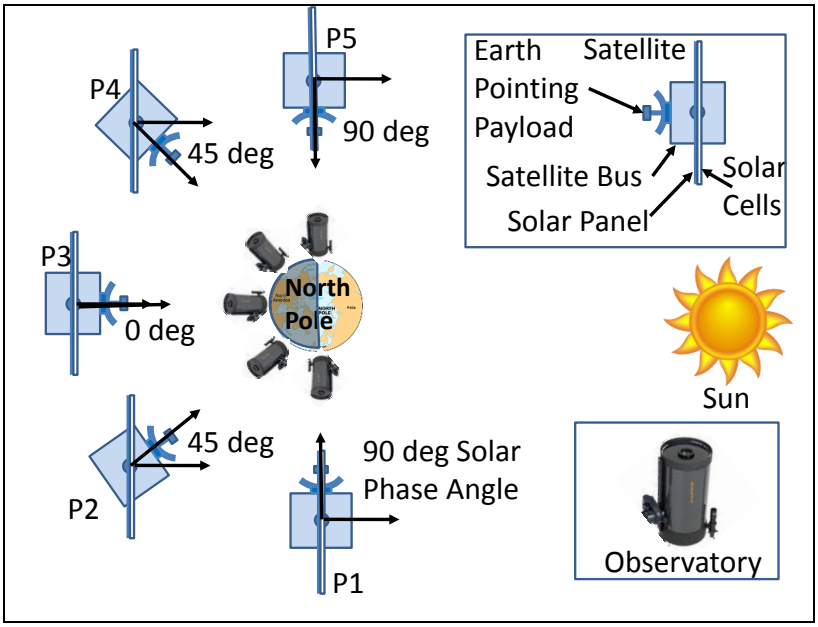

Figure 23. Solar phase angle geometry

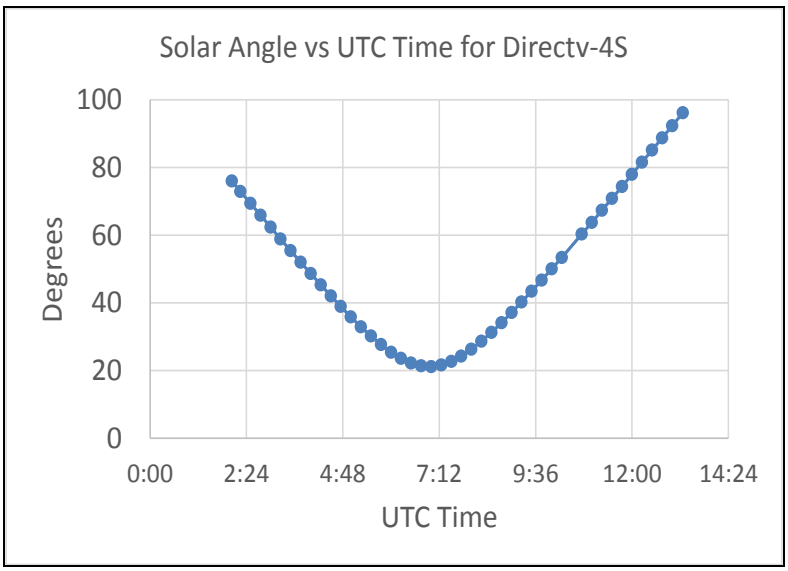

Figure 24. Solar phase angle for Directv-4S on February 8, 2015

A recent study by Cognion predicted and measured the solar flux from various satellites based on the solar phase angle (Cognion 2013). An interesting finding was that the backside of the solar arrays can yield a significant flux component that originates as illumination from Earth albedo or "earthshine". While the window of time to collect earthshine off the backside of a solar array is small due to the required geometry of solar phase angles greater than 90 degrees, thermal treatments typically used on solar array back sides are of a dielectric nature and may provide interesting polarization signatures for study.

Solar phase angle for this study was calculated by loading the satellite Two-Line Element (TLE) sets along with the date and times into a software package called Satellite Tool Kit (STK). STK generated a solar phase angle report in degrees on a minute-by-minute basis for the date and time of the data collections. This report was then manually merged with the calculated S_0 and S_1 Stokes parameters so the values could be plotted.

Data Collection CONOP

As mentioned previously, the initial data collection activity from December 30th, 2013 provided some key lessons that were used to improve the final data collection process. These findings are described below (Speicher 2014):

1. An initial image integration time of 10 seconds was too short since the pixel counts were only 5% of the full scale CCD 65,000 counts and thus not in the desired linear range of measurements. An integration time of 20 seconds was used during the final data collection activities which brought the CCD pixel counts into the linear range. This integration time also allowed the pixel counts to stay below the saturated levels during the collects at solar phase angles near zero degrees which are typically the brightest of the night.
2. During the initial data collection, five images of each spacecraft were collected to ensure that there was at least one image that did not have a star streak interfering with the satellite signal. Analysis of the data concluded that it was only necessary to collect two images for each satellite to produce at least one satisfactory data point without interference from star streaks. This helped reduce the time necessary to collect data on each satellite. On a few occasions during the final data collection activities it was noted that a star streak was interfering with the satellite data so a third image was manually commanded which provided satisfactory data.
3. Each satellite was imaged five times every 15 minutes during the December 20th, 2013 data collection activity. The data was fairly consistent during the

five 10-second data sets taken one right after the other. Another finding was that collecting data every 15 minutes did capture adequate fidelity of the optical signature since it did not change significantly during 15 minutes.

With these lessons shaping the CONOP, three sets of data were collected on the eight target satellites listed in Table 5 above using the USAFA Mobile-1 telescope on February 8th, February 14th, and March 21st, 2015. Each satellite was imaged twice every 15 minutes for a 20 second exposure using the dual camera polarimeter (Speicher 2015). Approximately 11 hours of data was collected on each night to allow for several different comparisons of the data. Since the polarimeter has two channels and thus two cameras, two separate sessions of Maxim DL were used to collect the camera Focal Plane Array (FPA) data (cyanogen.com 2015).

At the top of the hour and every 15 minutes after that, a set of data was collected by manually commanding the telescope to slew to a target using the existing telescope control software (RCOS). Next, Maxim DL was configured to append the name of the satellite onto the data file. Finally both instances of Maxim DL were manually commanded to take the two, twenty second images. Both cameras were taking images simultaneously within approximately one second. Although two images were taken, only one image from each camera was used in the study based on which image was the best with respect to star streak interference. Only images taken simultaneously were used. Once two images were collected on a satellite, the telescope was manually commanded to slew to the next satellite where the process described above was performed again. Including telescope slew time, configuring Maxim DL, and the actual imaging time, a

complete data collection on all eight satellites took approximately 8 minutes. Roughly seven minutes later the entire process was repeated. In future data collects, the telescope slewing and image collection will be automated so the operator does not have to manually perform all the operations.

Data Processing

Frame Calibration

Once the raw data was collected from the polarimeter cameras, each frame was manually assessed to determine which of the two 20-second exposures had the best data with no interfering star streaks. While each satellite was imaged 80 to 88 times in a night for a total of 700 images, only half of these were calibrated and used in the study since only one image was required every 15 minutes to properly characterize the optical signature.

After the highest quality raw frames were selected, they were calibrated on a pixel-by-pixel basis with respect to pixel bias, dark current, and pixel sensitivity. This was accomplished using the previously collected ten bias frames, dark frames, and flat frames for each camera. These sets of ten bias, dark, and flat frames were averaged together to make a master bias, master dark, and master flat frame for each camera that was used to calibrate all the raw data images. A software package called Maxim DL was used to build the master frames and calibrate the raw images. Figure 25 below shows the calibration process for each set of frames. Camera0 is the camera that collects vertically or P-polarized light that passes straight through the beam splitting cube. Camera90 is the

camera offset by 90 degrees that collects the horizontally or S-polarized light that is reflected off the beam splitting cube dielectric cement plane.

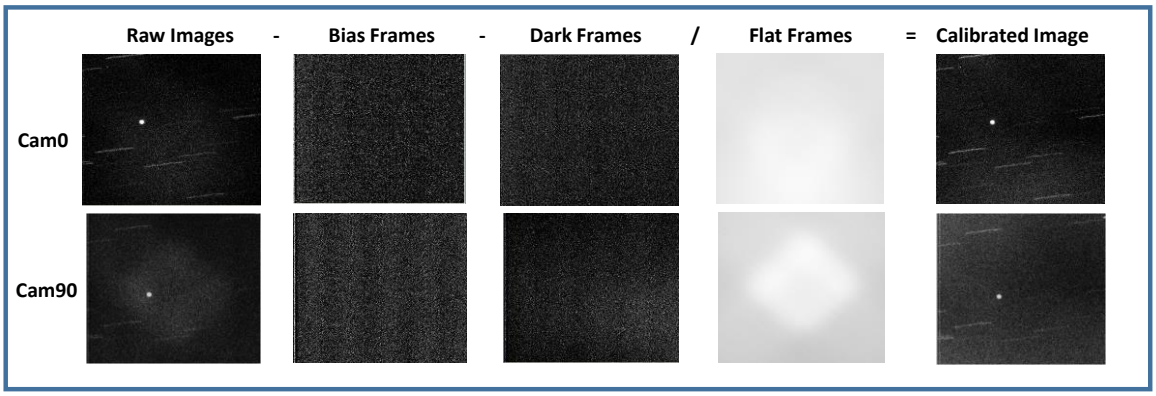

Figure 25. Processing of two simultaneous calibrated images of Directv-4s taken from the two polarimeter cameras

Figure 26 below shows two calibrated frames taken of SES-1 by both of the polarimeter cameras. It can be seen that the unresolved target satellite in the center of the frame is surrounded by stars that streak due to the 20 second exposure since the telescope is tracking the satellite.

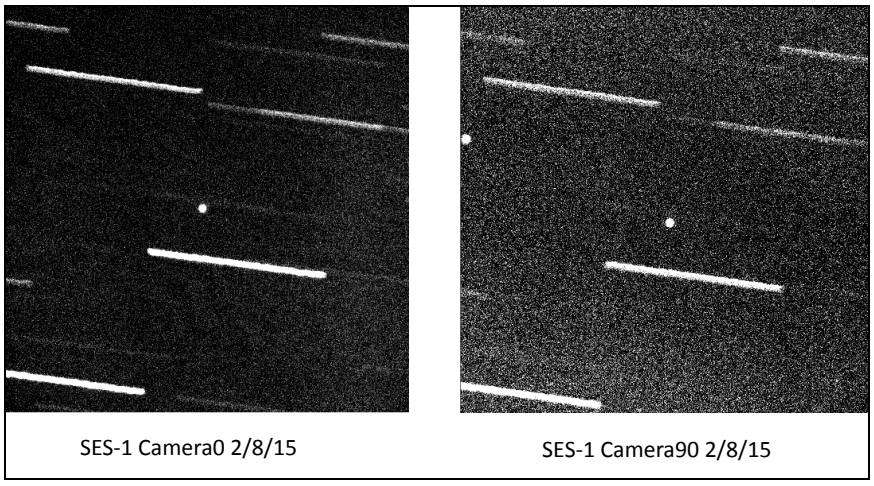

Figure 26. Two simultaneous images of SES-1 taken by the two channel polarimeter

Maxim DL was also used to extract the intensity of the satellite signal from each calibrated image. This was accomplished by first centering each satellite image in a

movable aperture. Each pixel count in the aperture was added together for a total pixel count. Next, Maxim DL computed the background noise in a small annulus surrounding the aperture. Finally, Maxim DL subtracts the background noise from the integrated satellite intensity so that the desired signal was calibrated with respect to background noise. In this manner, if there was a high background noise floor, the satellite signal was calculated so it would not contain an artificially high intensity. See Figure 27 below for an example screenshot of this procedure. Camera0 in Figure 27 recorded a calibrated intensity of 216,437 counts by integrating all the satellite pixels in the smallest aperture over the 20 second exposure and subtracting out the background noise. Also note that the Signal-to-Noise ratio "SNR" in the figure below is 339 which is good. Camera90 recorded an intensity of 77,419 counts for SES-1 from the image in Figure 26 above.

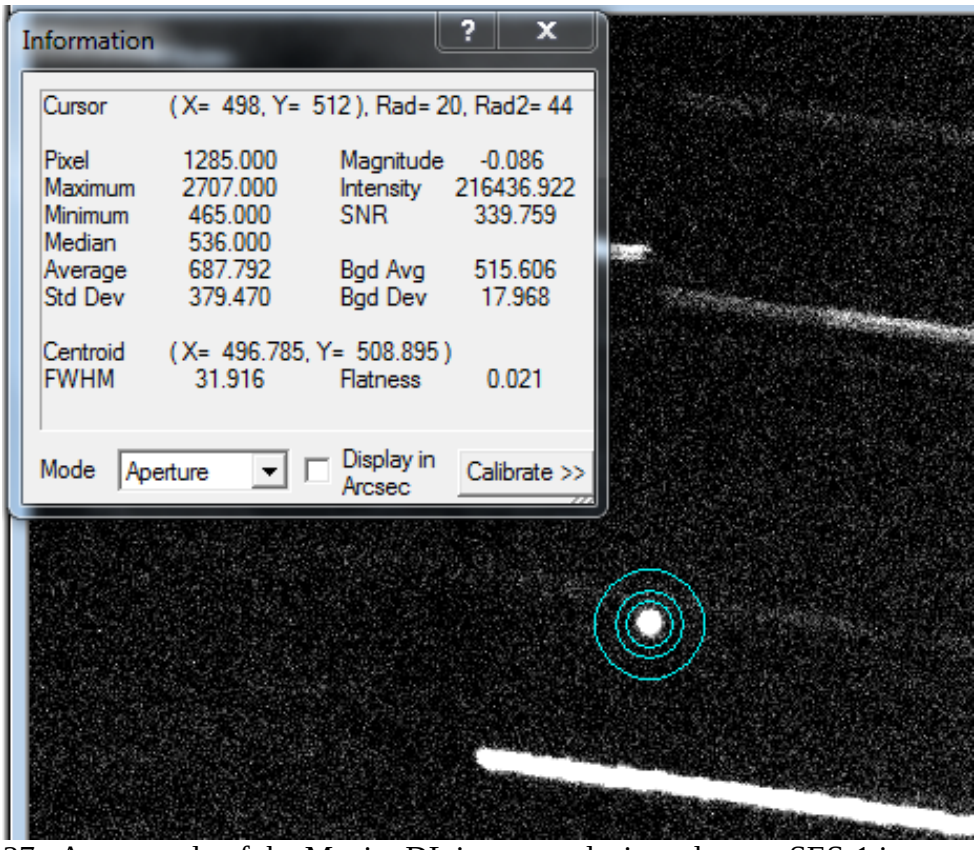

Figure 27. An example of the Maxim DL image analysis tool on an SES-1 image

Polarization Determination

After the integrated intensity of each satellite image was determined for Camera0 and Camera90, they were substituted into equation (24) for I_0 (Camera0) and I_1 (Camera90) in order to calculate the Stokes parameters S_0 and S_1. Equation (24) relates the measured intensities to the Stokes parameters directly using the Mueller calculus described earlier. Recall that the Mueller matrix accounts for errors in the instrumentation system and was determined experimentally using the flat panel and polaroid. When equation (24) above is solved for I_0 = 216,437 and I_1 = 77,419 counts, the Stokes parameters are as follows: S_0 = 280,619 counts and S_1 = -99,486 counts. Normalizing S_1 by S_0 yields S_1 = -99,486 / 280,619 = -0.35. Total intensity and linear

polarization (-1.0 to 1.0) were calculated with each data set for the satellites as described above and plotted against UTC time and solar phase angle to determine satellite signatures and trends.

CHAPTER FIVE: RESULTS

Comparison of S_0 Total Intensity Data

Stokes parameter S_0 represents the total satellite signal or intensity for each 20 second image integration time. It is expected that the satellite intensity will be a minimum at high solar phase angles and a maximum at low solar phase angles. See Figure 24 for the observation geometry. At high solar phase angles the solar arrays are edge-on to the observer so there is little solar flux from the solar panels reflecting to the observer. The analysis below will look at intensity variations for the same bus over time and variations between the different satellites. It should be noted that on 3/21/15 there was a 72 minute eclipse period for the satellites so no observations were taken during that time since the satellites were not lit by the sun due to the Earth's shadow.

In order to compare the linear polarization signals statistically from satellite to satellite, the Pearson Correlation Coefficient was calculated and compared between each set of the satellites with the same bus and between Directv-4S and SES-1 which are different buses. The Pearson Correlation Coefficient, r, is calculated using equation (25) below (McClave and Dietrich 1985):

$$r = \frac{(\sum xy) - \frac{(\sum x)(\sum y)}{n}}{\sqrt{\left((\sum x^2) - \frac{(\sum x)^2}{n}\right)\left((\sum y^2) - \frac{(\sum y)^2}{n}\right)}} \quad (25)$$

where *x* is a value in an array, *y* is a value in another array, and *n* is the number of *x* and *y* values in the arrays. There must be an equal number of values in both arrays that are being compared for correlation. Values of the Pearson Correlation Coefficient vary from 1.0 for a strong positive correlation to -1.0 for a strong negative correlation. Values near 0.0 indicate little or no correlation.

Directv-8 and Directv-9S (LSS 1300 Bus) S_0 Data

Figure 28 below shows plots of total intensity (camera counts) and solar phase angle vs UTC time for Directv-8 and Directv-9S during the three nights of observations (2/8/15, 2/14/15, and 3/21/15). The last two plots show all three nights of intensity data for each satellite. It can be seen that the signatures had a similar shape for both satellites, but were not consistent for the same satellite over time when analyzing the maximum intensity values. It should be noted that the Directv-8 main spike is wider than the main spike for Directv-9S. This feature could potentially aid in classification. Since both satellites have the same bus design from Loral Space Systems (LSS 1300) and similar intensity signatures, it would be difficult to differentiate the two with confidence.

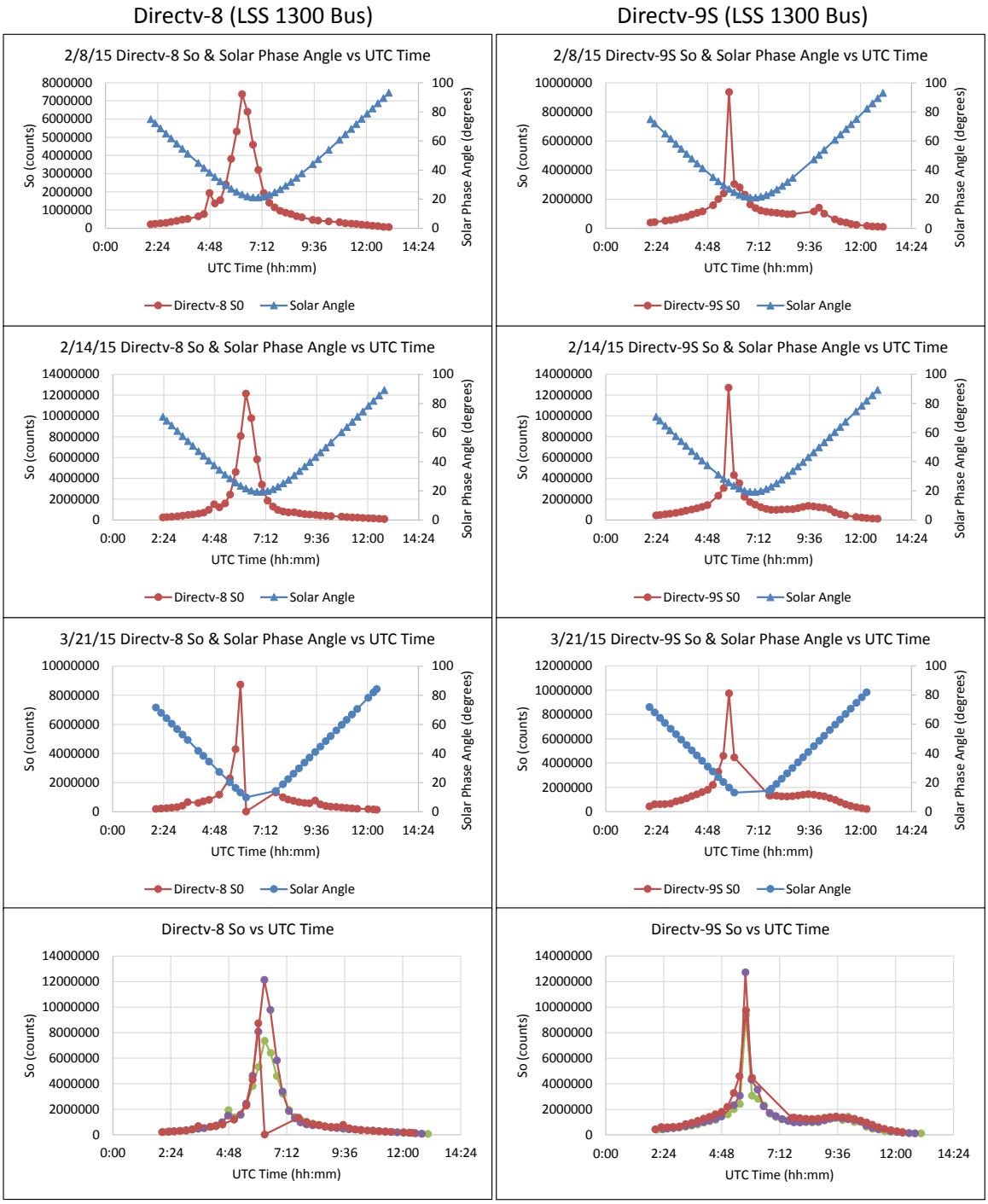

Figure 28. Total intensity, S_0, and solar phase angle for Directv-8 and Directv-9S collected February 8th, February 14th, and March 21st, 2015

Table 7 below shows the Pearson Correlation Coefficient for S_0 when comparing Directv-8 to itself, Directv-8 to Directv-9S, and Directv-9S to itself over the various nights. The green boxes are expected to correlate well since they are the same satellite and the red boxes are expected to have low correlation since they are different satellites. Correlation data for the same satellite on different nights worked as expected with values of 0.98. Correlation of the different satellites is lower as expected at 0.43 or less. The boxes noted as "eclipse" mean that the data cannot be compared since there was an eclipse on the third night which led to a different number of data points than for the first two nights. The Pearson Correlation Coefficient behaved well in that the same satellite had highly correlated data and the different satellites had low data correlation.

	Directv-8 LSS 1300 2/8/15	Directv-8 LSS 1300 2/14/15	Directv-8 LSS 1300 3/21/15	Directv-9S LSS 1300 2/8/15	Directv-9S LSS 1300 2/14/15	Directv-9S LSS 1300 3/21/15
Directv-8 LSS 1300 2/8/15	X					
Directv-8 LSS 1300 2/14/15	0.98	X				
Directv-8 LSS 1300 3/21/15	Eclipse	Eclipse	X			
Directv-9S LSS 1300 2/8/15	0.43	0.35	Eclipse	X		
Directv-9S LSS 1300 2/14/15	0.37	0.30	Eclipse	0.98	X	
Directv-9S LSS 1300 3/21/15	Eclipse	Eclipse	0.27	Eclipse	Eclipse	X

Table 7. Pearson Correlation Coefficients for Directv-8 and Directv-9S S_0

AMC-15 and AMC-18 (LM A2100 Bus) S_0 Data

Figure 29 below compares the intensity plots and solar phase angle of AMC-15 and AMC-18 during the three nights of observations. The last two plots show all three nights of intensity data for each satellite. It is interesting to note that the maximum intensity of the LM A2100 buses occurred at least an hour prior to the smallest solar phase angle. Since both satellites have the same bus design from Lockheed Martin (LM A2100), it would be difficult to differentiate the two due to the similar intensity plots over time. It should also be noted that the maximum values on the three different nights were not consistent on either satellite. An additional feature occurs on AMC-18 during the 3/21/15 data set in that a second major peak can be seen in Figure 30 below. It is interesting to note that the first peak on the 3/21/15 AMC-18 data is very similar to the peaks noted on 2/8/15 and 2/14/15. Analysis of the second peak will require more data.

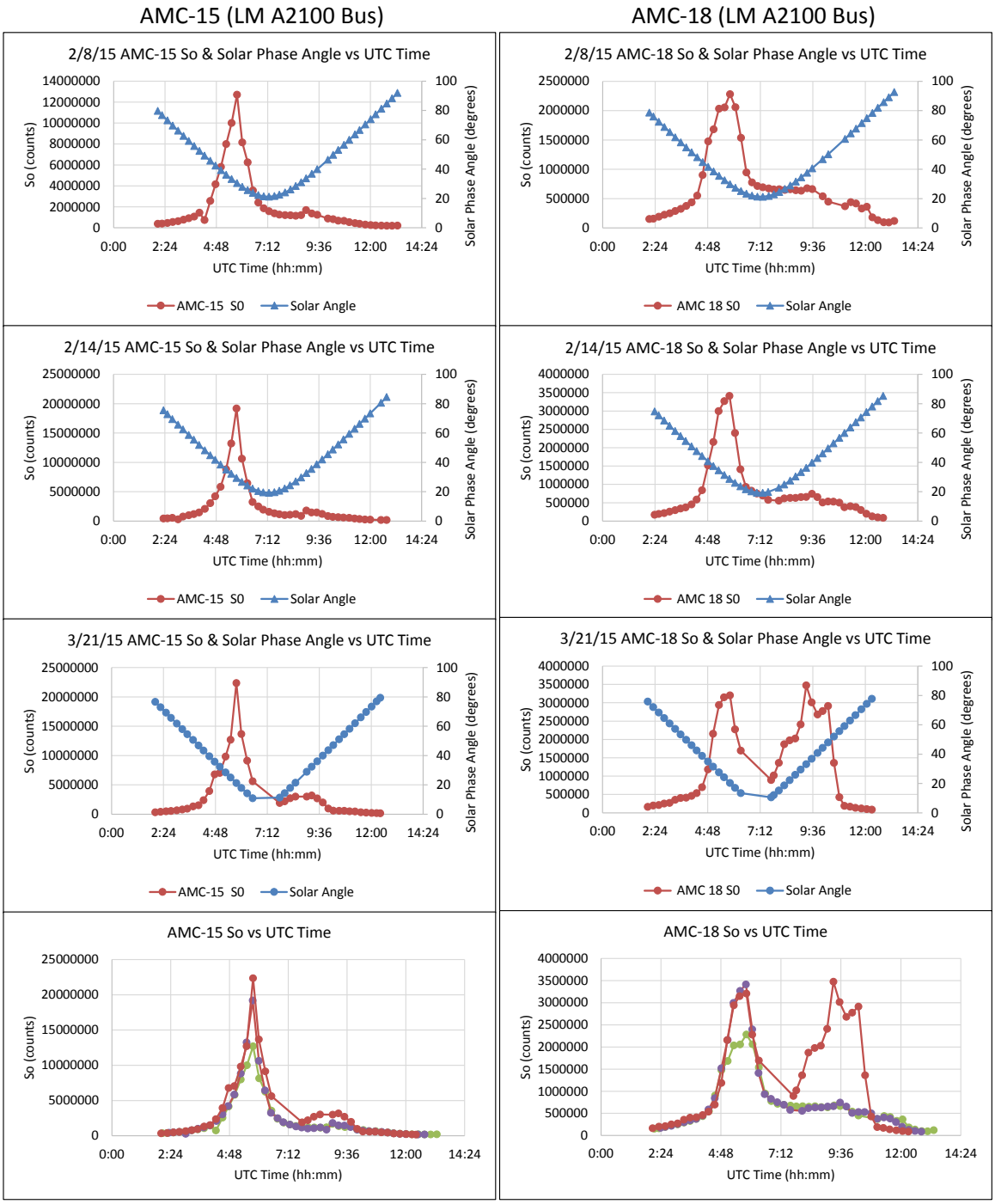

Figure 29. Total intensity, S_0, and solar phase angle for AMC-15 and AMC-18 Collected February 8th, February 14th, and March 21st, 2015

Table 8 below shows the Pearson Correlation Coefficient for S_0 when comparing AMC-15 to itself, AMC-15 to AMC-18, and AMC-18 to itself over the various nights. The green boxes are expected to correlate well since they are the same satellite and the red boxes are expected to have low correlation since they are different satellites. Correlation data for the same satellite on different nights was high as expected with values of 0.89 and 0.90 for AMC-15 and AMC-18 respectively. Correlation of the different satellites is higher with four values higher than 0.86. The boxes noted as "eclipse" mean that the data cannot be compared since there was an eclipse on the third night which led to a different number of data points than for the first two nights. The Pearson Correlation Coefficient did not behave well in that almost all the data was highly correlated.

	AMC-15 LM A2100 2/8/15	AMC-15 LM A21000	AMC-15 LM A2100 3/21/15	AMC-18 LM A2100 2/8/15	AMC-18 LM A21000 2/14/15	AMC-18 LM A2100 3/21/15
AMC-15 LM A2100 2/8/15	X					
LM A21000 2/14/15	0.89	X				
AMC-15 LM A2100 3/21/15	Eclipse	Eclipse	X			
AMC-18 LM A2100 2/8/15	0.96	0.87	Eclipse	X		
AMC-18 LM A21000 2/14/15	0.86	0.95	Eclipse	0.90	X	
AMC-18 LM A2100 3/21/15	Eclipse	Eclipse	0.55	Eclipse	Eclipse	X

Table 8. Pearson Correlation Coefficients for AMC-15 and AMC-18 S_0

Directv-10 and Directv-12 (Boeing 702 Bus) S_0 Data

Figure 30 below compares the intensity plots and solar phase angle of Directv-10 and Directv-12 during the three nights of observations. The last two plots show all three nights of intensity data for each satellite. It is interesting to note that the maximum intensity of the Boeing 702 buses occurred at the smallest solar phase angle as expected. Since both satellites have the same bus design, it would be difficult to differentiate the two due to the similar intensity plots over time. It should also be noted that the maximum values on the three different nights were not consistent on either satellite although the Directv-12 maximum intensity is close on the first two nights.

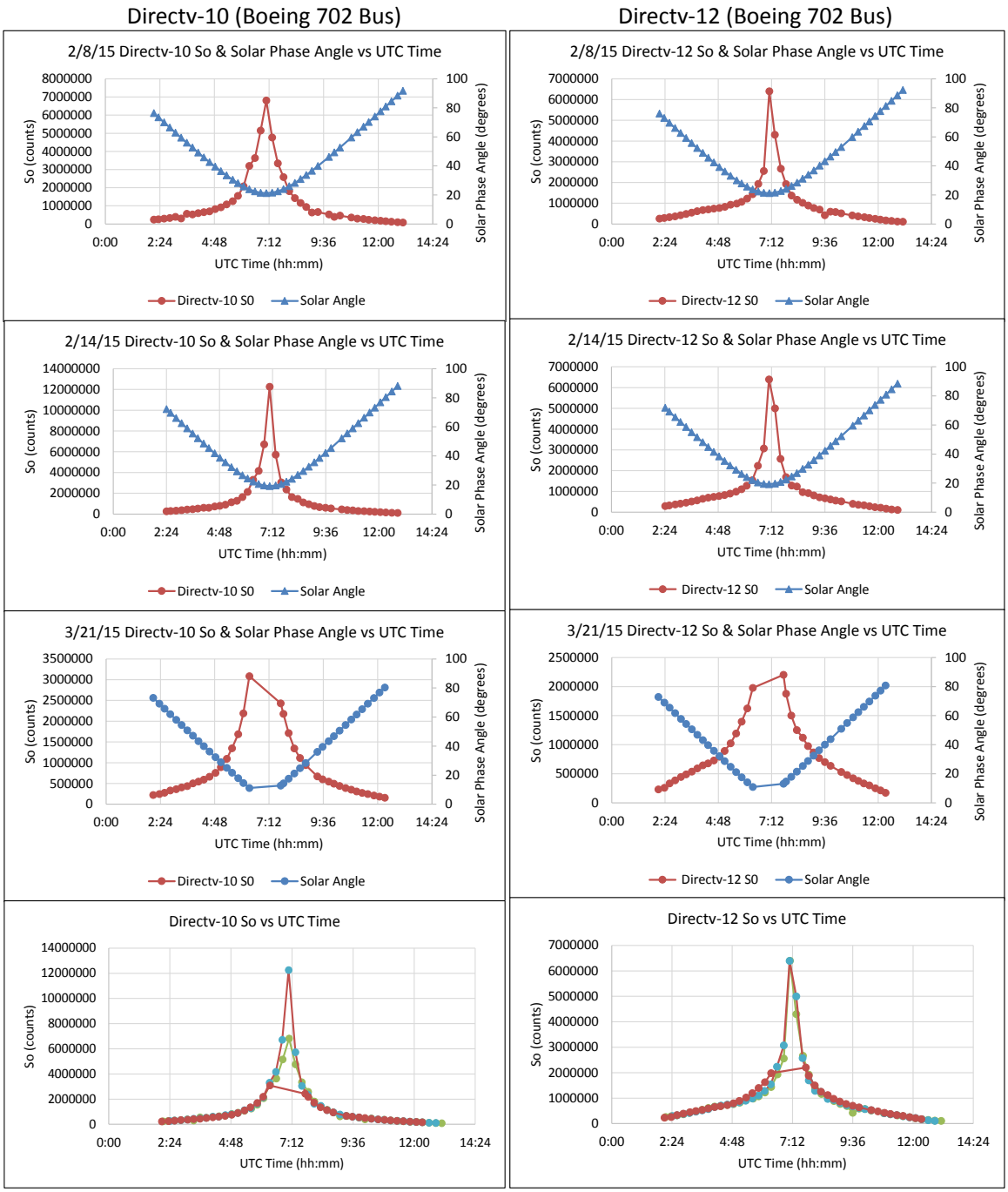

Figure 30. Total intensity, S_0, and solar phase angle for Directv-10 and Directv-12 collected February 8th, February 14th, and March 21st, 2015

Table 9 below shows the Pearson Correlation Coefficient for S_0 when comparing Directv-10 to itself, Directv-10 to Directv-12, and Directv-12 to itself over the various nights. The green boxes are expected to correlate well since they are the same satellite and the red boxes are expected to have low correlation since they are different satellites. Correlation data for the same satellite on different nights was high as expected with values of 0.84 and 0.81 for Directv-10 and Directv-12 respectively. Correlation of the different satellites is higher with four values higher than 0.93. The boxes noted as "eclipse" mean that the data cannot be compared since there was an eclipse on the third night which led to a different number of data points than for the first two nights. The Pearson Correlation Coefficient did not behave well in that almost all the data was highly correlated.

	Directv-10 Boeing 702 2/8/15	Directv-10 Boeing 702 2/14/15	Directv-10 Boeing 702 3/21/15	Directv-12 Boeing 702 2/8/15	Directv-12 Boeing 702 2/14/15	Directv-12 Boeing 702 3/21/15
Directv-10 Boeing 702 2/8/15	X					
Directv-10 Boeing 702 2/14/15	0.84	X				
Directv-10 Boeing 702 3/21/15	Eclipse	Eclipse	X			
Directv-12 Boeing 702 2/8/15	0.94	0.64	Eclipse	X		
Directv-12 Boeing 702 2/14/15	0.93	0.96	Eclipse	0.81	X	
Directv-12 Boeing 702 3/21/15	Eclipse	Eclipse	0.97	Eclipse	Eclipse	X

Table 9. Pearson Correlation Coefficients for Directv-10 and Directv-12 S_0

Directv-4S and SES-1 (Boeing 601 Bus and Star-2 Bus) S_0 Data

Figure 31 below compares the intensity plots and solar phase angle of Directv-4S and SES-1 during the three nights of observations. The last two plots show all three nights of intensity data for each satellite. It is interesting to note that the maximum intensity of the Boeing 601 bus is not consistent. The observations are ill behaved in that the intensities change dramatically and there are significant spurs throughout the night with one large specular signal well past the minimum solar phase angle. This rapid change in intensities could in fact be used as a feature to aid in classification of the Directv-4S and potentially Boeing 601 buses in general if other 601 buses showed the same ill-behaved intensity data. The SES-1 signal by contrast was fairly well behaved in that there was one central spike in the data near the minimum solar phase angle. While these two satellites with different buses certainly have different signatures and could be distinguished from each other, SES-1 has a signature that is similar to the other satellites that have maximum intensities near the minimum solar phase angle such as the Boeing 702 buses.

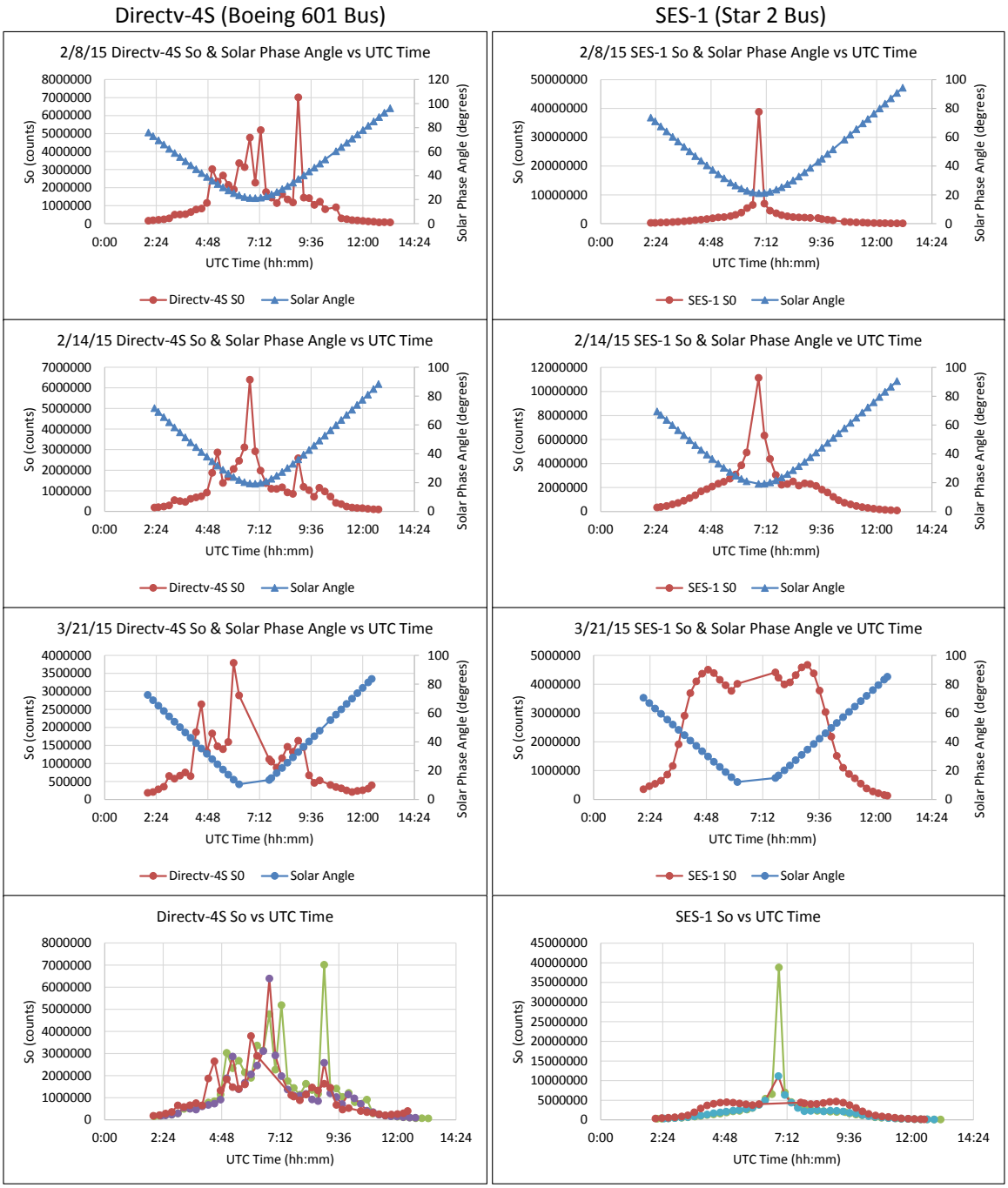

Figure 31. Total intensity, S_0, and solar phase angle for Directv-4S and SES-1 collected February 8th, February 14th, and March 21st, 2015

Table 10 below shows the Pearson Correlation Coefficient for S_0 when comparing Directv-4S to itself, Directv-4S to SES-1, and SES-1 to itself over the various nights. The green boxes are expected to correlate well since they are the same satellite and the red boxes are expected to have low correlation since they are different satellites. Correlation data for the same satellite on different nights was low with values of 0.58 and 0.40 for Directv-4S and SES-1 respectively. Correlation of the different satellites ranged from a low of 0.44 to a high of 0.78. The boxes noted as "eclipse" mean that the data cannot be compared since there was an eclipse on the third night which led to a different number of data points than for the first two nights. The Pearson Correlation Coefficient did not behave well in that almost all the data was moderately correlated.

	Directv-4S Boeing 601	Directv-4S Boeing 601	Directv-4S Boeing 601	SES-1 Star 2 2/8/15	SES-1 Star 2 2/14/15	SES-1 Star 2 3/21/15
Directv-4S Boeing 601 2/8/15	X					
Directv-4S Boeing 601 2/14/15	0.58	X				
Directv-4S Boeing 601 3/21/15	Eclipse	Eclipse	X			
SES-1 Star 2 2/8/15	0.51	0.44	Eclipse	X		
SES-1 Star 2 2/14/15	0.55	0.78	Eclipse	0.40	X	
SES-1 Star 2 3/21/15	Eclipse	Eclipse	0.76	Eclipse	Eclipse	X

Table 10. Pearson Correlation Coefficients for Directv-4S and SES-1 S_0

Another interesting comparison for all the S_0 data was to look at the solar phase angle at which the maximum intensity occurs as it relates to the minimum solar phase angle for that night. A linear relationship between the two was documented with this limited data set of three observations which may change as the data set increases. As the solar season progresses from Vernal equinox on approximately March 21st to Autumnal equinox on approximately September 23rd due to the Earth's 23.5 degree tilt, the minimum solar phase angle will vary over time. The data was analyzed to see if there was a seasonal correlation that could be exploited to distinguish different satellites. The hope is that since the different types of satellite buses seem to have maximum intensities that occur with consistent relationships to the minimum solar phase angle for that evening this could be exploited as a classification feature. For example, since the minimum solar phase angle can be predicted for a given satellite on a given day based on orbital geometry, the solar phase angle where the maximum intensity occurs can also be predicted if the linear relationship proposed in this dissertation holds over the solar season. Once S_0 data has been collected to determine the solar phase angle where the maximum intensity occurs, if it differs from the prediction then the satellite being studied may be incorrectly identified by the Space Surveillance Network (SSN).

There was a relatively consistent feature of the data for the Directv-8 and Directv-9S satellites in that there appeared to be a linear relationship between solar phase angle where the maximum intensity occurred and the minimum solar phase angle due to seasonal solar angle variations. Figure 32 below shows that when the solar phase angle for maximum intensity recorded on a particular evening is plotted against the minimum

solar phase angle for that particular evening, the plot is linear for both Directv-8 and Directv-9S. There appears to be potentially enough separation in the signatures to distinguish the two satellites from each other.

As with the Directv-8 and Directv-9S satellites, there was a relatively consistent feature of the data for both the AMC-15 and AMC-18 satellites in that there was a linear relationship between solar phase angle where the maximum intensity occurred and the minimum solar phase angle due to season solar angle variations. Figure 32 below shows that when the solar phase angle for maximum intensity recorded on a particular evening is plotted against the minimum solar phase angle for that particular evening the plot is linear for both AMC-15 and AMC-18. There is less separation of this parameter for these satellites than for Directv-8 and Directv-9S which means this would be a harder feature to use to differentiate the two satellites.

Unfortunately due to the eclipse in the third data set for Directv-10 and Directv-12, it will not be possible to include this data in Figure 32 and Figure 33 below which shows the plot of Directv-10 and Directv-12 minimum solar phase angle vs maximum intensity solar phase angle. With only two data points per satellite, the Directv-10 and Directv-12 satellites were consistent in these plots with respect to the slope of the line. There is no separation of this parameter for these satellites which means it would be impossible to use this feature to differentiate the two satellites with the data collected so far. The fact that these two signatures are so consistent may allow this data to be used to identify what type of bus this is and thus contribute to the classification problem of identifying unique satellites.

Unfortunately due to the eclipse in the third data set for Directv-4S and SES-1, it will not be possible to include this data in Figure 32 and Figure 33 below which shows the plot of Directv-4S and SES-1 minimum solar phase angle vs maximum intensity solar phase angle. The Directv-4S data for this analysis is most likely not valid due to the erratic nature of the maximum intensity. The SES-1 data, however, appears to be a valid characterization of the maximum intensity solar phase angle compared to the minimum solar phase angle.

Figure 32 below shows the minimum solar phase angle vs the maximum intensity solar phase angle for the entire set of eight satellites. For the limited set of data in this study, this relationship was linear and had similar slopes which may allow the extrapolation of future data to determine what type of bus a particular intensity signature represented. Directv-12, Directv-10, and SES-1 in Figure 32 are difficult to separate due to the similarity of the data. Figure 33 below shows a zoomed in plot of those satellites along with Directv-4S.

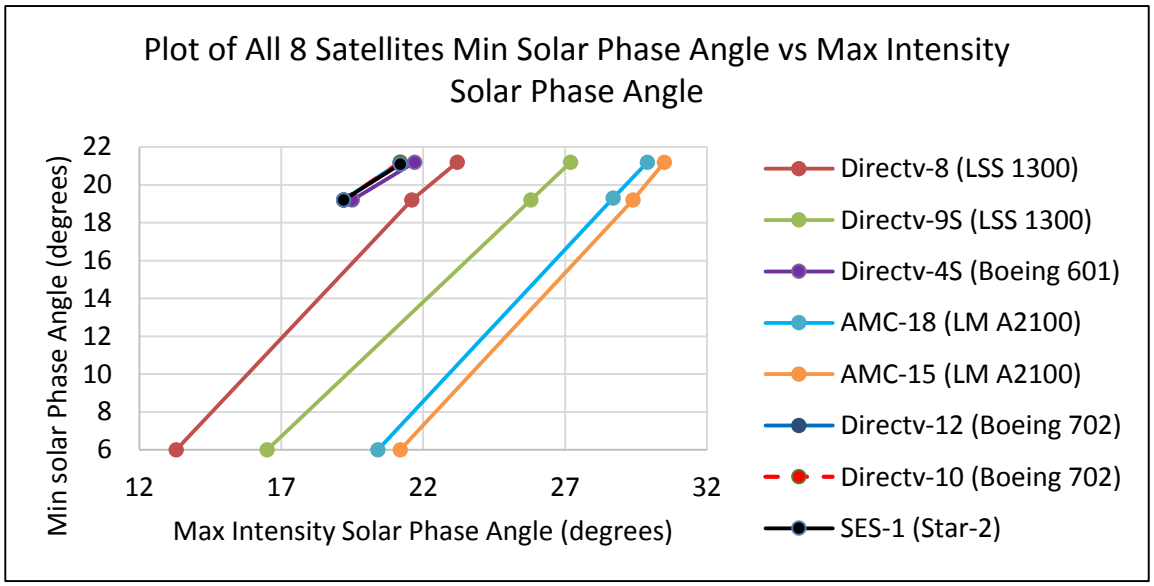

Figure 32. Plot of minimum solar phase angle vs maximum intensity solar phase angle collected February 8th, February 14th, and March 21st, 2015 for all Eight Satellites

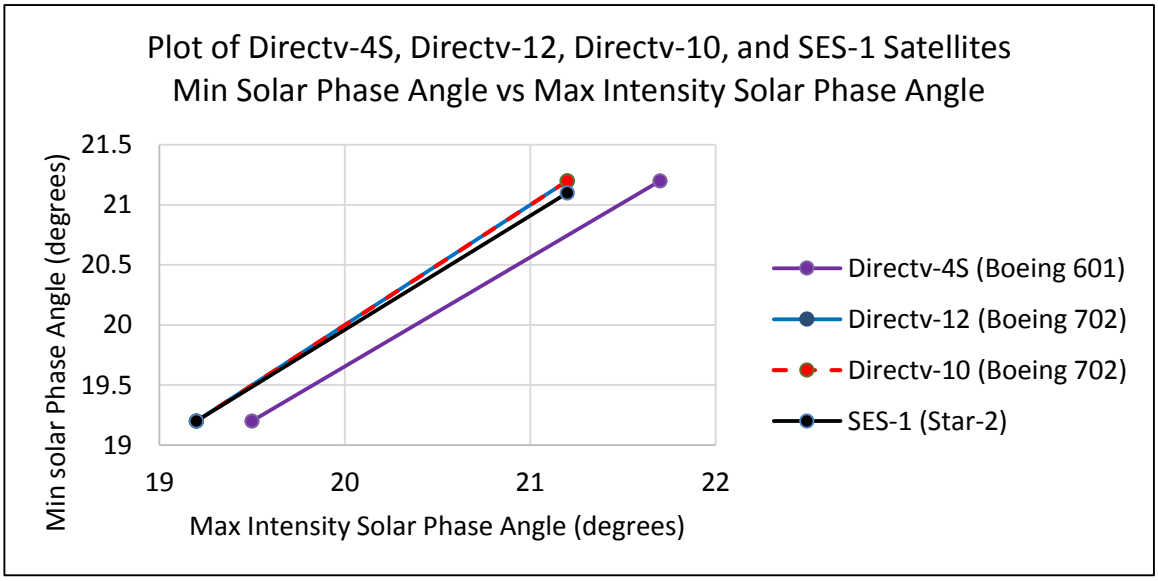

Figure 33. Plot of minimum solar phase angle vs maximum intensity solar phase angle collected February 8th and February 14th, 2015 for Directv-4S, Directv-12, Directv-10, and SES-1

While intensity data from the satellites in this study showed some features that could help in classification such as the general shape of the data and when the maximum intensity occurs relative to the minimum solar phase angle for that night, overall the data did not show enough diversity to completely classify the satellites. Most of the data may allow the type of bus to be identified, but would not enable identification of the exact satellite. Since many of the satellites in orbit are from the same relatively small set of manufacturers, intensity data alone does not meet the needs of the satellite surveillance community for classification of satellites. This data may, however, be used to show a change in operational status of a spacecraft due to a change in the control of the satellite bus or solar arrays. Typically, when a satellite goes into a “safe mode” due to a low state

of battery charge or control anomaly, the spacecraft is no longer three-axis stabilized but goes into a sun pointing mode. This means the solar arrays still track the sun by moving the entire bus with the solar arrays in some known "home" position so the spacecraft is in a power and thermal safe configuration. Thus different faces of the bus are pointed at the Earth which will most likely yield a different optical intensity to an observer.

Comparison of S_1 Linear Polarization Data

Since polarization properties can change as materials age in the space environment, it should be possible to detect a different linear polarization for the same satellite bus launched at different times. The data indicates that there is a significantly different linear polarization signature for the same bus launched several years apart. This difference could be due to material aging in the space environment or to a slightly different configuration of the payloads or solar arrays.

In several of the data sets it can be seen that the values of S_1 are slightly outside of the range of expected values of -1.0 to 1.0. Values as low as -1.1 are evident in the data. The fact that a few of the normalized plots of the S_1 parameters show values of -1.0 or slightly lower may be due to the fact that the Mueller matrix used for calibration is not perfect and may need to be slightly modified. This could be caused by the fact that the polaroid used in the calibration of the polarimetry channels is not a perfect polarizer in that it will let a small amount of the wrong polarization through. A more likely cause is that the small number of cases where the normalized S_1 is less than -1.0 occurs at the end of the evening when the signal-to-noise is low with values of approximately 20 for both cameras. A five percent deviation is well within reason for use of the data to show the

feasibility of using polarization to classify satellites. Figures 10 and 11 indicate that the beamsplitter performance of P-polarization separation is approximately 10% lower than the S-polarization. However, when the flat panel calibration data was fed back into the calibration algorithm as if it was satellite data, a result was produced that faithfully represented the correct polaroid angle within +/- five percent or a value of +/- 0.05 as it is related to the normalized S_1 Stokes parameter. See Figure 22 for the plot that shows a slight deviation from the desired values of -1.0 to 1.0 for S_1.

Directv-8 and Directv-9S (LSS 1300 Bus) S_1 Data

Figure 34 below shows normalized linear polarization data for Directv-8 and Directv-9S as collected on February 8th, February 14th, and March 21st, 2015. The last two plots show all three nights of linear polarization data for each satellite. It can easily be seen from the data that the S_1 Stokes parameter polarization data is repeatable from night to night and is distinctly different for the same satellite buses made by the same satellite manufacturer launched 1.5 years apart. Directv-8 showed the only positive S_1 values out of all the satellites which means the polarization went from vertical (P-polarization) to horizontal (S-polarization) and back to vertical. This distinctive feature was seen on all three nights at approximately the same time and solar phase angle for two nights and at a slight offset in time for the last night. In some of the data sets there are a few single outliers that may or may not be significant in classification of the satellites.

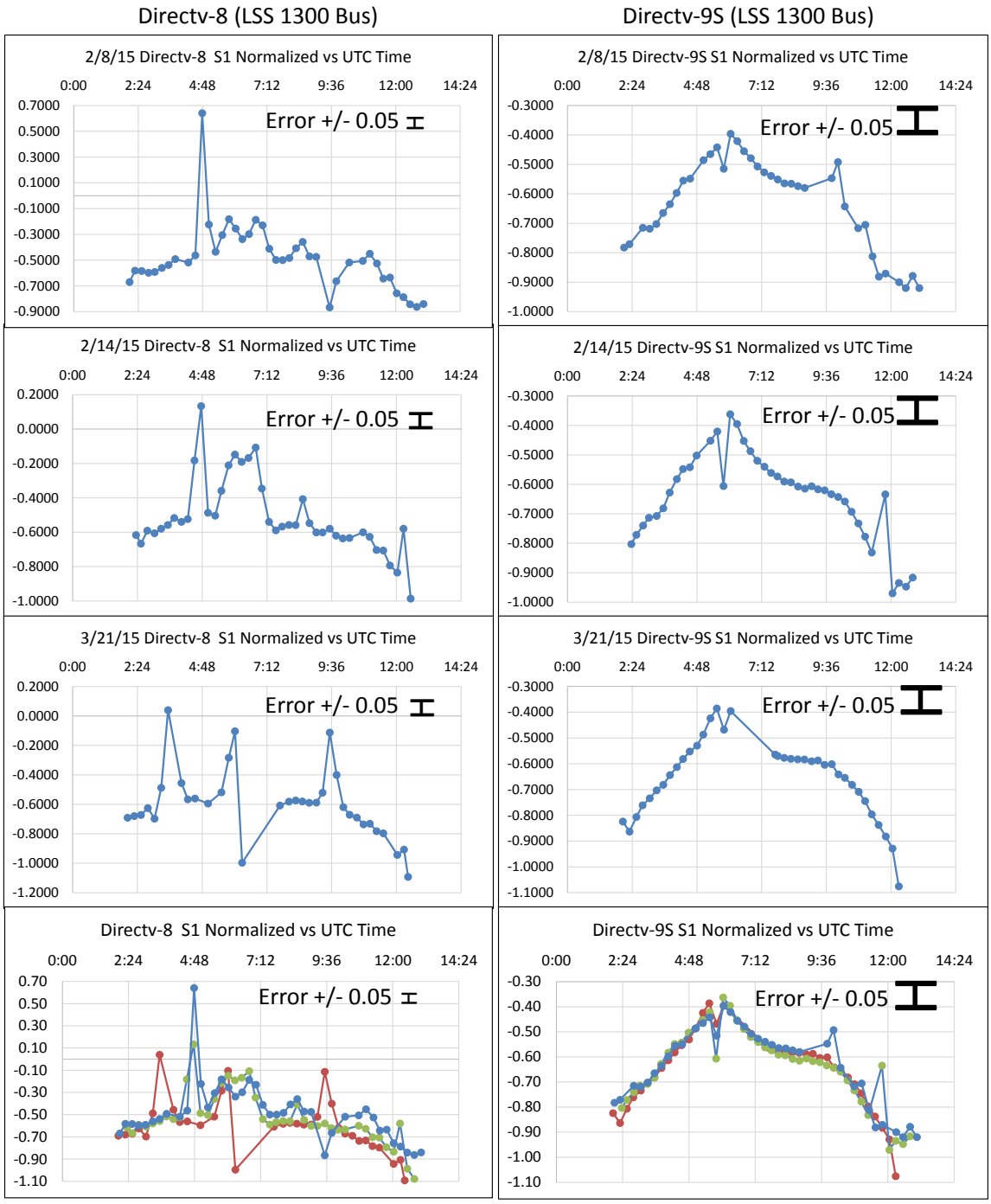

Figure 34. Normalized linear polarization, S_1, of Directv-8 and Directv-9S collected February 8th, February 14th, and March 21st, 2015

Table 11 below shows the Pearson Correlation Coefficient for S_1 when comparing Directv-8 to itself, Directv-8 to Directv-9S, and Directv-9S to itself over the various nights. The green boxes are expected to correlate well since they are the same satellite and the red boxes are expected to have low correlation since they are different satellites. Correlation data for the same satellite on different nights worked as expected with values of 0.83 or higher. Correlation of the different satellites is lower as expected at 0.74 or less. The boxes noted as "eclipse" mean that the data cannot be compared since there was an eclipse on the third night which led to a different number of data points than for the first two nights.

	Directv-8 LSS 1300 2/8/15	Directv-8 LSS 1300 2/14/15	Directv-8 LSS 1300 3/21/15	Directv-9S LSS 1300 2/8/15	Directv-9S LSS 1300 2/14/15	Directv-9S LSS 1300 3/21/15
Directv-8 LSS 1300 2/8/15	X					
Directv-8 LSS 1300 2/14/15	0.83	X				
Directv-8 LSS 1300 3/21/15	Eclipse	Eclipse	X			
Directv-9S LSS 1300 2/8/15	0.60	0.70	Eclipse	X		
Directv-9S LSS 1300 2/14/15	0.68	0.74	Eclipse	0.88	X	
Directv-9S LSS 1300 3/21/15	Eclipse	Eclipse	0.35	Eclipse	Eclipse	X

Table 11. Pearson Correlation Coefficients for Directv-8 and Directv-9S S_1

AMC-15 and AMC-18 (LM A2100 Bus) S_1 Data

Figure 35 below shows the normalized S_1 Stokes parameters for AMC-15 and AMC-18 from data collected on February 8th, February 14th, and March 21st, 2015. The

last two plots show all three nights of linear polarization data for each satellite. As with the previous satellites discussed, S_1 data repeats fairly well for all collections and the two identical buses show similar but distinctively different features of their polarization signatures. One of these differentiators includes a consistent polarization value for the higher points of the "M" shaped feature centered at a time of approximately 5:30. These two buses would probably be the hardest to differentiate of all the eight satellites.

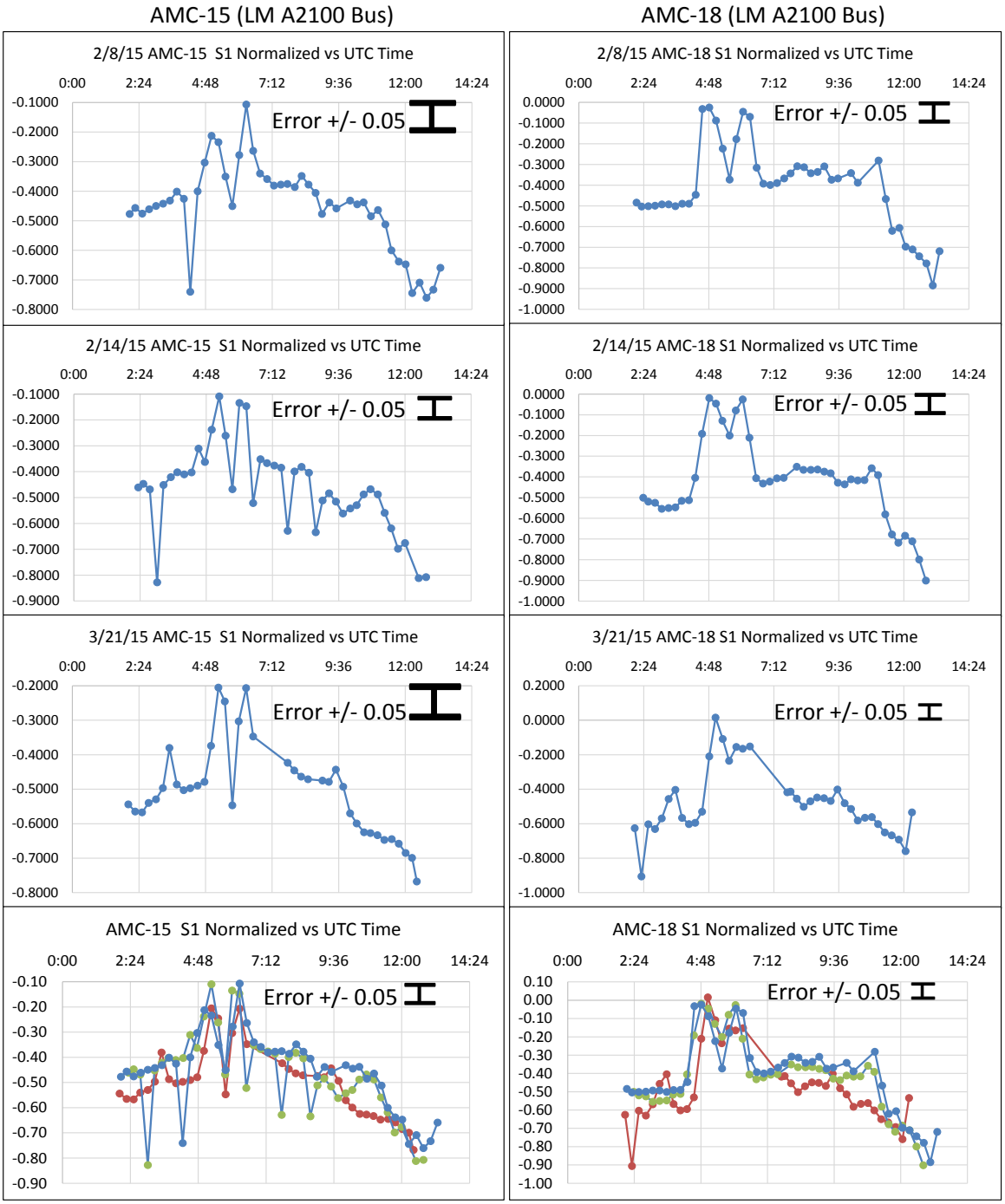

Figure 35. Normalized linear polarization, S_1, of AMC-15 and AMC-18 collected February 8th, February 14th, and March 21st, 2015

Table 12 below shows the Pearson Correlation Coefficient for S_1 when comparing AMC-15 to itself, AMC-15 to AMC-18, and AMC-18 to itself over the various nights.

The green boxes are expected to correlate well since they are the same satellite and the red boxes are expected to have low correlation since they are different satellites. Correlation data for the same satellite on different nights worked as expected for AMC-18 with a value of 0.88 but was lower than expected for AMC-15 with a value of 0.57. Correlation of the different satellites is slightly lower as expected at 0.79 or less.

	AMC-15 LM A2100 2/8/15	AMC-15 LM A21000 2/14/15	AMC-15 LM A2100 3/21/15	AMC-18 LM A2100 2/8/15	AMC-18 LM A21000	AMC-18 LM A2100 3/21/15
AMC-15 LM A2100 2/8/15	X					
AMC-15 LM A21000 2/14/15	0.57	X				
AMC-15 LM A2100 3/21/15	Eclipse	Eclipse	X			
AMC-18 LM A2100 2/8/15	0.79	0.71	Eclipse	X		
AMC-18 LM A21000 2/14/15	0.59	0.75	Eclipse	0.88	X	
AMC-18 LM A2100 3/21/15	Eclipse	Eclipse	0.73	Eclipse	Eclipse	X

Table 12. Pearson Correlation Coefficients for AMC-15 and AMC-18 S_1

Directv-10 and Directv12 (Boeing 702 Bus) S_1 Data

Figure 36 below shows the normalized S1 Stokes parameters for Directv-10 and Directv-12 as collected with the two-channel polarimeter on February 8th, February 14th, and March 21st, 2015. The last two plots show all three nights of linear polarization data for each satellite. Although the buses are the same for each satellite but with launch dates two years apart, there is a distinct difference in the polarization signature at the apex.

Another important aspect to note is how repeatable the signatures are for the same satellite with respect to the curve shape and max/min values. Directv-10 has a curved shape at its maximum and Directv-12 has an inverted “V” shape at it maximum. With the loss of data at these minimum values due to the 72 minute eclipse for the March 21st data set, it would be more difficult to classify with this data alone.

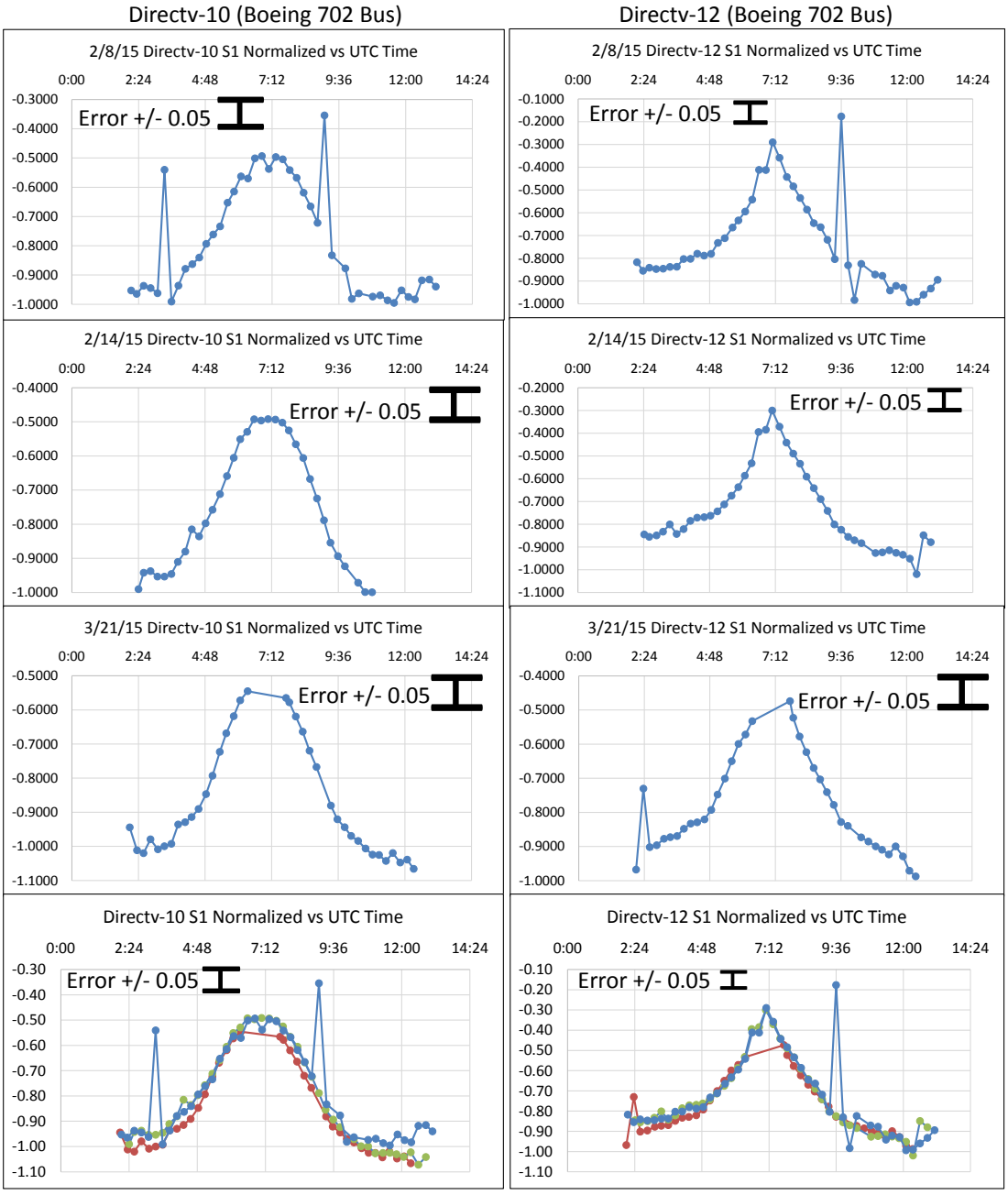

Figure 36. Normalized linear polarization, S_1, of Directv-10 and Directv-12 collected February 8th, February 14th, and March 21st, 2015

Table 13 below shows the Pearson Correlation Coefficient for S_1 when comparing Directv-10 to itself, Directv-10 to Directv-12, and Directv-12 to itself over the various nights. The green boxes are expected to correlate well since they are the same satellite

and the red boxes are expected to have low correlation since they are different satellites. Correlation data for the same satellite on different nights worked as expected with values of 0.81 or higher. Correlation of the different satellites was higher than expected with values as high as 0.96. This is due to the fact that the only real difference in the data occurs over as small part of the data at maximum values with the smooth curve and the inverted "V".

	Directv-10 Boeing 702 2/8/15	Directv-10 Boeing 702 2/14/15	Directv-10 Boeing 702 3/21/15	Directv-12 Boeing 702 2/8/15	Directv-12 Boeing 702 2/14/15	Directv-12 Boeing 702 3/21/15
Directv-10 Boeing 702 2/8/15	X					
Directv-10 Boeing 702 2/14/15	0.84	X				
Directv-10 Boeing 702 3/21/15	Eclipse	Eclipse	X			
Directv-12 Boeing 702 2/8/15	0.73	0.80	Eclipse	X		
Directv-12 Boeing 702 2/14/15	0.82	0.96	Eclipse	0.81	X	
Directv-12 Boeing 702 3/21/15	Eclipse	Eclipse	0.95	Eclipse	Eclipse	X

Table 13. Pearson Correlation Coefficients for Directv-10 and Directv-12 S_1

Directv-4S and SES-1 (Boeing 601 Bus and Star-2 Bus) S_1 Data

Figure 37 below shows normalized linear polarization data for Directv-4S and SES-1 as collected on February 8th, February 14th, and March 21st, 2015. The last two plots show all three nights of linear polarization data for each satellite. These two different buses built by different manufacturers have generally good repeatability in their data taken six nights apart and also diverse features from the other satellite S_1 data. Data

taken on March 21st 2015 of SES-1, however, shows a low visual correlation to data taken on the two previous nights. One particular feature to highlight is how the third data set rises in the final hour compared to the other two sets that drop dramatically in the last hour. The author could not find any data to suggest that the satellite was improperly identified by the Space Surveillance Network or that the satellite had a change in its operational status. It is therefore thought that the data is good and that more data collections may reveal a polarization signature that changes more dramatically with time. With enough characterization data sets collected in order to train a classifier, this should not be a problem.

Table 14 below shows the Pearson Correlation Coefficient for S_1 when comparing Directv-4S to itself, Directv-4S to SES-1, and SES-1 to itself over the various nights. The green boxes are expected to correlate well since they are the same satellite and the red boxes are expected to have low correlation since they are different satellites. Correlation data for the same satellite on different nights worked reasonably well with values of 0.70 or higher which is lower than the other "same satellite" correlations. Correlation of the different satellites is lower as expected at 0.75 or less.

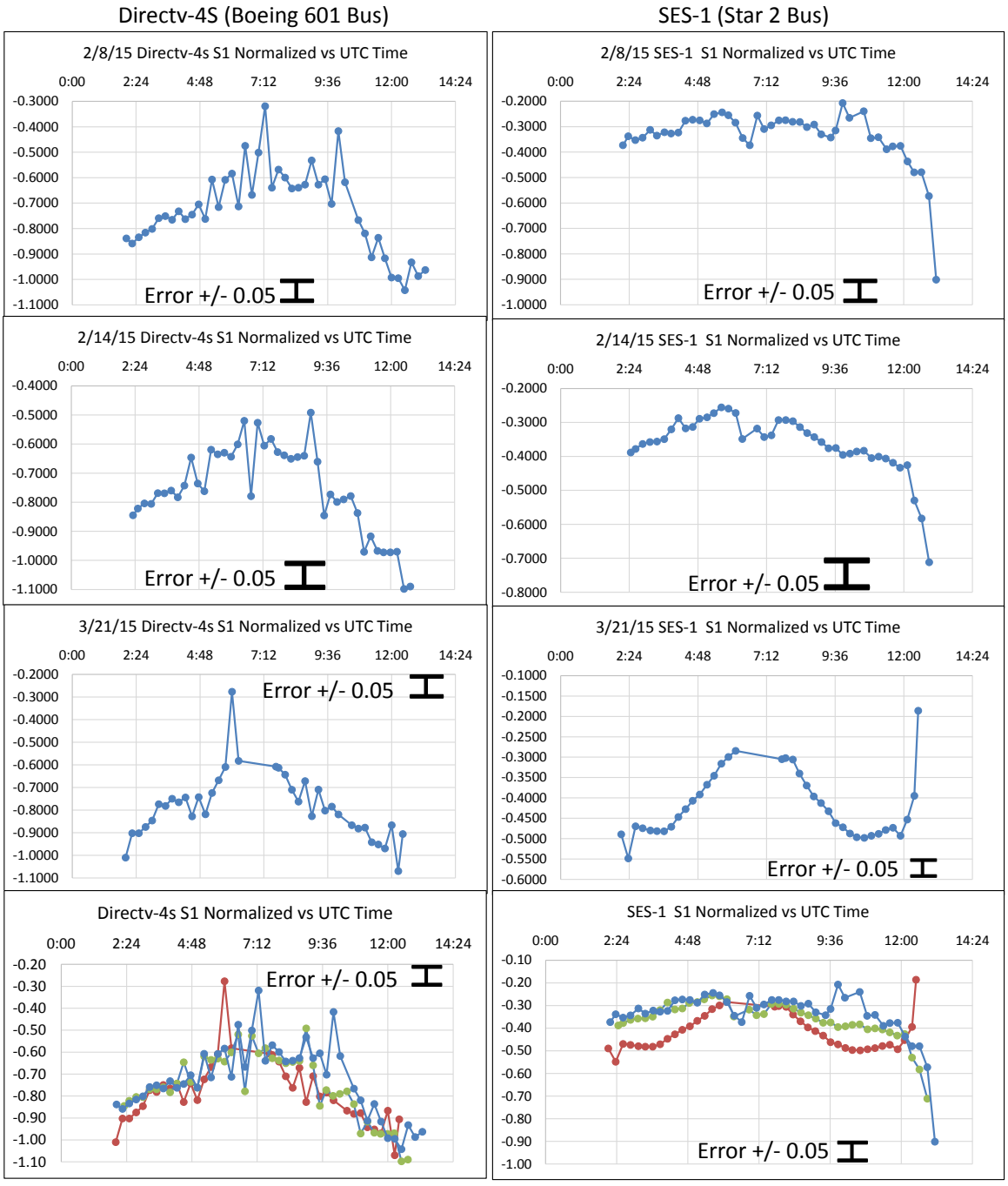

Figure 37. Normalized linear polarization, S1, of Directv-4S and SES-1 collected February 8th, February 14th, and March 21st, 2015

	Directv-4S Boeing 601 2/8/15	Directv-4S Boeing 601 2/14/15	Directv-4S Boeing 601 3/21/15	SES-1 Star 2 2/8/15	SES-1 Star 2 2/14/15	SES-1 Star 2 3/21/15
Directv-4S Boeing 601 2/8/15	X					
Directv-4S Boeing 601 2/14/15	0.70	X				
Directv-4S Boeing 601 3/21/15	Eclipse	Eclipse	X			
SES-1 Star 2 2/8/15	0.65	0.71	Eclipse	X		
SES-1 Star 2 2/14/15	0.59	0.75	Eclipse	0.77	X	
SES-1 Star 2 3/21/15	Eclipse	Eclipse	0.57	Eclipse	Eclipse	X

Table 14. Pearson Correlation Coefficients for Directv-4S and SES-1 S_1

A complete summary of all the calibrated data collected on all eight satellites for the three different nights (February 8th, February 14th, and March 21st, 2015) is shown in Figure 38 below. Each plot is a compilation of the data for a particular satellite. Several of the data sets show a tight grouping of the data but others require finer features to distinguish from the other satellites. While it will take many more data collections to fully characterize the optical signatures and develop a classifier, the data is encouraging that Stokes parameters for total intensity, S_0, and linear polarization, S_1, will provide the distinguishing features necessary. Especially encouraging is the fact that the polarization signatures for the same bus built by the same provider but launched several years apart are relatively easy to distinguish using polarization.

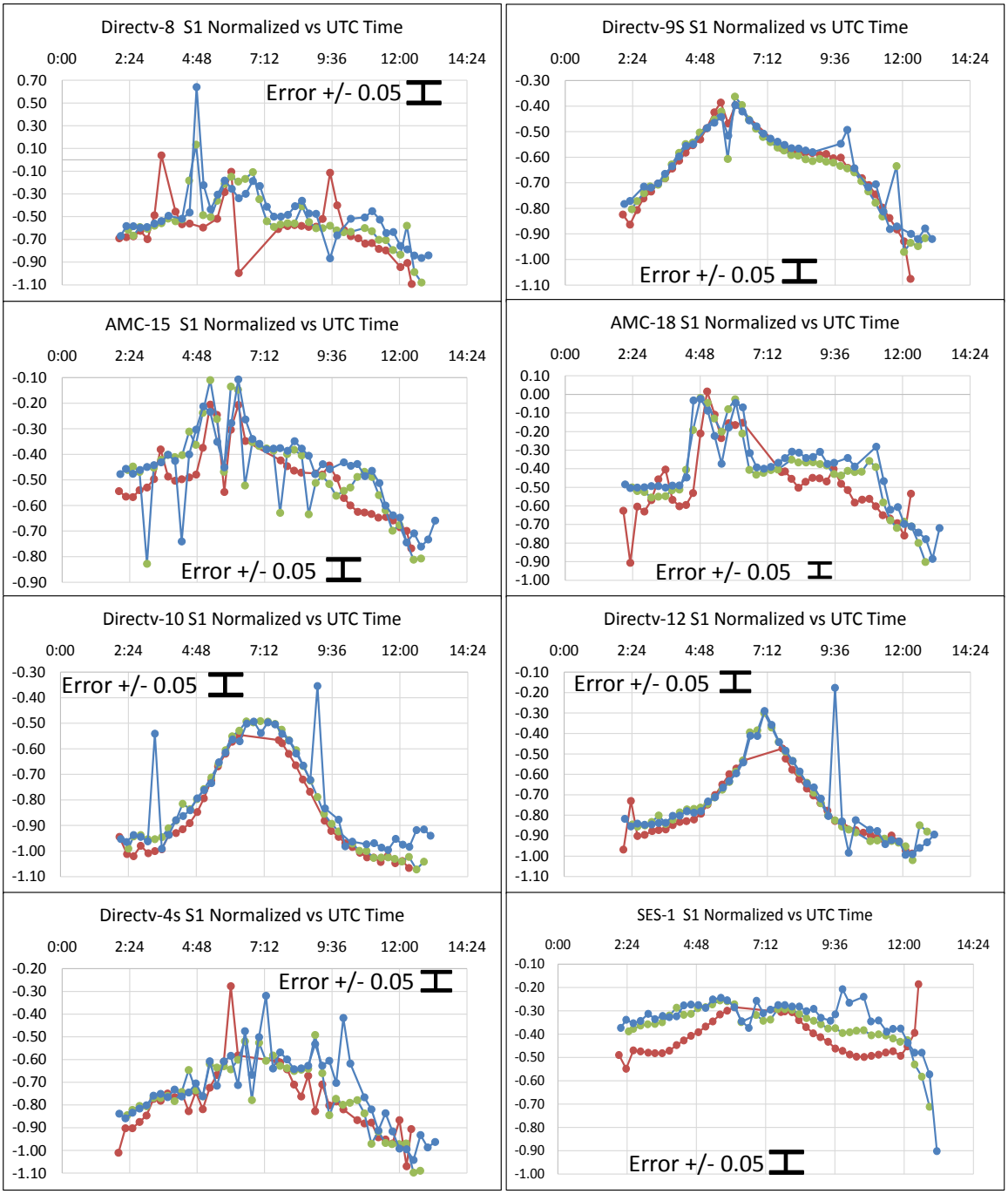

Figure 38. A summary of normalized linear polarization, S_1, for all eight satellites collected February 8th, February 14th, and March 21st, 2015

One interesting finding to note is that when the index of refraction of a vacuum (1.0) and solar cell cover glass (1.5) is fed into Brewster's equation shown above in equation (2), the light reflected off the solar array cells is expected to be fully polarized when reflected at Brewster's angle which is 56 degrees. The solar phase angle of 56 degrees occurred at approximately 3:15 and 10:30 for all the satellites and there was not any significant increase in the polarization signature in any of the data as shown in Figure 43 above. One possible explanation is that the solar array cells have an antireflective coating which reduced the total reflected light. Also, the solar cells are highly specular which means there is very little light reflected in a diffuse manner as required to be seen at 56 degrees off normal.

Generally speaking when viewing the data in Figure 38 above, it can be seen that the S_1 Stokes parameter for linear polarization started out lower corresponding to stronger vertical polarization. The linear polarization then tended to increase which means it went from vertical polarization towards more equal parts vertical and horizontal polarization near the middle of the night. Next, the signatures trended towards lower S_1 values signifying more vertical polarization. This means that while the solar arrays were edge-on to the observer and thus not a significant contributor to the overall optical signature, the bus components were higher values of S_1 and thus higher in vertical polarization referenced to the telescope due to greater incident reflection angles from surface normals. This signature could be part of the bus thermal control surfaces or the payload antennas.

Another interesting way to analyze the data is to plot the arithmetic mean of the normalized linear polarization parameter S_1. To find the arithmetic mean, add all S_1

values added together for a particular satellite on a particular night and then divide by the number of values for that evening. Figure 39 below shows all the calculated arithmetic mean S_1 values for each night. The data for these eight satellites is somewhat consistent from night to night and also separates well from satellite to satellite. Data for a particular type of satellite bus is also relatively close in value. This data could potentially help in a classifier.

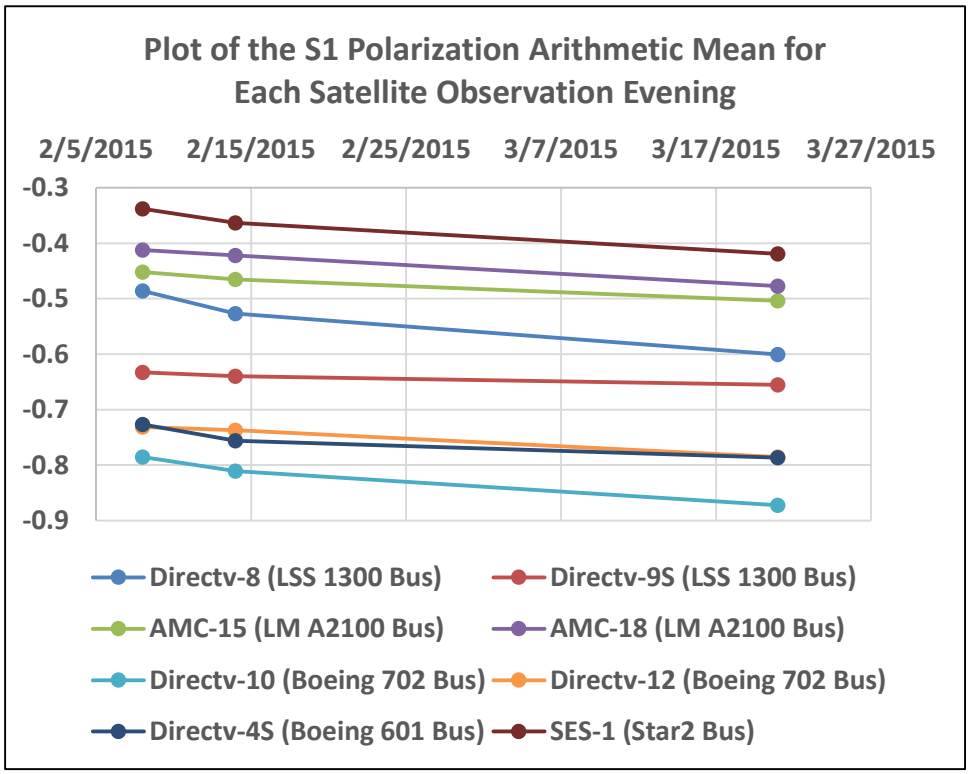

Figure 39. A summary of arithmetic means for normalized S_1, for all eight satellites collected February 8th, February 14th, and March 21st, 2015

Another interesting way to analyze the data is to plot the standard deviation of the normalized linear polarization parameter S_1. The standard deviation, s, is a measure of how measurements are dispersed from the arithmetic mean. It is calculated using equation (26) below (McClave and Dietrich 1985):

$$s = \sqrt{\frac{\sum(x - \bar{x})^2}{n - 1}} \tag{26}$$

where x is a value of normalized linear polarization S_1, $\bar{x}$ is the data set arithmetic mean, and n is the number of data points in the data set. Figure 40 below shows all the calculated standard deviation values for S_1 each night for each satellite. The data for these eight satellites is somewhat consistent from night to night for a particular satellite but does not separate well from satellite to satellite. Data for a particular type of satellite bus was not very close in value. This data would be more difficult to use in a classifier.

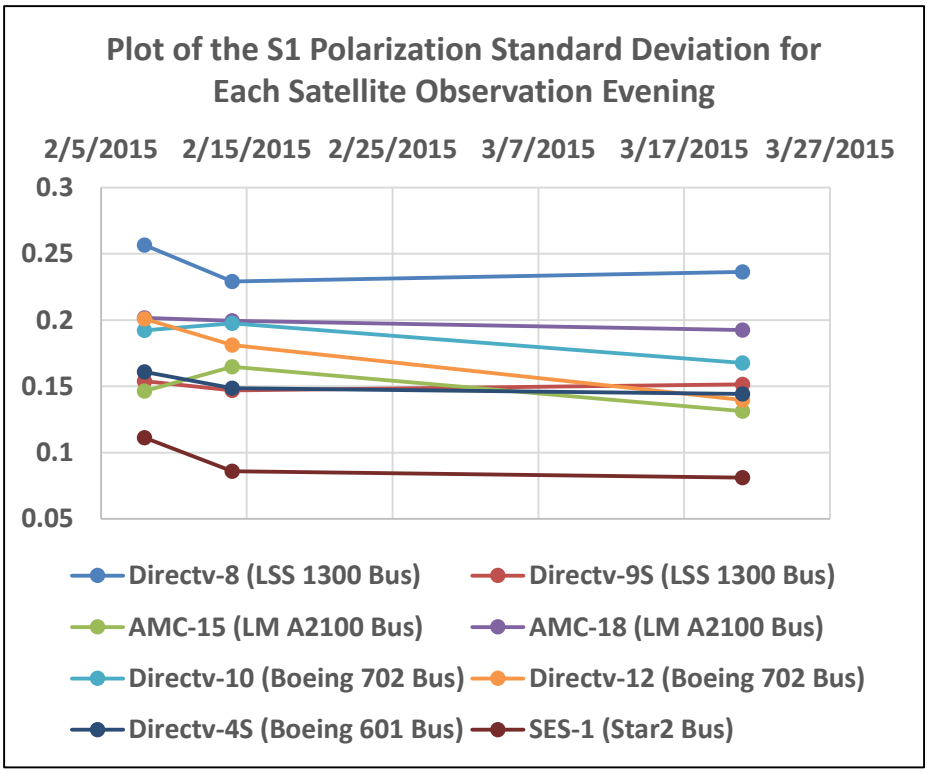

Figure 40. A summary of standard deviations for normalized S_1, for all eight satellites collected February 8th, February 14th, and March 21st, 2015

Correlation of S_0 Intensity Data and S_1 Linear Polarization Data

In order to compare the correlation of S_0 intensity data and normalized S_1 linear polarization data, the Pearson Correlation Coefficient was calculated for the same satellite on all the data for each night. Table 15 below shows that there was generally a weak to strong positive correlation between the S_0 and S_1 with values ranging from 0.2 to 0.96. What this really means though is that since the S_1 data was almost all negative values meaning vertical or P-polarization, as the values went more negative towards -1, the Degree of Polarization was actually higher. This implies that S_0 and S_1 actually have a negative correlation since as the intensity goes higher, the polarization gets stronger. There are many cases where when the intensity spiked higher, the linear polarization spiked higher (more negative towards total vertical polarization). This correlation of total intensity and linear polarization can be predicted due to the fact that, generally, there is a stronger polarization signal in the more specular reflection directions as opposed to the diffuse reflections (Schott 2009).

Directv-8 LSS 1300 2/8/15	Directv-8 LSS 1300 2/14/15	Directv-8 LSS 1300 3/21/15	Directv-9S LSS 1300 2/8/15	Directv-9S LSS 1300 2/14/15	Directv-9S LSS 1300 3/21/15
0.51	0.64	0.53	0.53	0.39	0.63
AMC-15 LM A2100 2/8/15	AMC-15 LM A21000 2/14/15	AMC-15 LM A2100 3/21/15	AMC-18 LM A2100 2/8/15	AMC-18 LM A21000 2/14/15	AMC-18 LM A2100 3/21/15
0.53	0.51	0.57	0.74	0.77	0.61
Directv-10 Boeing 702 2/8/15	Directv-10 Boeing 702 2/14/15	Directv-10 Boeing 702 3/21/15	Directv-12 Boeing 702 2/8/15	Directv-12 Boeing 702 2/14/15	Directv-12 Boeing 702 3/21/15
0.72	0.70	0.95	0.73	0.85	0.96
Directv-4S Boeing 601 2/8/15	Directv-4S Boeing 601 2/14/15	Directv-4S Boeing 601 3/21/15	SES-1 Star 2 2/8/15	SES-1 Star 2 2/14/15	SES-1 Star 2 3/21/15
0.67	0.55	0.76	0.20	0.44	0.50

Table 15. A summary of Pearson Correlation Coefficients comparing S_0 and normalized S_1, for all eight satellites collected February 8th, February 14th, and March 21st, 2015

Another way to look at how the Stokes S_0 and S_1 are related is to plot these parameters as a function of the UTC time since that will allow a visual correlation of various components of the satellite signatures to compare to the calculated correlation above. The plots are structured with S_0 in counts on the left vertical axis and S_1 values normalized to S_0 on the right vertical axis. Figure 41 below shows the intensity and linear polarization values for Directv-8 and Directv-9S as a function of UTC time. It is interesting to note that almost every significant spike in either intensity or polarization values corresponds to at least a small spike up or down in the other parameter. Keep in mind that as the Stokes linear polarization parameter S_1 decreases on these plots, the signal is more vertically or P-polarized. Directv-9S shows a repeatable case where the strongest intensity corresponds to a sharp increase towards linear polarization. It should

be noted however, that in general especially for Directv-9S, as the intensity decreased, the linear polarization was also reduced.

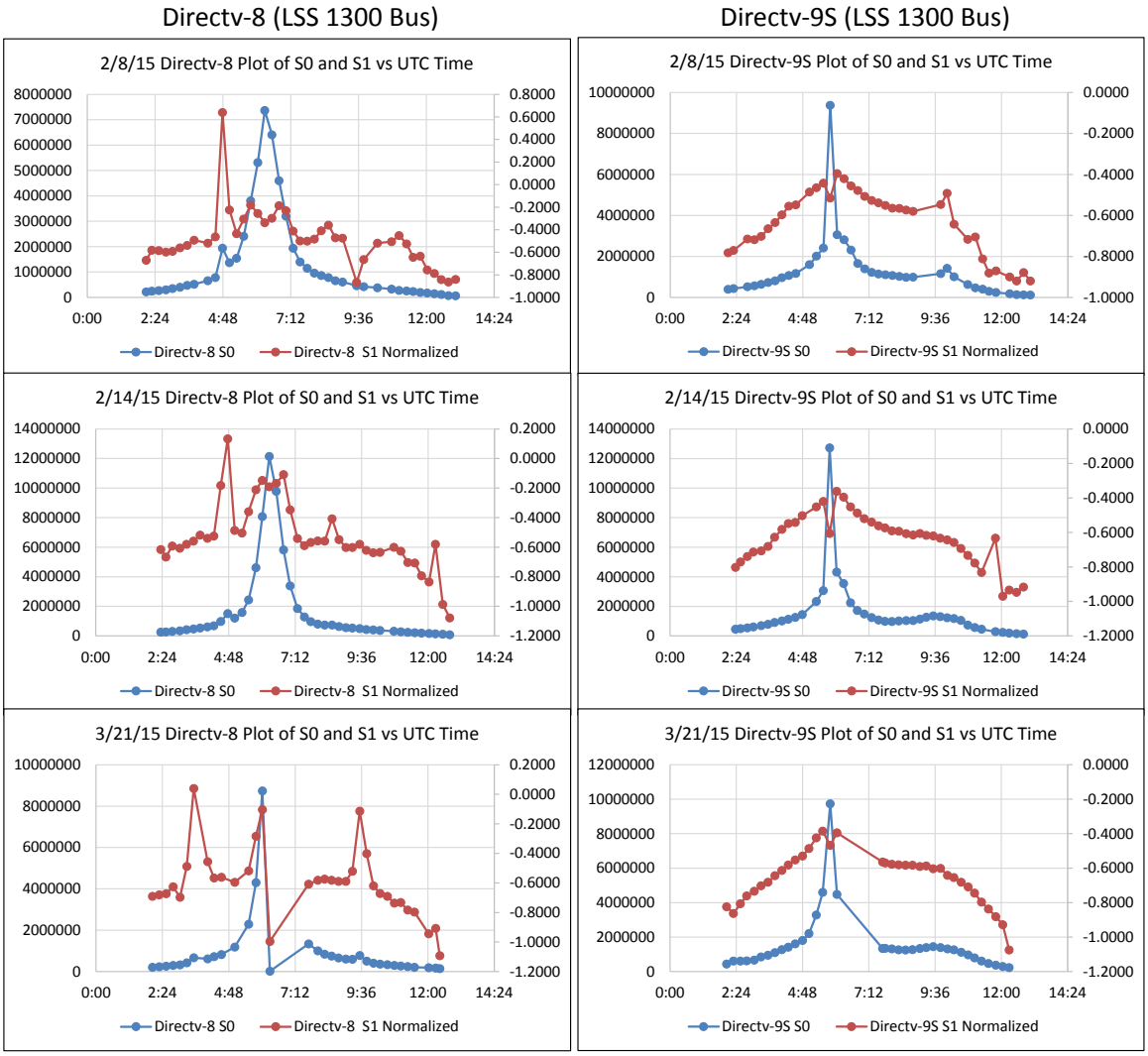

Figure 41. A plot of S_0 and normalized S_1 as a function of UTC time, for Directv-8 and Directv-9S collected February 8th, February 14th, and March 21st, 2015

Figure 42 below shows the intensity and linear polarization values for AMC-15 and AMC-18 as a function of UTC time. Both of these satellites also exhibit a strong increase in linear polarization as the intensity reaches a maximum value. It is also interesting to note that for the AMC-18 data on the third night, while there is a significant

second plateau in the intensity data, the polarization data seems relatively unchanged compared to the other AMC-18 data sets for that same time period around 9:30 UTC implying the intensity and polarization data are not correlated.

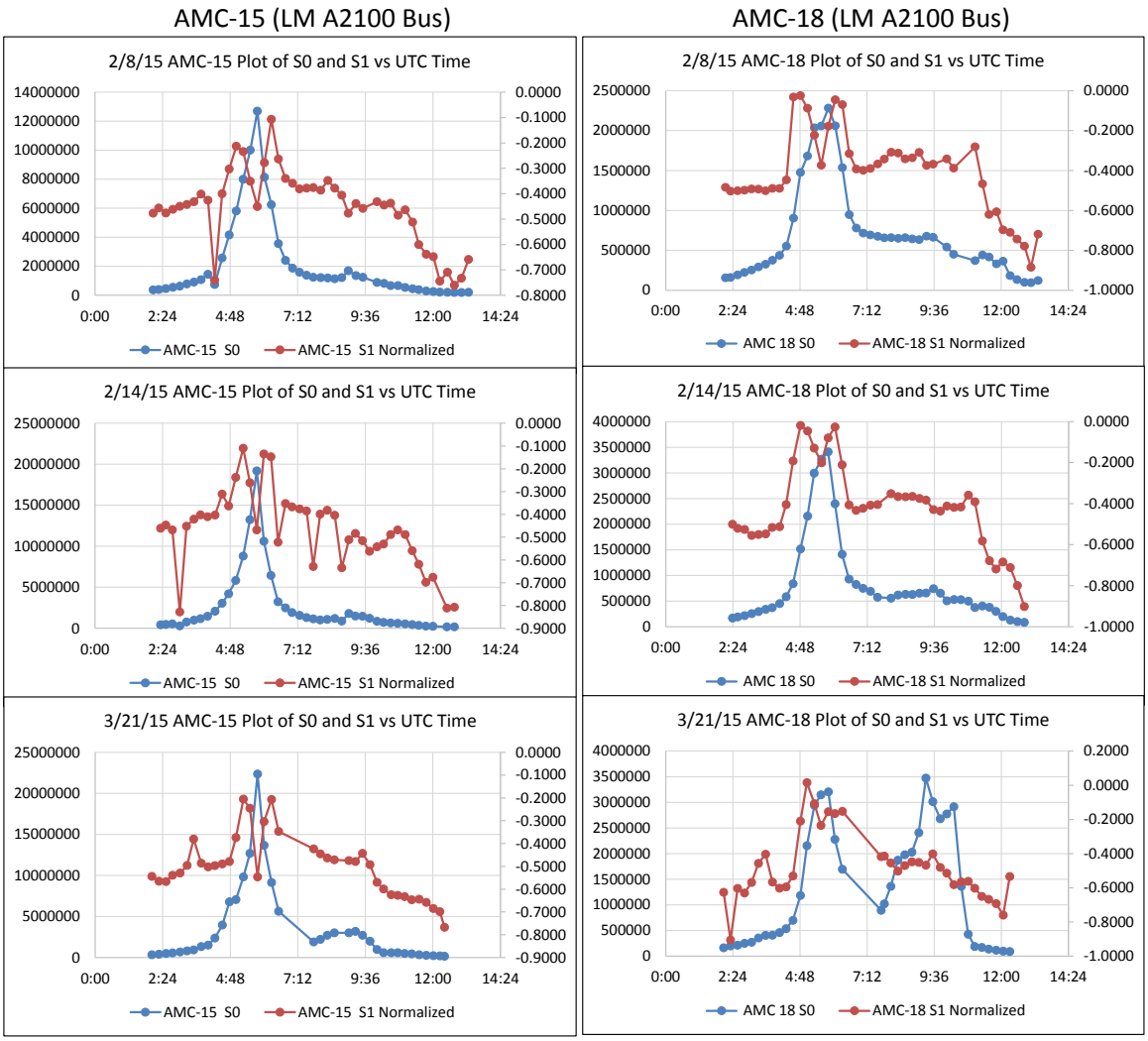

Figure 42. A plot of S_0 and normalized S_1 as a function of UTC time, for AMC-15 and AMC-18 collected February 8th, February 14th, and March 21st, 2015

Figure 43 below shows the intensity and linear polarization values for Directv-10 and Directv-12 as a function of UTC time. Both of these satellites show a relatively high positive correlation of intensity to linear polarization implying a negative correlation due

to the fact that for polarization, a more negative value has a higher degree of polarization since the S_1 values are all below zero on the y-axis of the plot. This data makes it clear that while intensity data alone could not classify these satellites, the significantly different polarization data near the maximum values of intensity can clearly differentiate the two satellites due to the curved apex of Directv-10 compared to the spiked apex for the Directv-12 satellite.

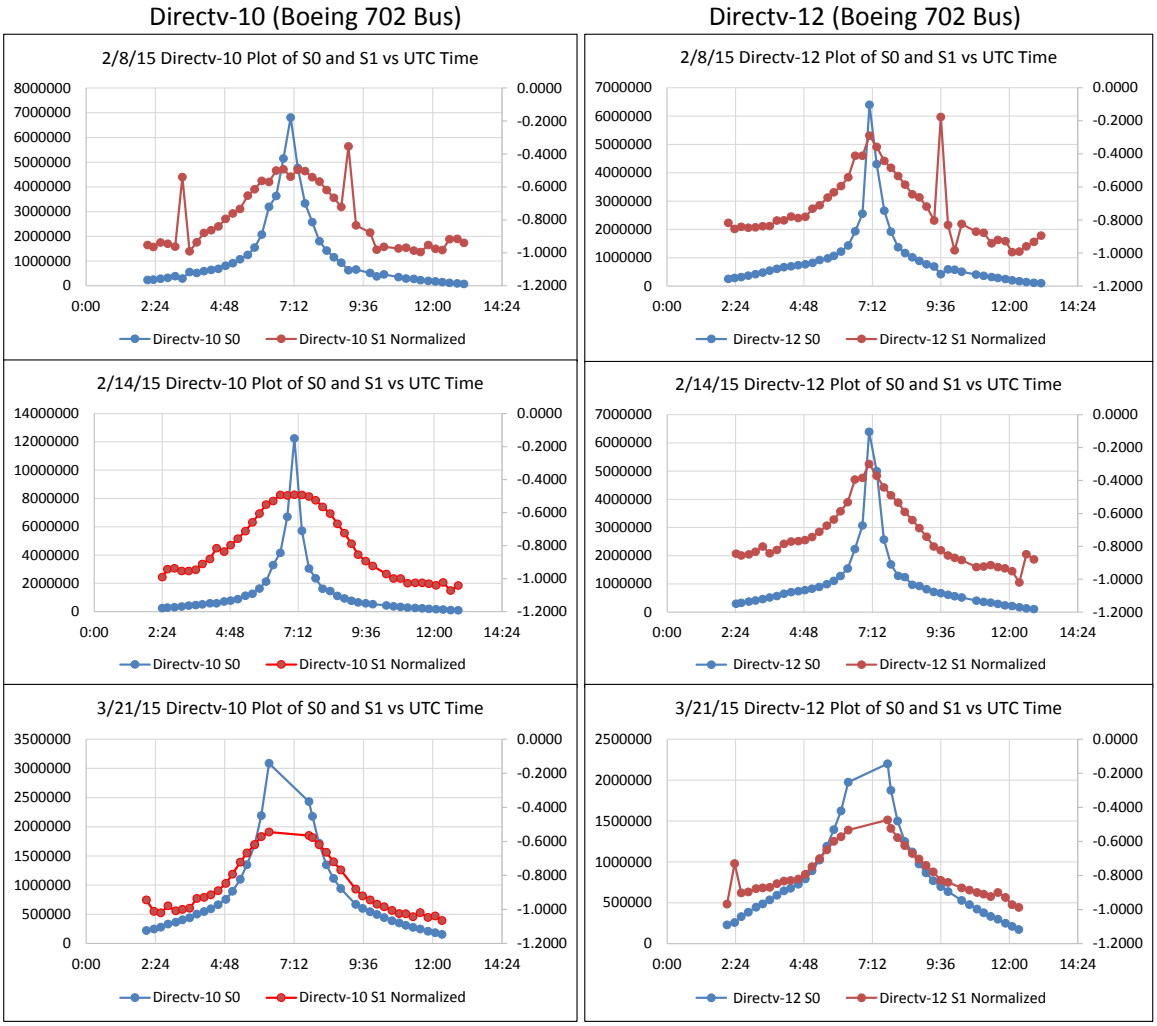

Figure 43. A plot of S_0 and normalized S_1 as a function of UTC time, for Directv-10 and Directv-12 collected February 8th, February 14th, and March 21st, 2015

Figure 44 below shows the intensity and linear polarization values for Directv-4Sand SES-1 as a function of UTC time. Directv-4S has the interesting feature of stronger specular increases in intensity yielding both higher and lower spikes in linear polarization. It should also be noted that the third set of data for SES-1 shows a marked difference in how the polarization data ends at 12:00 compared to the other two sets of data. This difference is not reflected in the corresponding intensity data.

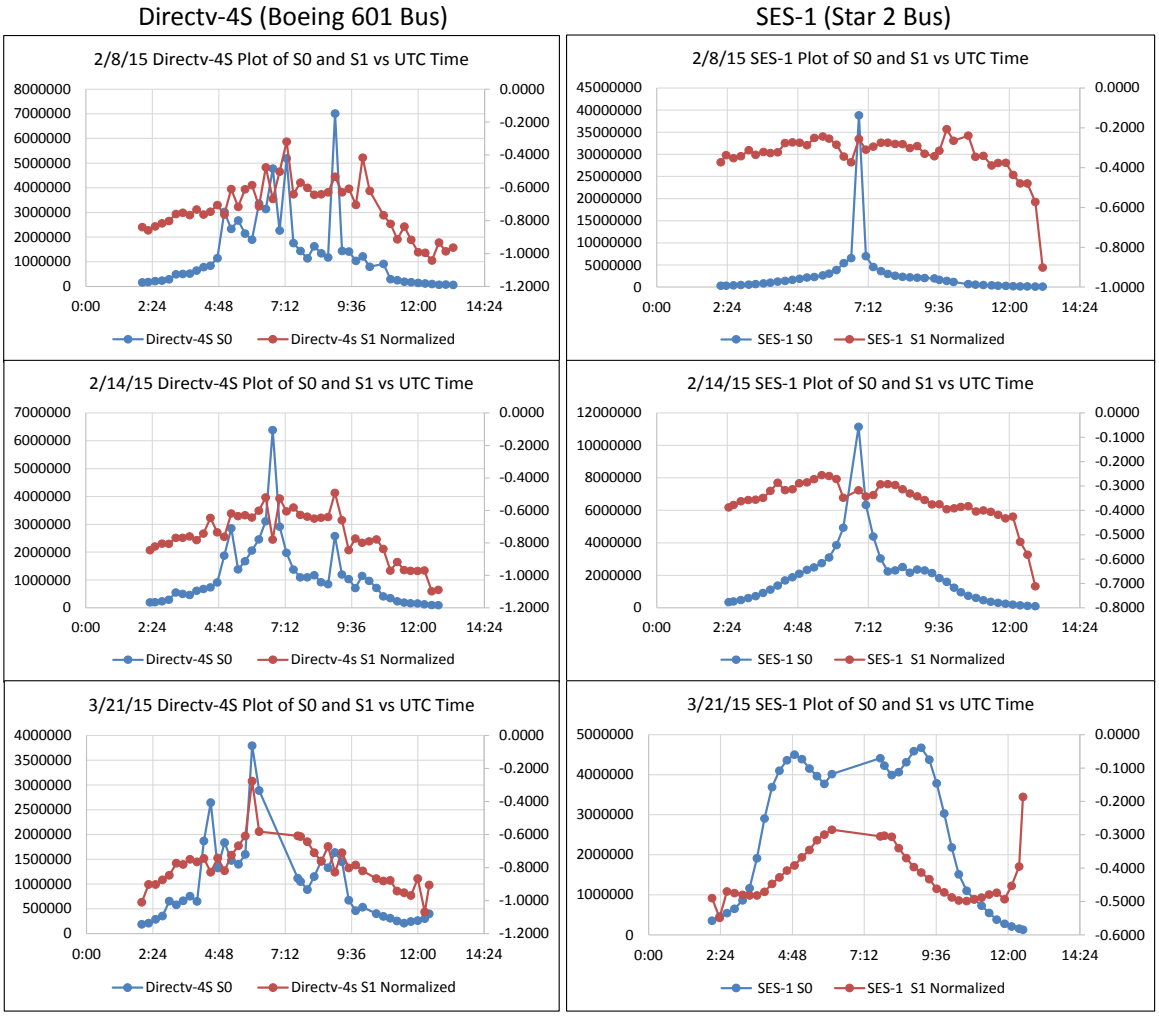

Figure 44. A plot of S_0 and normalized S_1 as a function of UTC time, for Directv-4S and SES-1 collected February 8th, February 14th, and March 21st, 2015

CHAPTER SIX: CONCLUSION

A two channel polarimeter system, calibration method, and preliminary set of collected and processed data were presented that indicate a satellite classifier system using intensity and polarization data may be possible in order to provide relevant data to the Space Situational Awareness community. It was shown that Stokes parameters S_0 and S_1, used in conjunction, may help in identifying specific satellites. No other published research has presented actual observation data regarding using polarization data from unresolved images to develop a satellite classifier. Several key findings have been noted as a result of this research.

The first key finding was that the Stokes parameter for intensity, S_0, did have distinguishing features for the same satellite buses but may provide data to help distinguish between different types of buses. Amplitudes usually varied greatly from night to night for the same satellite but there were some features in the curve shape that could be used as distinguishing characteristics. While trying to establish a distinctive and repeatable feature for when the maximum intensity occurred, it was discovered that there was a relationship with the solar phase angle. This correlation was a linear relationship

between the solar phase angle at which the maximum intensity occurred and the minimum solar phase angle for that night. With this data it should be possible to predict when the maximum intensity will occur for a particular satellite on a given night since the minimum solar phase angle varies through the seasons. This data could help flag a satellite that has been improperly identified by the Space Surveillance Network if the observed intensity does not occur as predicted.

The second key finding was that the Stokes parameter, S_1, for linear polarization was weakly to strongly positively correlated with Stokes parameter, S_0, for total intensity. As explained earlier, this actually indicates a weak to strong negative correlation between intensity and polarization since a more negative value corresponds a stronger vertical or P-polarization when values are below zero on the y-axis. One interesting note is that sometimes an increase in S_0 corresponded to decreases in S_1 and vice versa, while other times, an increase in S_0 corresponded to an increase in S_1. For one particular satellite, Directv-8, there was some component or feature that caused a micro glint that also caused a change in polarization from vertical to horizontal. Fortunately, there are other subtle, repeatable features in the S_1 polarization data that was not seen in the S_0 intensity data. For example, although the Directv-10 and Directv-12 intensity data could not differentiate the satellites, the shape of the polarization data at the maximum intensity was clearly either a smooth curve for Directv-10 or a spike for Directv-12.

The third key finding was that Stokes parameter S_1 showed good repeatability from night to night for each satellite in the general shape of the curve and the actual amplitudes. There were significantly diverse features not only for different satellite buses

but also for the same type of satellite bus launched only a few years apart. It is believed that the differences shown in the linear polarization curves through the night may be attributed to the difference in material optical properties due to aging in the space environment. There is potentially also a difference in the polarization curves due to slightly different materials on the buses, payload configurations (i.e difference in antennas or dishes), or spacecraft CONOPS. This repeatability in the Stokes S_1 data for a given satellite is seen quite clearly both in the plots of normalized linear polarization and in the arithmetic mean of the normalized polarization. Not only are the average values consistent for a particular satellite over time but the values are separated from satellite to satellite. Plots of the standard deviation of normalized S_1 values are not as consistent for a particular satellite and do not enable a distinction between the satellites. While the arithmetic mean values of linear polarization may help in developing a satellite classifier, the standard deviations do not seen to provide a discriminator.

The fourth key finding was that this preliminary study indicates Stokes parameters S_0 (intensity) and S_1 (linear polarization) warrant future research and data collection in order to develop a system that can positively identify and characterize satellites.

The fifth key finding was that repeatability and diversity of the polarization signal implies S_1 is due to optical properties of the materials and differences in the solar phase angle. The Boeing 702 buses used for Directv-10 and Directv-12 showed a strong visual correlation of S_0 with the solar phase angle. These same buses showed an interesting inverse relationship between S_1 and solar phase angle plot shape.

The sixth key finding was that linear polarization generally started out higher at the beginning of the evening, dropped to lower values as the solar phase angles decreased, and raised back up to higher values as the solar phase angles increased. This is due to the fact that the angle of incident light to the bus surfaces that are in view of the observer generally starts out large, decreases to zero or normal to the surface, and then increases to a large value by the end of the night. The Degree of Polarization (DOP) is generally lower as the angle of incident light to the reflection surface approaches zero degrees (Schott 2009). See Figure 23 for the viewing geometry as it changes through the night.

It should be noted that since the two channel polarimeter is not aligned with the solar orbit plane, polarization results will change based on the changing solar phase angle although for geostationary satellites this change will be minimal since the viewing geometry does not change appreciably. This change through the year can be characterized in future studies.

REFERENCES

Teehan, R., "Responsive Space Situational Awareness in 2020", Blue Horizons Paper from the Center for Strategy and Technology at the Air War College, April 2007.

Blake, T., "Space Domain Awareness", 2011 AMOS Conference Technical Briefing, The Maui Economic Development Board, Inc., Kihei, Maui, HI, 2011.

Wertz and Larson (editors), "Space Mission Analysis and Design", Microcosm Press, 2010.

Drummond, J. and Rast, R., "First Resolved Images of a Spacecraft in Geostationary Orbit with the Keck-II 10 m Telescope", Proceedings from AMOS Conference 2010.

Bruski, S., Harms, S., Jones, M., Thomas, N., Dahlke, S., "Determination of Satellite Characteristics Through Visible Light Intensity Analysis", Proceedings from AMOS Conference 2012.

Cauquy, M., Roggemann, M., and Schulz, T., "Distance-based and Neural-net-based Approaches for Classifying Satellites Using Spectral measurements", Optical Engineering SPIE Vol. 45, 2006.

Bowers, D., Wellems, D., Duggin, M., Glass, W., and Vaughn, L., "Broadband Spectral-Polarimetric BRDF Scan System and Data for Spacecraft Materials", Air Force Research Laboratory, Kirtland AFB, 2011.

Bush, K., Crockett, G., and Barnard, C., "Satellite Discrimination From Active and Passive Polarization Signatures: Simulation Predictions Using the TASAT Satellite Model", Proceedings of SPIE Polarization Analysis, Measurement, and Remote Sensing IV, SPIE Vol. 4481, 2002.

Pesses, M., Ryan, E., "A New Spin On Spin Polarimetry", Proceedings from AMOS Conference 2007.

Tippets, R., “Polarimetric Imaging of Artificial Satellites”, dissertation, The Union Institute and University, 2005.

Stryjewski, J., Hand, D., Tyler, D., Murali, S., Roggemann, M., Peterson, N., “Real Time Polarization Light Curves for Space Debris and Satellites”, Proceedings from AMOS Conference 2010.

“Image of Electromagnetic Radiation”, accessed June 3, 2015, https://s.yimg.com/fz/api/res/1.2/KZ5p4VlbCTHEac4_Mh1vvw--/YXBwaWQ9c3JjaGRkO2g9MTg3O3E9OTU7dz0yNjM-/http://micro.magnet.fsu.edu/primer/java/electromagnetic/electromagneticjavafigure1.jpg

Hudson, A. and Nelson, R., “University Physics”, Harcourt Brace Jovanovich Inc, 1982.

“The Picket Fence Analogy”, accessed May 9, 2015, http://www.physicsclassroom.com/class/light/u12l1e3.gif.

Tinbergen, J., “Astronomical Polarimetry”, Cambridge University Press, 1996.

Schott, J., “Fundamentals of Polarimetric Remote Sensing”, SPIE Press, 2009.

Kliger, D., Lewis, J., Randall, C., Polarized Light in Optics and Spectroscopy, Academic Press, p. 103-107, 1990.

“Circular.Polarization.Circularly.Polarized.Light_With.Components_Right.Handed.”, accessed May 9, 2015, http://upload.wikimedia.org/wikipedia/commons/thumb/7/77/Circular.Polarization.Circularly.Polarized.Light_With.Components_Right.Handed.svg/440px-Circular.Polarization.Circularly.Polarized.Light_With.Components_Right.Handed.svg.png.

“Image of Elliptically Polarized Light”, accessed May 9, 2015, https://sp.yimg.com/ib/th?id=JN.7Eytji1%2fJuFxfR2fEPLiGA&pid=15.1&P=0.

“Image of Polarizing Beamsplitter”, accessed May 9, 2015, http://www.edmundoptics.com/images/articles/fig-3-tb.gif.

Tribble, Alan C., The Space Environment, Princeton University Press, 1995.

Wilkes, D. R. and Zwiener, J. M., “Science Data Report for the Optical Properties Monitor (OPM) Experiment”, NASA/CR-2001-210881, Marshal Space Flight Center, March 2001.

Rantanen, R., Gordon, T., Finckernor, M., and Pippin, G., "Comparison of Contamination Model Predictions to LDEF Surface Measurements", Conference on Optical Contamination: Effects, Measurements, and Control VI, SPIE Vol. 3427, 1998.

Pippin, G. and Finckenor, M., "Measurements of Optically Transparent and Mirrored specimens From The POSA, LDEF A0034, and EOIM-III Space Flight Experiments", Optical System Contamination: Effects, Measurements, and Control VII, SPIE Vol. 4774, 2002.

Dearborn, M., Chun, F., Liu, J., and Tippets, R., "USAF Academy Center for Space Situational Awareness", 2011 AMOS Technical Conference Paper, The Maui Economic Development Board, Inc., Kihei, Maui, HI, 2011.

Apogee F47 camera datasheet from Apogee Imaging Systems, accessed May 9, 2015, http://www.ccd.com/alta_f47.html.

Edmund Optics, Polarizing Cube Beamsplitter 50 mm VIS data sheet, accessed May 9, 2015, http://www.edmundoptics.com/optics/beamsplitters/cube-beamsplitters/broadband-polarizing-cube-beamsplitters/2986/.

AlnitaK Astrosystems, Flat Man XL data sheet, accessed May 9, 2015, http://optecinc.com/astronomy/catalog/alnitak/flatmanxl.htm.

Chenault, D., "Infrared Spectropolarimetry", dissertation, The University of Alabama, 1992.

Speicher, A., Matin, M., Tippets, R., and Chun, F., "Calibration of a system to collect visible-light polarization data for classification of geosynchronous satellites", Remote Sensing System Engineering V, SPIE Vol. 9223, 2014.

Hornbeck, R., "Numerical Methods", Quantum Publishers, 1975.

"Image of Directv-4S", accessed May 9, 2015, http://space.skyrocket.de/img_sat/directv-4s__1.jpg.

"Image of Directv-8", accessed May 9, 2015, http://space.skyrocket.de/img_sat/directv-8__1.jpg.

"Image of Directv-9S", accessed May 9, 2015, http://sslmda.com/images/products/renderings/directv9s.jpg.

"Image of SES-1", accessed May 9, 2015, https://sp.yimg.com/ib/th?id=JN.2CzXiaeVI8ME5%2bvUS13OWQ&pid=15.1&P=0.

"Image of MAC-15", accessed May 9, 2015, http://space.skyrocket.de/img_sat/amc-15__1.jpg.

"Image of AMC-18", accessed May 9, 2015, http://images.spaceref.com/news/a2100.jpg.

"Image of Directv-10 and Directv-12", accessed May 9, 2015, http://space.skyrocket.de/img_sat/directv-10__2.jpg.

Cognion, R., "Observations and modeling of GEO satellites at large phase angles", AMOS Proceedings, 2013.

Speicher, A., Matin, M., Tippets, R., Chun, F., Strong, D., "Results from an experiment that collected visible-light polarization data using unresolved imagery for classification of geosynchronous satellites", Airborne Intelligence, Surveillance, Reconnaissance (ISR) Systems and Applications XII, SPIE Vol. 9460, 2015.

http://cynogen.com, Diffraction Limited Maxim DL.

McClave, J. and Dietrich II, F., "Statistics", Dellen Publishing Company, 1985.

APPENDIX A: SIGNAL-TO-NOISE CALCULATION

Calculate Expected Signal and Noise

Calculate Watts/m^2 at telescope entrance

SatVisualMag := 12

SunVisualMag := −26.75

SunIntensity := 1367 $\frac{watts}{m^2}$

VisualMagDiff := SatVisualMag − SunVisualMag VisualMagDiff = 38.75

Temp := $\frac{VisualMagDiff}{-2.5}$ Temp = −15.5

Temp := Temp + log(SunIntensity) Temp = −12.364

GeoIntensity := 10^{Temp} GeoIntensity = 4.323×10^{-13} $\frac{watts}{m^2}$

Calculate the energy of each photon at the given wavelength

λ := $0.4 \cdot 10^{-6}$ wavelength in meters

Planck := $6.6260755 \cdot 10^{-34}$ watts·sec^2

c := $3 \cdot 10^{8}$ $\frac{meters}{sec}$

EnergyPhoton := $\frac{(Planck \cdot c)}{\lambda}$ EnergyPhoton = 0 watt sec

Calculate the effective telescope aperture

MirrorDia_inch := 20

MirrorDia_meters := 0.0254·MirrorDia_inch MirrorDia_meters = 0.508 meters

Collect_area := $\pi \cdot \left(\frac{MirrorDia\_meters}{2}\right)^2$ Collect_area = 0.203 meters^2

Mirror_obstruction_radius := 0.1 meters

Obstructed_area := $\pi \cdot$Mirror_obstruction_radius^2 Obstructed_area = 0.031 m^2

Effective_collect_area := Collect_area − Obstructed_area Effective_collect_area = 0.171 m^2

Calculate the number of photons per square meter at telescope entrance

$$Photons := \frac{GeoIntensity}{EnergyPhoton}$$ Photons = 8.699×10^5 per sec per m^2

Calculate the number of photons that enter the telescope per second

Photons_in_sec := Photons$\cdot$Effective_collect_area Photons_in_sec = 1.49×10^5

Calculate the number of photons that get through the beamsplitter and strike the FPA per sec

Polarization_split := 0.3

Photons_at_FPA := Photons_in_sec$\cdot$Polarization_split Photons_at_FPA = 4.469×10^4

Calculate the number of photons per pixel per second

Pixels_for_sat := 210

$$Photons\_per\_pixel := \frac{Photons\_at\_FPA}{Pixels\_for\_sat}$$ Photons_per_pixel = 212.827

Calculate the number of electrons per pixel per second

QE := 0.75

electrons_pixel_sec := Photons_per_pixel$\cdot$QE electrons_pixel_sec = 159.62

Calculate the number of electrons for the integration period

Integration := 10 seconds

S_t := electrons_pixel_sec·Integration S_t = 1.596×10^3 signal in electrons

N_pixels := 210 N_pixels = 210 total satellite pixels

S_t_total := S_t·N_pixels S_t_total = 3.352×10^5 electrons for 210 pixels

Compare to actual data taken of Directv-4S

actual_counts := 322423 counts for 210 pixels

$$\text{Difference} := \left(\frac{\text{actual\_counts} - \text{S\_t\_total}}{\text{actual\_counts}}\right) \cdot 100$$

Difference = −3.964 percent

Calculate the percentage of full well

Full_well := 100000 electrons

$$\text{Percent\_Full\_Well} := \left(\frac{\text{S\_t}}{\text{Full\_well}}\right) \cdot 100$$

Percent_Full_Well = 1.596

Calculate the noise of the FPA (values from the F47 data sheet

Nr := 2 Readout noise in electrons rms

Ns := 15 System noise in electrons rms

Ndc := 0.2 Dark current noise inelectrons per pixel per second

Ndc_t := Ndc·Integration Ndc_t = 2 electrons

Nb := 20 Background noise estimate in electrons per pixel per second

$Nb\_t := Nb \cdot Integration$ $Nb\_t = 200$ electrons per pixel

$$N\_total := \left| S\_t\_total + N\_pixels \cdot \left(Nb\_t + Ndc\_t + Nr^2 \right) \right|^{0.5}$$

$N\_total = 615.193$ electrons per 210 pixels

Calculate the Signal to noise ratio

$$SN := \frac{S\_t \cdot N\_pixels}{N\_total}$$

$SN = 544.874$

Calculate the Signal to Noise ratio assuming polarization

$Polarization := 0.2$

$SN\_polarization := SN \cdot Polarization$

$SN\_polarization = 108.975$

APPENDIX B: MUELLER MATRIX ALGORITHM

Polarization Data Reduction Approach

Initialize variables

$n := 18$

$i := 0..n$

$angles := 19$

$chan := 4$

Input data from intensity measurements (normalized)

Cam0 Ppol

$$dd := \begin{pmatrix} 0.5207 \\ 0.5298 \\ 0.5565 \\ 0.5950 \\ 0.6459 \\ 0.7032 \\ 0.7514 \\ 0.8015 \\ 0.8315 \\ 0.8406 \\ 0.8309 \\ 0.8012 \\ 0.7577 \\ 0.7040 \\ 0.6468 \\ 0.5982 \\ 0.5569 \\ 0.5311 \\ 0.5207 \end{pmatrix}$$

$$bb := \begin{pmatrix} 0 \\ 0 \\ 0 \\ 0 \\ 0 \\ 0 \\ 0 \\ 0 \\ 0 \\ 0 \\ 0 \\ 0 \\ 0 \\ 0 \\ 0 \\ 0 \\ 0 \\ 0 \\ 0 \end{pmatrix}$$

$$cc := \begin{pmatrix} 0 \\ 0 \\ 0 \\ 0 \\ 0 \\ 0 \\ 0 \\ 0 \\ 0 \\ 0 \\ 0 \\ 0 \\ 0 \\ 0 \\ 0 \\ 0 \\ 0 \\ 0 \\ 0 \end{pmatrix}$$

Cam90 Spol

$$aa := \begin{pmatrix} 0.4792 \\ 0.4701 \\ 0.4435 \\ 0.4050 \\ 0.3541 \\ 0.2968 \\ 0.2486 \\ 0.1985 \\ 0.1685 \\ 0.1594 \\ 0.1691 \\ 0.1988 \\ 0.2423 \\ 0.2960 \\ 0.3532 \\ 0.4018 \\ 0.4431 \\ 0.4689 \\ 0.4792 \end{pmatrix}$$

Calculate estimates using a model for input into the solver

$$
\begin{array}{l}
estimates(a, chan, angles) := \\
\quad i \leftarrow 0 \\
\quad j \leftarrow 0 \\
\quad k \leftarrow 0 \\
\quad \textbf{while } j < chan \\
\quad\quad k \leftarrow 0 \\
\quad\quad sa \leftarrow a_{j,3} \cdot a_{j,3+1} \\
\quad\quad sb \leftarrow a_{j,3} \cdot a_{j,3+2} \\
\quad\quad \textbf{while } k < angles \\
\quad\quad\quad \phi \leftarrow k \cdot 10 \cdot \frac{\pi}{180} \\
\quad\quad\quad s0 \leftarrow 1 \\
\quad\quad\quad s0 \leftarrow a_{11+k} \quad \textbf{if } k \neq 0 \\
\quad\quad\quad s1 \leftarrow s0 \cdot cos(2 \cdot \phi) \\
\quad\quad\quad s2 \leftarrow s0 \cdot sin(2 \cdot \phi) \\
\quad\quad\quad intensity_i \leftarrow \frac{1}{2} \cdot \left(s0 \cdot a_{j,3} + s1 \cdot sa + s2 \cdot sb\right) \\
\quad\quad\quad k \leftarrow k + 1 \\
\quad\quad\quad i \leftarrow i + 1 \\
\quad\quad j \leftarrow j + 1 \\
\quad intensity
\end{array}
$$

$$
\begin{aligned}
&initialize(a, b, c) := \\
&\quad i \leftarrow 0 \\
&\quad j \leftarrow 0 \\
&\quad k \leftarrow 0 \\
&\quad \textbf{while } j < b \\
&\quad\quad k \leftarrow 0 \\
&\quad\quad sa \leftarrow a_{j,\,3+1} \\
&\quad\quad sb \leftarrow a_{j,\,3+2} \\
&\quad\quad \textbf{while } k < c \\
&\quad\quad\quad \phi \leftarrow k \cdot 10 \cdot \frac{\pi}{180} \\
&\quad\quad\quad s1 \leftarrow \cos(2\phi) \\
&\quad\quad\quad s2 \leftarrow \sin(2 \cdot \phi) \\
&\quad\quad\quad intensity_i \leftarrow \frac{1}{2} \cdot \left(a_{j,\,3} + s1 \cdot sa + s2 \cdot sb\right) \\
&\quad\quad\quad k \leftarrow k + 1 \\
&\quad\quad\quad i \leftarrow i + 1 \\
&\quad\quad j \leftarrow j + 1 \\
&\quad intensity
\end{aligned}
$$

$$
\begin{aligned}
&partials(\Omega, t, P, chan, angles, n) := \\
&\quad i \leftarrow 0 \\
&\quad \varepsilon \leftarrow .001 \\
&\quad \nu \leftarrow P \\
&\quad \text{while } i \leq t \\
&\quad\quad \upsilon_i \leftarrow P_i \\
&\quad\quad increment \leftarrow \varepsilon \cdot |P_i| \\
&\quad\quad increment \leftarrow \varepsilon \quad \text{if } increment = 0 \\
&\quad\quad \nu_i \leftarrow P_i + increment \\
&\quad\quad \beta \leftarrow estimates(\nu, chan, angles) \quad \text{if } \Omega = 0 \\
&\quad\quad \beta \leftarrow initialize(\nu, chan, angles) \quad \text{otherwise} \\
&\quad\quad \xi \leftarrow estimates(P, chan, angles) \quad \text{if } \Omega = 0 \\
&\quad\quad \xi \leftarrow initialize(P, chan, angles) \quad \text{otherwise} \\
&\quad\quad j \leftarrow 0 \\
&\quad\quad \text{while } j \leq n \\
&\quad\quad\quad \mu_{j,i} \leftarrow \frac{(\beta_j - \xi_j)}{increment} \\
&\quad\quad\quad j \leftarrow j + 1 \\
&\quad\quad i \leftarrow i + 1 \\
&\quad \mu
\end{aligned}
$$

$$
\begin{aligned}
&chisqr(y, intensity, n) := \\
&\quad val \leftarrow \sum_{l=0}^{n} \left(y_l - intensity_l\right)^2 \\
&\quad val
\end{aligned}
$$

$$\chi(\Omega, t, \beta, \lambda, d, P, chan, angles) :=$$

$i \leftarrow 0$

$j \leftarrow 0$

$energy \leftarrow estimates(P, chan, angles) \quad if \ \Omega = 0$

$energy \leftarrow initialize(P, chan, angles) \quad otherwise$

$\gamma \leftarrow \beta^T \cdot \beta$

while $j \leq t$

- $i \leftarrow 0$
- *while* $i \leq t$
  - $\zeta_{i,j} \leftarrow \dfrac{\gamma_{i,j}}{\sqrt{\gamma_{j,j} \cdot \gamma_{i,i}}}$
  - $i \leftarrow i + 1$
- $\zeta_{j,j} \leftarrow 1 + \lambda$
- $j \leftarrow j + 1$

$\zeta \leftarrow \zeta^{-1}$

$y \leftarrow d - energy$

$j \leftarrow 0$

while $j \leq t$

- $i \leftarrow 0$
- *while* $i \leq t$
  - $\zeta_{i,j} \leftarrow \dfrac{\zeta_{i,j}}{\sqrt{\gamma_{j,j} \cdot \gamma_{i,i}}}$
  - $i \leftarrow i + 1$
- $j \leftarrow j + 1$

$\varepsilon \leftarrow \zeta \cdot \beta^T \cdot y$

$\nu \leftarrow P + \varepsilon$

ν

```
marquardt(Ω, t, n, y, P, chan, angles) :=
    λ ← .00001
    k ← 0
    tolerance ← .0000001
    while k < 1000
        α ← partials(Ω, t, P, chan, angles, n)
        intensity ← estimates(P, chan, angles)  if Ω = 0
        intensity ← initialize(P, chan, angles)  otherwise
        chi ← chisqr(y, intensity, n)
        j ← 0
        while j < 1000
            ν ← χ(Ω, t, α, λ, y, P, chan, angles)
            intensity ← estimates(ν, chan, angles)  if Ω = 0
            intensity ← initialize(ν, chan, angles)  otherwise
            chi2 ← chisqr(y, intensity, n)
            dif ← chi − chi2
            break  if  dif ≥ 0
            λ ← λ·10
            j ← j + 1
        λ ← λ / 100
        break  if  |dif| / chi2 ≤ tolerance
        P ← ν
        k ← k + 1
    ν
```

```
makey(aa, bb, cc, dd, n) :=
    i ← 0
    while i < n
        y_i ← aa_i
        y_(i+19) ← bb_i
        y_(i+38) ← cc_i
        y_(i+57) ← dd_i
        i ← i + 1
    y
```

```
params(angles) := | k ← 0
                  | while k < angles
                  |     | c_{k+12} ← 1
                  |     | k ← k + 1
                  | c
```

$y := makey(aa, bb, cc, dd, 19)$ $\quad rows(y) = 76$

```
organize_data(aa, bb, cc, dd, n) := | i ← 0
                                    | while i < n + 1
                                    |     | d_{0,i} ← aa_i
                                    |     | d_{1,i} ← dd_i
                                    |     | i ← i + 1
                                    | d
```

```
Generate_Stokes(Data, W) := | i ← 0
                            | while i < n + 1
                            |     | D^⟨i⟩ ← W · Data^⟨i⟩
                            |     | i ← i + 1
                            | D
```

Initialization and setup

$$analyzerangles := \begin{pmatrix} 0 \\ 135 \\ 45 \\ 90 \end{pmatrix}$$

$\Omega := 1$

$init_0 := -0.5$ $init_3 := .4$ $init_6 := .4$ $init_9 := .4$

$init_1 := .4$ $init_4 := .4$ $init_7 := .5$ $init_{10} := -.3$

$init_2 := -0.2$ $init_5 := -.5$ $init_8 := .8$ $init_{11} := .78$

$i := 0..76$ $n := 75$

$t := last(init)$ $t = 11$

$start := initialize(init, chan, angles)$

$fit := marquardt(\Omega, t, n, y, init, chan, angles)$

$finish := initialize(fit, chan, angles)$

$analyzerangles_0 := 28.648 \cdot atan2(fit_1, fit_2)$

$analyzerangles_1 := 28.648 \cdot atan2(fit_4, fit_5)$

$analyzerangles_2 := 28.648 \cdot atan2(fit_7, fit_8)$

$analyzerangles_3 := 28.648 \cdot atan2(fit_{10}, fit_{11})$

$analyzerangles_0 = 0.7121396693$ $analyzerangles_1 = -43.5682562246$

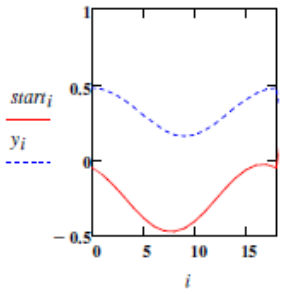

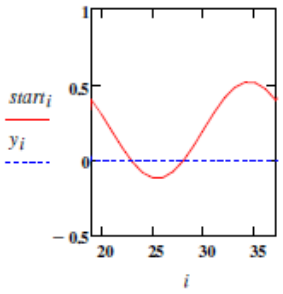

$analyzerangles_2 = -88.1119858335$ $analyzerangles_3 = -88.5714953241$

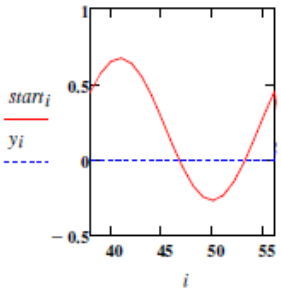

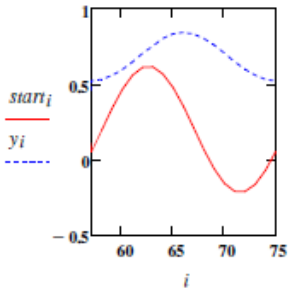

$$Eff(A, n) := \left| \begin{array}{l} i \leftarrow 0 \\ \text{while } i < n + 1 \\ \quad \left| \begin{array}{l} d \leftarrow A^{\langle i \rangle} \\ s_{0,i} \leftarrow \left| \dfrac{d_0 - d_2}{d_0 + d_2} \right| \\ s_{1,i} \leftarrow \left| \dfrac{d_1 - d_3}{d_1 + d_3} \right| \\ i \leftarrow i + 1 \end{array} \right. \\ s \end{array} \right.$$

$$initial2(fit, b, param) := \left| \begin{array}{l} j \leftarrow 0 \\ \text{while } j < b \\ \quad \left| \begin{array}{l} param_{j \cdot 3} \leftarrow fit_{j \cdot 3} \\ param_{j \cdot 3+1} \leftarrow fit_{j \cdot 3} \cdot fit_{j \cdot 3+1} \\ param_{j \cdot 3+2} \leftarrow fit_{j \cdot 3} \cdot fit_{j \cdot 3+2} \\ j \leftarrow j + 1 \end{array} \right. \\ param \end{array} \right.$$

$parameters := params(angles)$

$parameters := initial2(fit, chan, parameters)$

$n := 75 \qquad i := 0 .. n$

$intensities := estimates(parameters, chan, angles)$

$analyzerangles_0 = 0.7121396693 \qquad analyzerangles_1 = -43.5682562246$

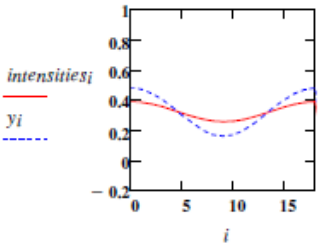

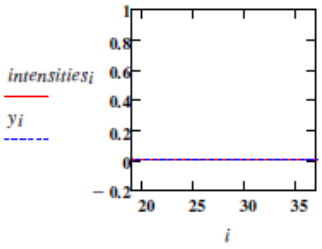

$analyzerangles_2 = -88.1119858335 \qquad analyzerangles_3 = -88.5714953241$

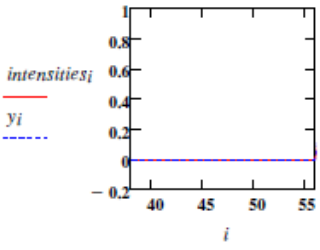

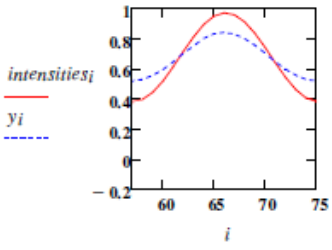

$n := 75 \qquad \Omega := 0$

$P := parameters$

$t := last(P) \qquad t = 30$

$fit := marquardt(\Omega, t, n, y, P, chan, angles)$

$intensities := estimates(fit, chan, angles)$

$$DOP(p) := \left| \begin{array}{l} j \leftarrow 0 \\ \text{while } j < 4 \\ \quad \left| \begin{array}{l} f_{j,1} \leftarrow \sqrt{(p_{j\cdot 3+1})^2 + (p_{j\cdot 3+2})^2} \\ f_{j,2} \leftarrow 28.648 \cdot atan2(p_{j\cdot 3+1}, p_{j\cdot 3+2}) \\ f_{j,0} \leftarrow p_{j\cdot 3} \\ f_{j,3} \leftarrow \dfrac{1}{1 - f_{j,1}} \\ j \leftarrow j + 1 \end{array} \right. \\ f \end{array} \right.$$

$$dolp := DOP(fit)$$

$$analyzer\_angle\_one := 28.648 \cdot atan2(fit_1, fit_2) \qquad analyzer\_angle\_two := 28.648 \cdot atan2(fit_4, fit_5)$$

$$analyzer\_angle\_3 := 28.648 \cdot atan2(fit_7, fit_8) \qquad analyzer\_angle\_4 := 28.648 \cdot atan2(fit_{10}, fit_{11})$$

$$dolp = \begin{pmatrix} 0.6598750049 & 0.4622061428 & 0.6547528517 & 1.8594485351 \\ 3.2409169836 \times 10^{-3} & 8.1075595872 \times 10^{-6} & -39.1432364641 & 1.0000081076 \\ -7.0310405997 \times 10^{-4} & 1.3679552407 \times 10^{-6} & 1.8883605065 & 1.000001368 \\ 1.4082573569 & 0.2693402772 & -88.606005994 & 1.3686261453 \end{pmatrix}$$

$analyzer\_angle\_one = 0.6547528517$

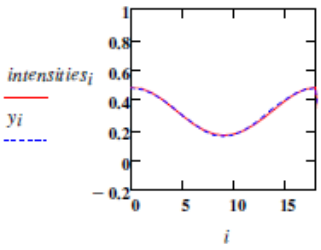

$analyzer\_angle\_two = -39.1432364641$

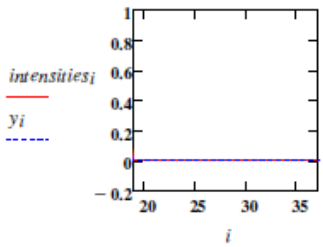

$analyzer\_angle\_3 = 1.8883605065$

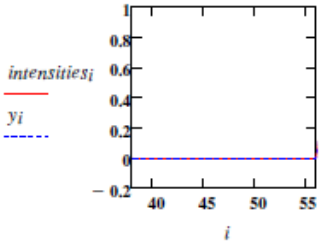

$analyzer\_angle\_4 = -88.606005994$

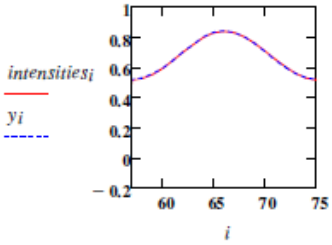

$intensities := estimates(fit, chan, angles)$

$residuals := y - intensities$

$rss := stdev(residuals)$

$rss = 3.6704741589 \times 10^{-3}$

$analyzer\_angle\_one = 0.6547528517$

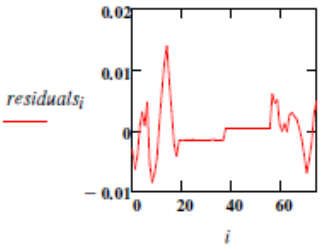

$analyzer\_angle\_two = -39.1432364641$

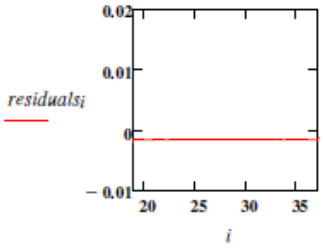

$analyzer\_angle\_3 = 1.8883605065$

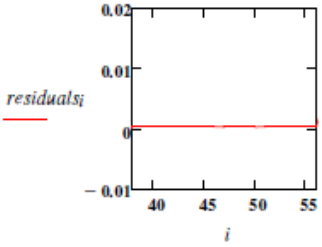

$analyzer\_angle\_4 = -88.606005994$

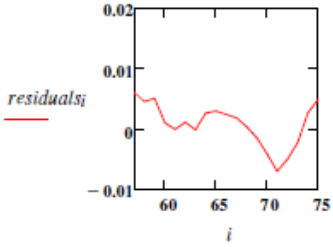

$m := 12 .. 29$

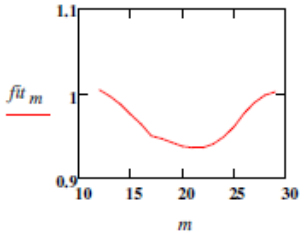

$$Aver := \left(\frac{1}{18}\right) \cdot \sum_{m=12}^{29} fit_m$$

$Aver = 0.9666184561$

$$U := \frac{1}{2} \cdot \begin{pmatrix} fit_0 & fit_1 \cdot fit_0 \\ fit_9 & fit_9 \cdot fit_{10} \end{pmatrix}$$

$$U = \begin{pmatrix} 0.3299375024 & 0.1524593127 \\ 0.7041286784 & -0.1894256254 \end{pmatrix}$$

$W := \left(U^T \cdot U\right)^{-1} \cdot U^T$

$$W = \begin{pmatrix} 1.1152551091 & 0.8976136523 \\ 4.1456012327 & -1.9425274935 \end{pmatrix}$$

$Data := organize\_data(aa, bb, cc, dd, 18)$

$Stokes := Generate\_Stokes(Data, W)$

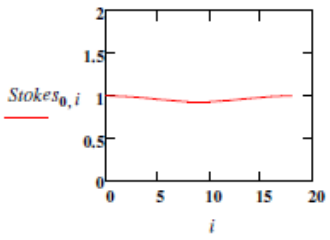

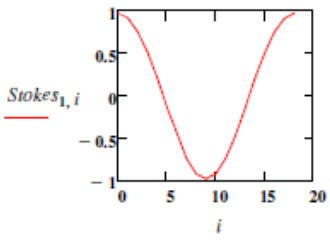

$$U = \begin{pmatrix} 0.3299375024 & 0.1524593127 \\ 0.7041286784 & -0.1894256254 \end{pmatrix}$$

$$W := U^{-1}$$

$$W = \begin{pmatrix} 1.1152551091 & 0.8976136523 \\ 4.1456012327 & -1.9425274935 \end{pmatrix}$$